PROTECT2024

9th International Colloquium on Performance, Protection & Strengthening of Structures Under Extreme Loading & Events

13 - 16 August 2024 I Singapore

CONFERENCE PROCEEDINGS

Organised by

NANYANG TECHNOLOGICAL UNIVERSITY SINGAPORE

NTU CEE Alumni Association

LIST OF TECHNICAL PAPERS

ID Number	Authors (s) – Paper Title
SSEL-1	***Ahmed Almaadawy, Srishti Banerji, Ghada M. Hekal, Magdy I. Salama -*** Response Of Continuous RC Beams Strengthened Using Strain-hardening Cementitious Composities
SSEL-3	***Javad Shayanfar, Joaquim A. O. Barros*** – FRP Confinement-induced Enhancement In Stress-strain Behavior Of Fire-damaged Concrete Columns: Design-oriented Model
SSEL-6	***Roouf Un Nabi Dar, Dr. P. Alagappan*** - Numerical Study On The Perforation Of Coated RC Panels By Hard Projectiles
SSEL-7	***Topendra Oli, Abidemi Bashiru Folorunsho, Gihyun Kim, Taejin Jang, Cheolwoo Park, Seungwon Kim -*** Explosion Analysis On Protection Wall Of Hydrogen Storage Tank With TNT Equivalent Weight Method
SSEL-8	***Wenbing Han, Kang Chen, Daming Wang, Bo Yang*** - Resistance Of Composite Beam With Various Types Of Connections Under Midspan Impact Scenarios
SSEL-12	***Eyal Eytam, Hezi Y. Grisaro*** - Mitigating Damage Of Structures Under Blast Loads Using Linear Protective Layers
SSEL-13	***Scott McFadden, Wesam Njeem, Ashok Malhotra, Laura Ciornei, P.Eng*** - The Effect Of Static Preloads On RC Beams And Slabs Subjected To Blast Loads

RESPONSE OF CONTINUOUS RC BEAMS STRENGTHENED USING STRAIN-HARDENING CEMENTITIOUS COMPOSITIES

Ahmed Almaadawy[1], Srishti Banerji[2], Ghada M. Hekal[3], Magdy I. Salama[4]

[1] Graduate Research Assistant, Utah State University, United States, ahmed.almaadawy@usu.edu

[2] Assistant Professor, Utah State University, United States, srishti.banerji@usu.edu

[3] Associate Professor, Menoufia University, Egypt, drghekal@hotmail.com

[4] Associate Professor, Kafrelsheikh University, Egypt, magdy_yakoub@eng.kfs.edu.eg

Corresponding Author: Srishti Banerji, PhD

Department of Civil & Environmental Engineering, Utah State University, Logan, Utah, United States, 84322

Email: srishti.banerji@usu.edu

ABSTRACT

Strain-hardening cementitious composites (SHCC) are becoming a promising material for strengthening structures due to their excellent mechanical properties, high ductility, and micro-crack development characteristics. Previous research has primarily investigated strengthening of simply supported beams, whereas studies on continuous beams are currently lacking. To address this gap, the present study assesses the behavior of reinforced concrete (RC) continuous beams strengthened by reinforced SHCC layers under flexural loading. In the current research, five RC continuous beams were tested; one of which was the control (un-strengthened) beam and the other four were strengthened at the region of mid-support negative moment. SHCC layers were bonded to the RC beam surface using epoxy adhesive along with SHCC reinforcing bars in an anchored manner. The test parameters considered different strengthening configurations (L-shaped with CFRP laminates and U-shaped). The control specimen failed at 391 kN, while the strengthened beams failed at higher loads (418-495 kN). The U-shaped configuration over full beam depth exhibited the highest load capacity (495 kN), resulting in a 27% increase. Measured data from tests were used to validate a finite-element-based numerical model developed using ABAQUS. The measured and predicted load capacity, load-deflection response, and cracking patterns were in good agreement. The numerical model can be utilized for analysing RC continuous beams strengthened by SHCC for future applications.

Keywords: *Reinforced concrete continuous beams, Strain-hardening cementitious composites, Finite element modelling, Debonding failure.*

1. INTRODUCTION

Reinforced concrete (RC) continuous beams are vital structural elements widely used in civil engineering construction due to their versatility and load-bearing capacity. However, over time, these beams may experience deterioration and deficiencies, such as cracking and deflection, which necessitate strengthening interventions. To address the deficiencies and enhance the

load-carrying capacity of RC beams, a range of strengthening techniques have been used in the literature. These include externally bonded systems such as fiber-reinforced polymers (FRP) [1], steel plates [2], and advanced cementitious composites like fiber-reinforced cementitious matrix (FRCM) [3, 4], textile reinforced mortar (TRM) [5]. Among the various techniques available, the use of strain-hardening cementitious composites (SHCC) has emerged as a promising solution for enhancing the performance and durability of RC structures. SHCC is a mortar-based composite that consists of cementitious materials (cement and silica fume) and is reinforced with fibers (typically polypropylene fibers). SHCC is characterized by its ability to undergo strain hardening, which means that even after initial cracking, it continues to carry loads and deform in a plastic manner. The strain hardening occurs due to the bridging and pullout mechanisms of the embedded fibers causing multiple fine cracks, which helps to distribute stress and prevent brittle failure. As the material undergoes deformation, the fibers effectively transfer load and contribute to the composite's ability to strain beyond the cracking point. The typical tensile strength and strain of SHCC can vary depending on the mix design, fiber type, and curing conditions. However, typical values for SHCC include tensile strengths ranging from 4 MPa to 10 MPa and tensile strains exceeding 3% to 5% before failure. These values are higher than that of conventional concrete, which exhibits brittle tensile behavior with limited tensile strength and strain capacity.

Previous experimental studies have demonstrated the efficacy of SHCC layers in retrofitting existing simply supported RC beams, and some of these studies are briefly discussed here. Zhang et al. [6] investigated experimentally and numerically the behavior of simply supported RC beams strengthened using SHCC layers bonded to the bottom surface of the RC beam. In this study, four beams were cast; three of them were strengthened beams with different SHCC layer thicknesses of 10, 30, and 50 mm; and the fourth beam without any strengthening was considered the control beam. The results showed that the load-carrying capacity of the strengthened RC beams increased by 20–60% with the increasing thickness of the SHCC layer. Kim et al. [7] studied experimentally the flexural performance of four simply supported RC beams strengthened with SHCC and high-strength reinforcing steel (HSRS) bars and tested under four-point loading. The experimental findings indicated that the application of SHCC effectively regulated crack width, enhanced stiffness by 23–41%, and increased the load-bearing capacity of the beams by 3–30%, particularly when combined with HSRS bars, which show the highest increase (30%). Hussein et al. [8] conducted tests on the flexural performance of simply supported RC beams strengthened by bottom steel reinforced SHCC layer with a reinforcement ratio of 0.3% and 0.6%. The findings revealed that combining SHCC with tensile steel reinforcement (reinforcement ratio of 0.6%) increased the load-carrying capacity to 100.7 kN, doubling that of the control beam (49 kN). The deflection behavior of the strengthened beams revealed that steel reinforcement within the SHCC layer markedly improved the post-peak performance of the beams. It is crucial to underscore that strengthening RC structures with an unreinforced SHCC layer may result in non-ductile failure.

Previous research has predominantly addressed the strengthening of simply supported RC beams using SHCC. Despite the effective utilization of SHCC in enhancing the strength of simple span RC beams, there remains a dearth of studies exploring its application in strengthening RC continuous beams, which mirrors real-world structural configurations more

closely. This study is the first to capture the flexural behavior of SHCC strengthening continuous RC beams, which makes it novel. Differing from prior research, each beam incorporates a column head above the mid-support to replicate real-world continuous beam configurations, including continuity disruptions. The investigation encompasses the evaluation of different strengthening configurations, including L-shaped with CFRP laminates and U-shaped techniques. Additionally, a finite element model has been developed and validated against the experimental findings to facilitate further numerical parametric studies.

2. EXPERIMENTAL PROGRAM

Five RC continuous beams with two equal spans were fabricated and subjected to testing, with a single point load applied at the midpoint of each span, as shown in Figure 1. The total length of the beam was 3200 mm, split into two equal effective spans of 1550 mm each. All beams have a rectangular cross-section, with dimensions of 150 mm in width and 300 mm in depth. Furthermore, at the midpoint of the beam length, a column head with a height of 200 mm and a square cross-section of 150 mm width was installed. This column head simulates an obstruction, preventing the continuity of strengthening systems. The beams were reinforced with two 16-mm-diameter longitudinal steel rebars at the bottom, along with two 12-mm-diameter steel rebars at the top. Additionally, 8-mm-diameter stirrups were employed for shear reinforcement, evenly spaced at 100-mm intervals. The column reinforcement consisted of four 12 mm-diameter steel rebars and 8 mm-diameter stirrups, spaced equally at 100 mm intervals, as illustrated in Figure 1.

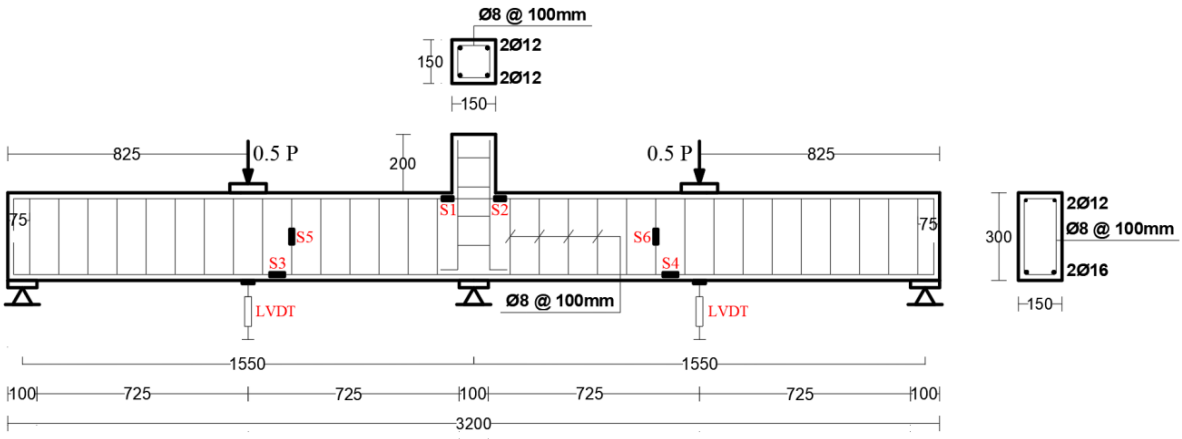

Figure 1. Geometry and reinforcement details of continuous RC beams (all dimensions in mm).

One of the five beams served as a control beam (CB) without any strengthening, while the remaining four beams were strengthened using reinforced SHCC layers. The strengthening configurations consisted of two main types: (i) L-shaped strengthening combined with CFRP laminates, and (ii) U-shaped strengthening. Each configuration was applied to two specimens, and in both configurations, the SHCC layers were attached with longitudinal and transverse reinforcing rebars of 6 mm diameter. For the L-shaped strengthening, one beam utilized an SHCC layer reinforced with longitudinally anchored steel rebars (referred to as specimen SB-LLA), while the other L-shaped beam was reinforced with transversely anchored steel rebars

(referred to as specimen SB-LTA), as depicted in Figure 2a. When anchored, the embedment depth of rebar is 50 mm. Additionally, in the L-shaped specimens, CFRP sheets were wrapped around the column head and the vertical side of the L-shaped layer to enhance the bond between them and enhance strengthening continuity. As for the U-shaped configuration, one beam entailed the full depth of the beam (referred to as specimen SB-UF), while the other utilized half the depth of the beam (referred to as specimen SB-UH), as shown in Figure 2b. In both U-shaped specimens, only the transverse rebars were embedded in the RC beam. The U-shaped strengthening configuration was implemented to strengthen flexure and shear simultaneously. Hence, the horizontal part resists flexural stresses, while the vertical part resists shear forces.

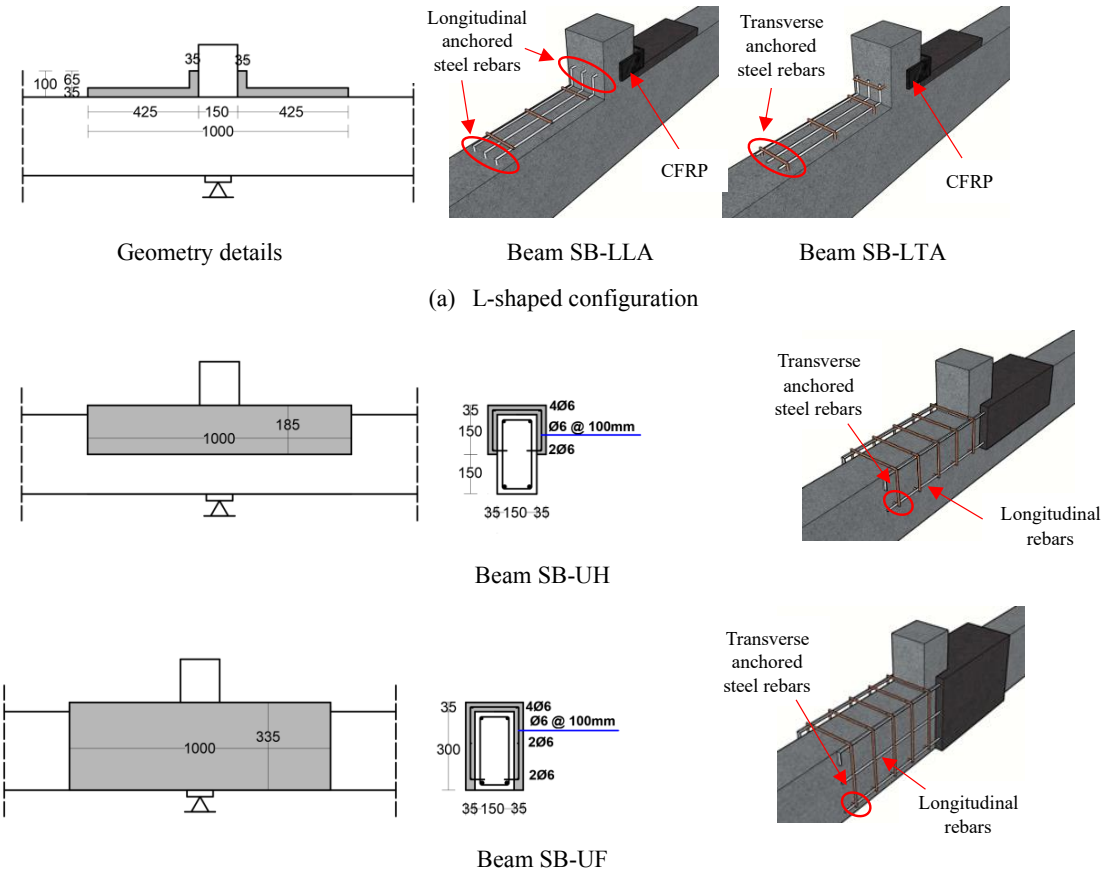

Figure 2. Geometry and reinforcement details of strengthening configurations (all dimensions in mm).

In this study, two types of steel rebars were utilized: ribbed bars with diameters of 12 mm and 16 mm served as the main reinforcement for the RC beam, whereas plain bars with diameters of 6 mm and 8 mm were employed for reinforcing the strengthening layer and as shear reinforcement (stirrups) for the RC beam, respectively.

2.1. Material properties

All samples were fabricated using a conventional normal strength concrete (NSC) mix, which included Portland cement (Type I), fine aggregates (ranging from 0.15 to 4.75 mm in diameter),

coarse aggregates (ranging from 5 to 16 mm in diameter), and water. The strengthening material for all specimens was SHCC, consisting of ordinary Portland cement (Type I), fine aggregate (sand) with a maximum size of 0.5 mm, silica fume, 2% by volume of polypropylene (PP) fibers measuring 12 mm in length and 0.012 mm in diameter, water, and superplasticizer. The mix proportions of NSC and SHCC are provided in Table 1.

Table 1. Mix proportions and mechanical properties of NSC and SHCC

Material	Cement (kg/m^3)	Fine agg. (kg/m^3)	Coarse agg. (kg/m^3)	Water (kg/m^3)	Silica fume (kg/m^3)	PP fiber (kg/m^3)	Superplasticizer (kg/m^3)	Compressive strength (MPa)	Tensile strength (MPa)
NSC	350	535	1279	175	------	------	------	42	3.5
SHCC	1342	157.9	------	312.1	237	16.2	31.6	91	5.8

Compressive strength tests were conducted on cylinder specimens measuring 150 mm in diameter and 300 mm in height. The compressive strength of NSC was 42 MPa, while that of SHCC was 91 MPa. According to the recorded compressive stress-strain curves of NSC and SHCC shown in Figure 3a, SHCC exhibits a more ductile response due to its strain-hardening characteristics. In addition, it can sustain significant deformation and absorb greater energy prior to failure. To determine the tensile strength of both NSC and SHCC, a direct tension test was conducted on dog-bone-shaped specimens. The tension stress-strain characteristics of NSC and SHCC are shown in Figure 3b. Initially, SHCC demonstrates linear-elastic behavior like NSC. However, unlike NSC, SHCC exhibits a distinctive strain-hardening response after surpassing its initial yield point.

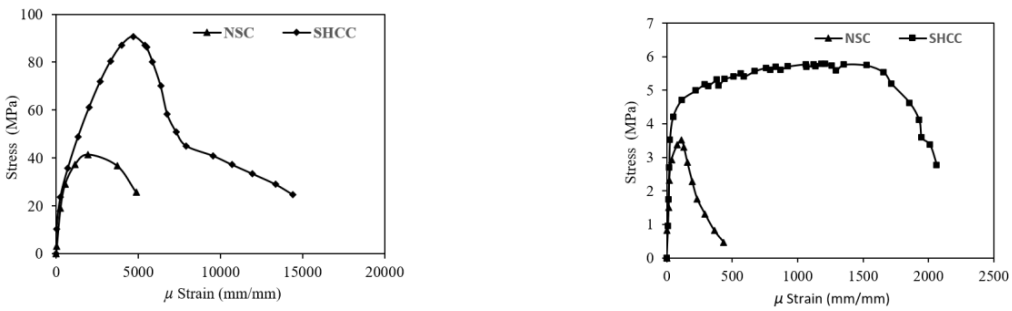

(a) Comressive stress-strain response

(b) Tensile stress-strain response

Figure 3. Stress-strain responses of NSC and SHCC in tension and compression.

Consequently, as tensile stress surpasses the initial yield point, additional microcracks emerged, and the material underwent strain hardening, leading to a simultaneous increase in stress and strain. The tensile strength of SHCC is recorded at 5.8 MPa, while that of NSC is 3.5 MPa. The mechanical properties of NSC and SHCC are summarized in Table 1. Four reinforcing steel bars of varying diameters were used in the current study, including plain bars of diameters 6 and 8 mm and ribbed bars of diameters 12 and 16 mm. A uniaxial tensile test was performed on these bars to determine their mechanical characteristics. The yield strength values for plain and ribbed bars were 280 and 500 MPa, respectively, while their ultimate strength values were 400 and 600 MPa, respectively.

2.2. Strengthening procedure

Initially, all the test beams were cast, and cured for 28 days. Four out of five beams were prepared for strengthening. Firstly, holes were drilled in the RC beam surface for embedding the longitudinal and horizontal reinforcing bars of the SHCC layers. Subsequently, epoxy adhesive was utilized to bond the reinforcement anchors to the RC beam. Following this, RC beam surface was roughened using a jackhammer to enhance the bond between the SHCC and RC beam. Eventually, the surface was cleaned by blowing away the dust, adhesive epoxy was then applied to the entire surface, and finally, the SHCC layers were cast and finished.

2.3. Instrumentation and test setup

All the five test beams were subjected to flexural loading using a five-point loading configuration (2 points for loads and 3 points for supports), as shown in Figure 1. A 1000 kN hydraulic jack applied the load onto a spreader steel I-beam, which, in turn, transferred the load to the RC beams via two solid steel cylinders positioned at both mid-spans of the RC beam. The loading during the test was symmetric, and all specimens were tested to failure under a load-controlled loading due to the limitation of equipment's at a rate of 1 kN/min. Linear variable differential transducers (LVDTs) were affixed at each mid-span beneath the two loading points to measure beam deflections during the test. Each beam was installed with six strain gauges (S1–S6) with a 30 mm gauge length at the critical locations of the reinforcing rebars as shown in Figure 1, to monitor strain and trace the yielding and post-yielding performance of the rebars.

3. RESULTS AND DISCUSSION

In this section, the experimental results will be presented and discussed, focusing on the observed load-deflection response and failure patterns.

3.1. Load-deflection response

The mid-span deflection was measured for each of the spans in the continuous beam on right and left side of the column. The measured data is plotted in Figure 4a for two of the beams (SB-LLA and SB-UF) and as anticipated, the response was almost identical throughout the testing. Hence, for consistency in comparison, the left mid-span deflections are compared for all tested beams in Figure 4b. Table 2 shows a summary of recorded yielding and ultimate peak loads in addition to the corresponding yielding and ultimate deflection, along with the ductility index for all tested specimens. Yielding deflection (Δy) and ultimate deflection (Δu) were monitored at the first yielding load (which was tracked by the strain gauges) and failure (peak) load, respectively. The ductility index represents the ratio between ultimate deflection and yielding deflection.

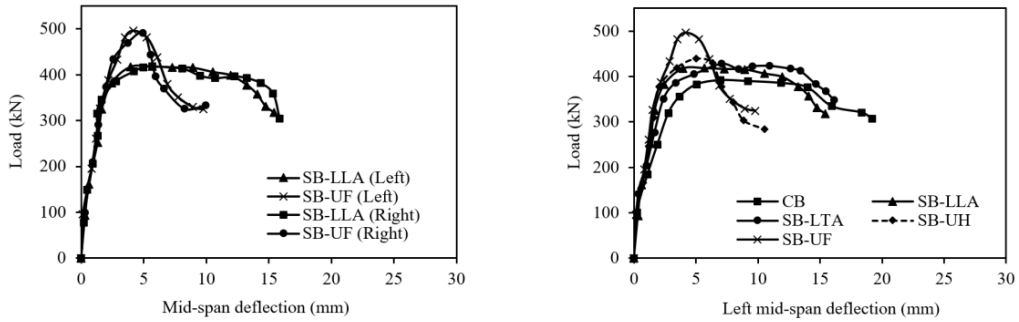

(a) Load-deflection response of left versus right span (b) Load-left midspan deflection response

Figure 4. Load-deflection response of all tested specimens.

Table 2. Measured loads and deflection parameters for all tested beams.

Specimen	Yielding loads (kN)	Ultimate peak loads (kN)	Yielding deflection Δy (mm)	Ultimate deflection Δu (mm)	Ductility index (Δu/Δy)
CB	306	391	1.92	6.97	3.63
SB-LLA	326	418	1.91	5.67	2.97
SB-LTA	330	428	1.87	7.06	3.77
SB-UH	334	439	1.89	4.99	2.64
SB-UF	428	495	2.04	4.18	2.05

3.2. Failure patterns

The failure patterns for all the tested beams are discussed in this section; in addition, the failure patterns of three beams, CB, SB-LTA, and SBUF, are shown in Figure 5. The control beam CB displayed a flexural crack pattern that initiated at locations experiencing high tensile stresses. With increasing load, cracks initiated at midspans, where tensile stresses predominated due to downward beam deflection, and propagated towards the supports, extending longitudinally. The control beam CB exhibited its first crack at a load of 129 kN. L-shaped strengthened beams also exhibited a combination of flexural cracks and splitting flexural cracks, developing at higher loads. However, the first cracking loads of beams SB-LLA and SB-LTA were approximately 10% and 11% higher than the control beam. Notably, both L-shaped strengthened beams experienced flexural failure due to yielding of upper and lower reinforcing bars at mid-support and midspans, respectively. Furthermore, partial debonding failure between SHCC layer and RC beam surface was observed at the end of tests of both L-shaped strengthened beams. In beam SB-LLA, the debonding failure occurred between SHCC layer and the vertical side of the column head, while in beam SB-LTA debonding occurred between the horizontal part of the SHCC layer and the RC beam top face. The occurrence of debonding in both specimens is due to the high concentration of tensile stresses in this region and the discontinuity of the strengthening layer.

In terms of U-shaped strengthening, both the beams demonstrated superior performance compared to the other beams. The upper reinforcing bars at mid-support did not yield and debonding failure was not observed in these specimens because of higher contact area between RC beam surface and SHCC layer. The first cracking load for the U-shaped strengthening specimens, SB-UH and SB-UF, was approximately 24% and 28% higher than that of the control beam, respectively. These U-shaped strengthened beams exhibited a combined failure

pattern of flexural and shear failures. Furthermore, the failure in these beams took place outside the strengthening region. In both U-shaped strengthened beams, the failure sequence commenced with the yielding of bottom reinforcing bars at both mid-spans, followed by shear failure. As observed, the distinctive strain-hardening characteristics of SHCC play a crucial role in enhancing the ultimate peak loads for strengthened specimens. However, as a result of increasing the ultimate flexural resistance for U-shaped specimens, shear failure occurred.

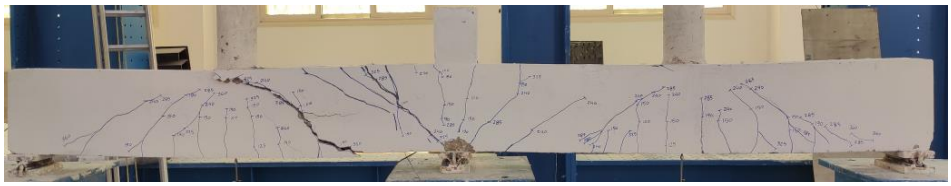

(i) Control specimen CB

(ii) Specimen SB-LTA

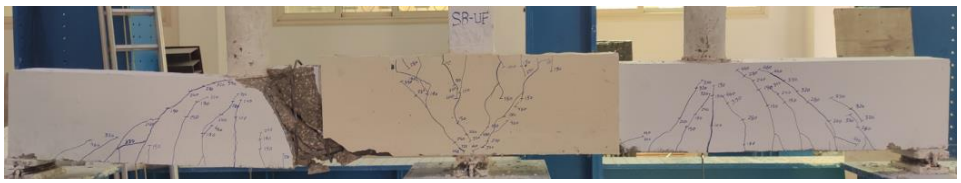

(iii) Specimen SB-UF

Figure 5. Failure patterns of all tested beams.

The failure patterns of all tested specimens were not identical on the two sides of the beams despite application of symmetric loading. This can be attributed to the variations in concrete homogeneity, reinforcement placement, or construction techniques which could have led to differences in structural behavior and crack patterns between the two spans. This phenomenon has been observed in previous studies in the literature [3].

4. NUMERICAL SIMULATION

A non-linear finite element (FE) program (ABAQUS) [9] was used to simulate all the tested beams, aiming to validate the experimental findings by comparing them with the FE results. The simulation of beams entailed utilizing a 3D solid element model, and due to symmetry considerations, only half of the continuous beams were simulated, as in Hekal et al. [10] NSC, SHCC, supports, and loading plates were modeled using eight-node isoperimetric brick elements (Type C3D8), while reinforcing steel bars were simulated using a three-node linear 3D truss (Type T3D3). To mitigate stress concentration, steel plates were positioned under the supports and load. Figure 6 shows the geometry, boundary conditions, and structural elements

utilized in the FE model. A mesh size of 25 mm was used based on a mesh sensitivity analysis. All the beams in the numerical model were tested under displacement-controlled loading.

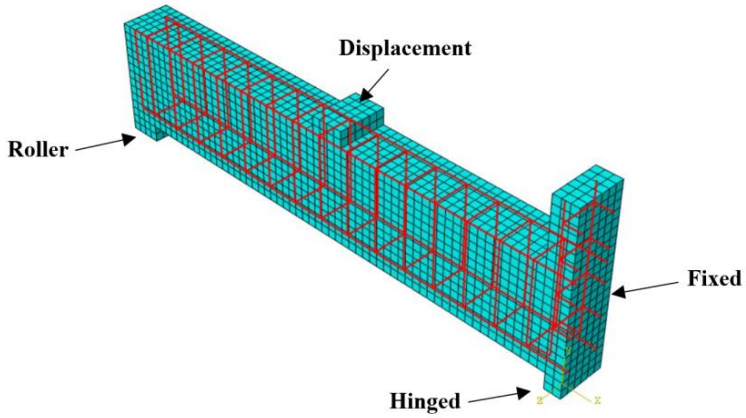

Figure 6. Geometry and boundary conditions used in finite-element modeling.

4.1. Material modelling

The Concrete Damaged Plasticity Model (CDPM) was employed to model NSC and SHCC components in the current study. Stress-strain curves derived from experimental results were utilized to define the nonlinear properties of NSC and SHCC. The Poisson's ratio for NSC and SHCC was assumed to be 0.2 and 0.17, respectively. The modulus of elasticity for NSC and SHCC was 31.6 GPa and 29.1 GPa, respectively. The elastic-perfect plastic relationship is utilized to simulate the behavior of the reinforcing steel bars, with both tension and compression demonstrating similar responses. The finite element (FE) model used the properties of the reinforcing steel bars from the conducted uniaxial tensile tests. Moreover, the modulus of elasticity and Poisson's ratio of reinforcing steel bars are taken as 2×10^5 MPa and 0.3, respectively. The interaction between reinforcing steel bars and RC beam was modeled as an embedded region, [11], where RC beam served as the host region. Moreover, since no instances of debonding failure were observed between the CFRP layers, SHCC, and the concrete column head during the experimental tests, their interaction was regarded as a tie constraint (full bond). The interaction between the SHCC layer and the RC beam surface was utilized as a surface-to-surface contact approach, as in Obaidat et al. [11].

4.2. Numerical validation results

The predicted and measured load-deflection response was compared for all the beams and a comparison for three of the beams (CB, SB-LTA, and SB-UF) are shown in Figure 7. Table 3 shows a summary of numerical ultimate peak loads for all tested beams compared to their experimental loads. For the control beam CB, the model predicted flexural failure similar to the test, with an ultimate peak load of 382 kN in the FE model and 391 kN in experimental tests, indicating a deviation of approximately -2.3%. Regarding the L-shaped strengthening, specimen SB-LLA failed numerically at 405 kN compared to 418 kN experimentally, while specimen SB-LTA experienced a higher numerical failure load (439 kN) compared to its

experimental ultimate peak load of 428 kN. Specimens SB-UH and SB-UF failed numerically at loads of 443 kN and 486 kN, differing by approximately 1.1% and -1.9%, respectively, from their experimental loads. Overall, the experimental ultimate peak loads matched closely with the finite element results for all beams with variations ranging from 0.9% to 3.2%. Moreover, Figure 7 illustrates a close match between the pre-peak behavior in both the FE model and experimental results for all beams. However, differences arise in the post-peak behavior. These differences can be attributed to the use of load-controlled loading in experiments and displacement-controlled loading in the FE model. Load-controlled loading may not fully capture the post-peak behavior compared to displacement-controlled loading. Additionally, boundary constraints such as supports and loading applications in the FE models may not precisely replicate those in the experimental setup.

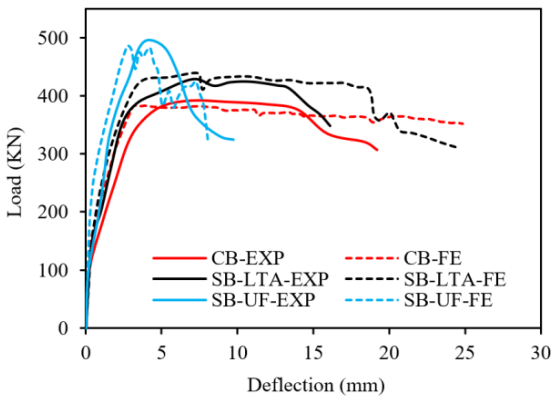

Figure 7. Experimental versus numerical load-deflection responses.

Table 3. Experimental versus numerical ultimate peak loads for all tested beams.

Specimen	Ultimate peak loads (kN)		
	Experimental	Numerical	Experimental/Numerical
CB	391	382	1.024
SB-LLA	418	405	1.032
SB-LTA	428	439	0.975
SB-UH	439	443	0.991
SB-UF	495	486	1.019

5. CONCLUSIONS

The current study presents experimental investigations and numerical validation of RC continuous beams strengthened with reinforced strain-hardening cementitious composites (SHCC) layers under flexural loading. Based on the findings obtained from both experimental and numerical analyses, the following conclusions can be inferred:

- L-shaped SHCC strengthening with CFRP and longitudinal and transversely anchored rebars increased the ultimate peak load compared to the control beam. Utilizing longitudinally anchored rebars resulted in a 6.8% increase in peak load, whereas transversely anchored rebars led to a 9.3% increase.

- U-shaped SHCC strengthening in beams exhibited a greater increase in the ultimate peak load of the control beam as compared to L-shaped strengthening. Using the U-shaped strengthening along the full beam depth resulted in a 27% enhancement in peak load, while strengthening along half beam depth led to a 12% increase.
- While SHCC strengthening increased load-carrying capacity of the RC continuous beams, only 4% ductility increased in beam strengthened with L-shaped SHCC and transversely anchored rebars, whereas ductility decreased in the other three strengthened beams. This reduction in ductility is due to the increase in flexural capacity through strengthening, resulting in a combination of flexural and shear failure instead of pure flexure failure.
- Partial debonding failure between the SHCC layer and the RC beam occurred with L-shaped strengthening due to the high concentration of tensile stresses and the discontinuity of the strengthening. In contrast, with U-shaped strengthening, debonding failure did not occur because of the increased contact area between the RC beam and SHCC layers.
- The developed 3D finite element model incorporates three-dimensional solid elements and cohesive interactions and can effectively predict loads and load-deflection response of RC continuous beams strengthened by SHCC. The experimentally measured loads and predicted values was very close, with differences ranging from 0.9% to 3.2%.

REFERENCES

[1] R. A. Hawileh, H. A. Rasheed, J. A. Abdalla, and A. K. Al-Tamimi, "Behavior of reinforced concrete beams strengthened with externally bonded hybrid fiber reinforced polymer systems," *Mater Des*, vol. 53, pp. 972–982, 2014.

[2] S. Aykac, I. Kalkan, B. Aykac, S. Karahan, and S. Kayar, "Strengthening and repair of reinforced concrete beams using external steel plates," *Journal of Structural Engineering*, vol. 139, no. 6, pp. 929–939, 2013.

[3] A. Mandor and A. El Refai, "Flexural response of reinforced concrete continuous beams strengthened with fiber-reinforced cementitious matrix (FRCM)," *Eng Struct*, vol. 251, p. 113557, 2022.

[4] N. Khattak, M. Mansour, T. El-Maaddawy, and N. Ismail, "Continuous reinforced concrete beams strengthened with fabric-reinforced cementitious matrix: Experimental investigation and numerical simulation," *Buildings*, vol. 12, no. 1, p. 27, 2021.

[5] H. M. Elsanadedy, T. H. Almusallam, S. H. Alsayed, and Y. A. Al-Salloum, "Flexural strengthening of RC beams using textile reinforced mortar–Experimental and numerical study," *Compos Struct*, vol. 97, pp. 40–55, 2013.

[6] Y. Zhang, N. Ueda, H. Nakamura, and M. Kunieda, "Behavior investigation of reinforced concrete members with flexural strengthening using strain-hardening cementitious composite," *ACI Struct J*, vol. 114, no. 2, p. 417, 2017.

[7] Y. Y. Kim, B. Y. Lee, J.-W. Bang, B.-C. Han, L. Feo, and C.-G. Cho, "Flexural performance of reinforced concrete beams strengthened with strain-hardening cementitious composite and high strength reinforcing steel bar," *Compos B Eng*, vol. 56, pp. 512–519, 2014.

[8] M. Hussein, M. Kunieda, and H. Nakamura, "Strength and ductility of RC beams strengthened with steel-reinforced strain hardening cementitious composites," *Cem Concr Compos*, vol. 34, no. 9, pp. 1061–1066, 2012.

[9] D. Systèmes, "ABAQUS Documentation (Dassault Systèmes, Providence, RI)." Version, 2014.

[10] G. M. Hekal, M. I. Salama, G. Elsamak, and A. H. Almaadawy, "Shear behavior of RC beams strengthened with ultra-high-performance fiber-reinforced concrete using finite-element analysis," *Asian Journal of Civil Engineering*, vol. 24, no. 1, pp. 71–91, 2023.

[11] Y. T. Obaidat, S. Heyden, and O. Dahlblom, "The effect of CFRP and CFRP/concrete interface models when modelling retrofitted RC beams with FEM," *Compos Struct*, vol. 92, no. 6, pp. 1391–1398, 2010.

FRP CONFINEMENT-INDUCED ENHANCEMENT IN STRESS-STRAIN BEHAVIOR OF FIRE-DAMAGED CONCRETE COLUMNS: DESIGN-ORIENTED MODEL

Javad Shayanfar[1], and Joaquim A. O. Barros[2]

[1] PhD, ISISE, Department of Civil Engineering, University of Minho, arch3d.ir@gmail.com.

[2] Full Prof., ISISE, IBS, Department of Civil Engineering, University of Minho, barros@civil.uminho.pt.

Corresponding Author: Javad Shayanfar, PhD.

University of Minho, Azurém, Guimarães, Portugal, 4800-058

Email: arch3d.ir@gmail.com

ABSTRACT

Despite several confinement models available in the literature to calculate the axial behavior of fiber-reinforced-polymer (FRP) confined concrete columns at ambient conditions, a reliable design-oriented model to obtain the behavior of heat-damaged concrete columns post-confined with FRP is still lacking. This study aims to address this research gap, by proposing a new model that predicts the effects of FRP confinement on concrete elements with thermal-induced damage. This model proposes a closed-form formulation to derive a stress-strain expression, including a set of strength and strain sub-models to calculate the stress/strain information at transition and ultimate points defining the stress-strain response. To develop the model and calibrate its key components by data analysis of statistical treatment techniques, a large test database of FRP confined unheated/heat-damaged concrete of circular/square cross-section was collected. The proposed design-oriented model is able to demonstrate the influence of pre-existing thermal damage in terms of the stress-strain relationship, whose reliability is revealed comprehensively through predicting data from several experimental heat-damaged concrete specimens confined with FRP systems.

Keywords: *FRP Confinement, Heat-damaged Concrete, Axial Behavior; Stress-strain Model.*

INTRODUCTION

Post-fire experimental research has demonstrated that at fire occurrence, the mechanical, chemical, and physical characteristics of concrete exposed to high temperatures are deteriorated, leading to concrete dehydration, higher porous microstructure, and a decrease of the bond between concrete constituents resulting in stiffness and strength degradation (Kodur [1]). Accordingly, the response of a concrete structure in terms of its serviceability, seismic performance, and durability is influenced noticeably when subjected to high temperatures (Demir et al. [2]). Considering the relatively high cost of reconstruction alternative, the usage of a post-fire strengthening solution for assuring the required performance and strength capacity level of a fire-damaged concrete structure can be justified. Experimental research [3-7] evidenced the potentialities of fiber-reinforced-polymer (FRP) confinement technique for improving the axial strength, ductility and stiffness of heat-damaged concrete columns.

To predict the stress–strain response of FRP confined circular and square concrete (FFCC and FFSC, respectively) under ambient temperatures, many models have been proposed, generally categorized into two groups: analysis-oriented models, AOM, ([10-12) and design-oriented models, DOM, ([13-15]). However, very few AOM and DOM models have been proposed for FRP-confined heat-damaged circular and square concrete (FCHCC and FCHSC, respectively) [3, 16-18]. Bisby *et al.* [3] generalized ACI 440.2R-08 [19] model, which was developed exclusively for FCCC at ambient conditions, in an attempt to predict the axial stress-strain response of FCHCC (at high temperatures). In this model, for the sake of simplicity, the effectiveness/capability of FRP confinement in improving concrete behavior was assumed identical for concrete at ambient and elevated conditions. In other words, the axial strength and strain enhancements induced by confinement on FCHCC were considered the same adopted on FCCC at ambient conditions. The generalized model has predicted conservative values regarding the corresponding experimental results. Ouyang *et al.* [5] assessed the applicability of existing confinement models (Lam and Teng [20], and Ozbakkaloglu and Lim [21]), which were developed exclusively for FFCC, to be generalized to FFHCC by addressing the mechanical characteristics of unconfined heat-damaged concrete. They evidenced that these generalized models predict conservatively the axial response of the test specimens of FFHCC, which was also confirmed by Song *et al.* [6] for FCHSC.

In this paper, a new generalized DOM is developed to predict a stress-strain relation ($f_c - \varepsilon_c$) of FCHCC/FCHSC. This model consists of a closed-form formulation to derive a $f_c - \varepsilon_c$ relationship, which integrates a set of strength and strain sub-models to calculate the stress/strain information at the transition and ultimate points. The initial focus is placed on the determination of the $f_c - \varepsilon_c$ expression including parabolic and linear functions based on experimental observations of axial response of FCHCC/FCHSC with different levels of pre-existing thermal-induced damage. Subsequently, predictive formulations are proposed to calculate stress/strain information at the transition and ultimate stages where the influences of non-circularity and thermal damage level on confinement-induced enhancements are reflected in their determination based on regression analysis.

Proposed stress-strain model

Based on experimental observations [3-7], by increasing exposure temperature from ambient to elevated temperature, the shape of FCHCC/FCHSC's axial response is converted from a parabolic-linear stress-strain relation into an almost linear one. Accordingly, in this study, a new stress-strain model was proposed (Figure 1):

$$f_c = \left(2E_{ctr} - E_2\right)\varepsilon_c - \left(\frac{E_{ctr} - E_2}{\varepsilon_{ctr,T}}\right)\varepsilon_c^{\,2} \qquad \text{for } \varepsilon_c \le \varepsilon_{ctr,T} \tag{1a}$$

$$f_c = f_{ctr,T} + E_2\left(\varepsilon_c - \varepsilon_{ctr,T}\right) \qquad \text{for } \varepsilon_c \ge \varepsilon_{ctr,T} \tag{1b}$$

in which

$$E_{ctr} = \frac{f_{ctr,T}}{\varepsilon_{ctr,T}} \tag{2}$$

$$E_2 = \frac{f_{cu,T} - f_{ctr,T}}{\varepsilon_{cu,T} - \varepsilon_{ctr,T}} \tag{3}$$

where f_c is the axial stress at axial strain (ε_c). $f_{ctr,T}$ is the axial stress at axial strain ($\varepsilon_{ctr,T}$) corresponding to the transition zone. $f_{cu,T}$ is the axial stress at axial strain ($\varepsilon_{cu,T}$) corresponding to the ultimate condition. The proposed model requires information regarding the transition and ultimate stages to be able to calculate the stress-strain response of FRP-confined heat-damaged concrete columns, which will be presented in the following section.

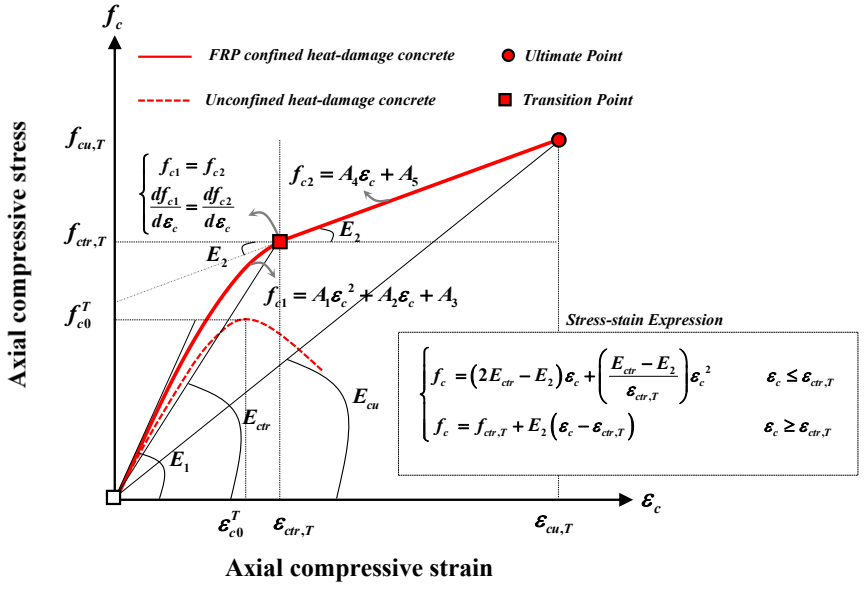

Figure 1. Proposed stress-strain model

Sub-model for Ultimate Stress at Elevated Conditions

For the case of FFCC and FFSC, Shayanfar et al. [18] proposed a new well-calibrated formulation to determine ultimate stress (f_{cu}), as follows:

$$\frac{f_{cu}}{f_{c0}} = 1 + \frac{2.6}{\beta_{SE}\beta_R} K_L^{0.93} f_{c0}^{-1.28} \varepsilon_{fu}^{0.69} \tag{4}$$

in which

$$K_L = 2\frac{n_f^k t_f E_f}{b} \tag{5}$$

$$\beta_{SE} = \left(\frac{b}{150}\right)^{0.2} \le 1.1 \tag{6}$$

$$\beta_R = 0.85\left(R_b\right)^{-0.75} \ge 1 \tag{7}$$

where n_f is the number of FRP layers; t_f is the nominal thickness of a FRP layer; E_f is the FRP elasticity modulus; κ is equal to 1 and 0.85 corresponding to $n_f \le 3$ and $n_f \ge 4$, respectively, according to *fib* bulletin 90 recommendation [22]; b is the column dimension; ε_{fu} is FRP ultimate tensile strain; β_{SE} and β_R represent the terms addressing the effects of column's cross-section dimension and corner radius ratio ($R_b = 2r/b$) on the axial strength enhancements. Experimental evidence shows that increasing T_m , the peak strength of unconfined heat-damage concrete is reduced from f_{c0} at ambient conditions to f_{c0}^T at elevated temperature. Accordingly, the peak axial strength of FCHCC and FCHSC can be determined from Eq. (4) by substituting f_{c0} by f_{c0}^T resulting:

$$\frac{f_{cu,T}}{f_{c0}^T} = 1 + \frac{2.6}{\beta_{SE}\beta_R}\left(K_L\right)^{0.93}\left(f_{c0}^T\right)^{-1.28}\left(\varepsilon_{fu}\right)^{0.69} \tag{8}$$

A close look at Eq. (8) demonstrates that the effectiveness of the FRP confining system on FCHCC/FCHSC is assumed the same as that of FCCC/FCSC with identical concrete strength. To highlight the effect of pre-existing thermal damage on the effectiveness of the FRP confinement system, the ratio of confinement-induced enhancements obtained analytically over experimentally, defined by an error index Y_1 ($=\left(f_{cu,T}/f_{c0}^T - 1\right)^{Ana} \Big/ \left(f_{cu,T}/f_{c0}^T - 1\right)^{Exp}$) is evaluated in Figure 2a.

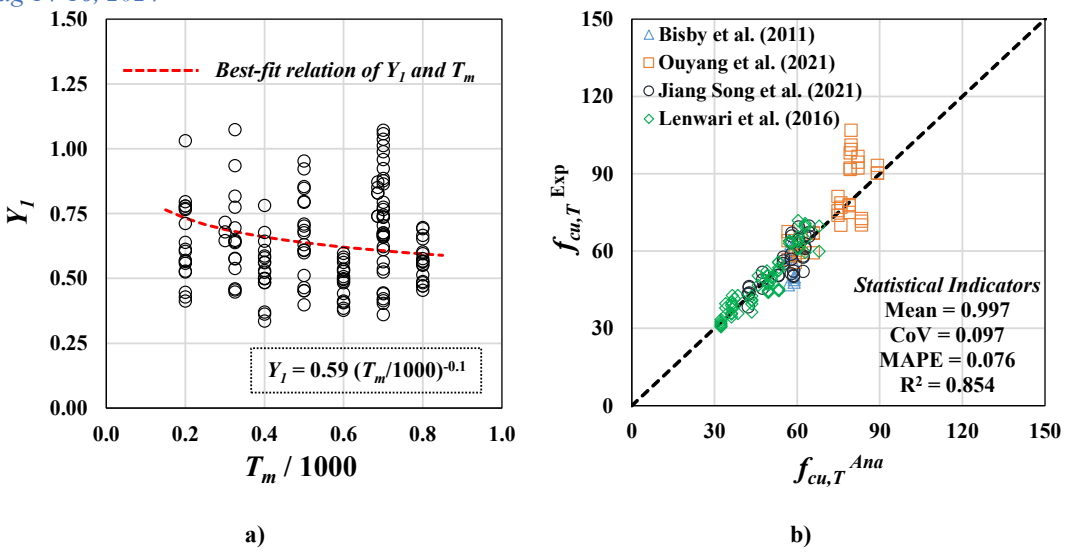

Figure 2. The predictive performance of a) Eq. (8); b) Eq. (11)

As can be seen, Eq. (8) results in substantial underestimations in terms of f_{cu} by increasing T_m imposed to concrete. It shows the necessity of considering the thermal damage influence on the effectiveness increase of the FRP confinement imposed on heat-damaged concrete. Accordingly, applying regression analysis to the experimental data of FCHCC/FCHSC [3-6], the best-fit expression of Y_1 versus T_m relation was derived as $Y_1 = 0.59\left(T_m/1000\right)^{-0.1} \le 1$. By reflecting the influences of concrete strength (f_{c0}), corner radius ratio (R_b), and cooling regime (in water or air) in the developed Y_1 based on the experimental data, the following extra calibration factor is added to Eq. (8):

$$\beta_T = 7.25\beta_{cm}\beta_{T0}\left(\frac{1.2-0.2R_b}{f_{c0}^{\,0.72}}\right)\left(\frac{T_m}{1000}\right)^{-0.1} \le 1 \tag{9}$$

in which

$$\beta_{T0} = 2-5\left(\frac{T_m}{1000}\right) \le 1 \tag{10}$$

and β_{cm} is equal to 1 and 1.175 for the air-cooling method and water-cooling method, respectively, obtained based on the experimental results reported by Lenwari *et al.* [4]. Hence, by introducing β_T (Eq. (9)) reflecting the thermal damage influence on FRP confinement-induced improvements into Eq. (8), the peak axial strength of FCHCC and FCHSC ($f_{cu,T}$) can be calculated as:

$$\frac{f_{cu,T}}{f_{c0}^{T}} = 1 + \frac{2.6}{\beta_{SE}\beta_{R}\beta_{T}} K_{L}^{\ 0.93} f_{c0}^{T-1.28} \varepsilon_{fu}^{\ 0.69} \tag{11}$$

It should be noted that, for concrete at room temperature, β_T is equal to 1, therefore Eq. (11) degenerates in Eq. (4), which represents the successful establishment of the exposure temperature unification in the strength model development. Figure 2b compares the results obtained experimentally from Bisby *et al.* [3], Lenwari *et al.* [4], Ouyang *et al.* [5] and Song *et al.* [6] with those predicted by the proposed unified model. As can be seen, the model is able to predict closely the experimental data of FCHCC/FCHSC confirming its suitable predictive performance.

Sub-model for Ultimate Strain at Elevated Conditions

For the case of FFCC and FFSC, Shayanfar et al. [18] proposed a new well-calibrated formulation to determine ultimate strain (ε_{cu}), as follows:

$$\frac{\varepsilon_{cu}}{\varepsilon_{c0}} = \frac{300}{\alpha_{SE}\alpha_{R}} K_{L}^{\ 0.56} f_{c0}^{\ -0.78} \varepsilon_{fu}^{\ 1.17} \tag{12}$$

in which

$$\alpha_{SE} = \left(\frac{b}{150}\right)^{0.12} \le 1 \tag{13}$$

$$\alpha_{R} = \left(2.2 - 7R_{b}\right) \frac{\mathrm{e}^{-170X_{r}}}{R_{b}^{\ 0.2}} \ge \frac{\mathrm{e}^{-170X_{r}}}{R_{b}^{\ 0.2}} \tag{14}$$

$$X_{r} = \left(1 - R_{b}\right) \varepsilon_{fu} / f_{c0} \tag{15}$$

where α_{SE} and α_{R} represent the terms addressing the effects of the column's cross-section dimension and corner radius ratio on the axial strength enhancements. For the determination of the ultimate strain ($\varepsilon_{cu,T}$) of FCHCC/FCHSC, the approach already adopted for the ultimate stress of FCCC/FCSC at elevated conditions was taken, by replacing the concrete characteristics at ambient conditions for those at heat-damaged conditions. Accordingly, based on Eq. (12), by substituting f_{c0} and ε_{c0} with f_{c0}^{T} and ε_{c0}^{T}, respectively, $\varepsilon_{cu,T}$ is derived as:

$$\frac{\varepsilon_{cu,T}}{\varepsilon_{c0}^{T}} = \frac{300}{\alpha_{SE}\alpha_{R}} \left(K_{L}\right)^{0.56} \left(f_{c0}^{T}\right)^{-0.78} \left(\varepsilon_{fu}\right)^{1.17} \tag{16}$$

By defining a reduction factor α_T considering an error index of Eq. (16) ($\alpha_T = \varepsilon_{cu,T}^{Ana} / \varepsilon_{cu,T}^{Exp}$), the predictive performance of Eq. (16) can be evaluated concerning thermal damage level based on the existing experimental data. As can be seen in Figure 3a, Eq. (16) overestimates remarkably the experimental counterparts ($\alpha_T \geq 1$), which highlights the necessity for considering a reduction factor in Eq. (16) to decrease the confinement-induced improvements with T_m in terms of $\varepsilon_{cu,T}$.

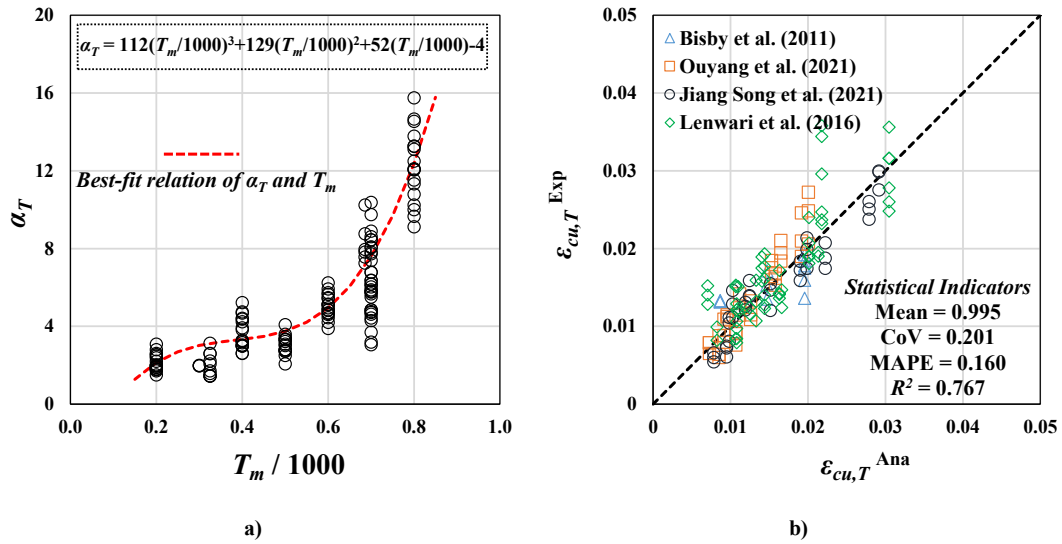

Figure 3. The predictive performance of a) Eq. (16); b) Eq. (18)

Accordingly, based on regression analysis performed on 141 experimental data, the best-fit expression of α_T versus T_m relation was derived as a 3rd degree polynomial equation format (Figure 7a):

$$\alpha_T = \alpha_{cm}\left[112\left(\frac{T_m}{1000}\right)^3 - 129\left(\frac{T_m}{1000}\right)^2 + 52\left(\frac{T_m}{1000}\right) - 4\right] \geq 1 \tag{17}$$

where α_{cm} is equal to 1 and 0.65 for air-cooling method and water-cooling method, respectively, obtained based on the experimental results reported by Lenwari *et al.* [4]. By introducing the parameter α_T, from Eq. (17) into Eq. (16), $\varepsilon_{cu,T}$ of FCHCC/FCHSC can be proposed as:

$$\frac{\varepsilon_{cu,T}}{\varepsilon_{c0}^{T}} = \frac{300}{\alpha_{SE}\alpha_R\alpha_T} K_L^{0.56} f_{c0}^{T-0.78} \varepsilon_{fu}^{1.17} \tag{18}$$

where the model has a unified character with the case of concrete at the room temperature (FCCC/FCSC with $\alpha_T = 1$). In Figure 3b, the performance of the proposed model is assessed based on the experimental results reported by Bisby *et al.* [3], Lenwari *et al.* [4], Ouyang *et al.* [5] and Song *et al.* [6]. It shows that there is a good agreement between both the experimental and analytical data of FCHCC/FCHSC. As a result, by calculating $f_{cu,T}$ and its corresponding strain of $\varepsilon_{cu,T}$, by Eq. (11) and (18), respectively, their information can be addressed for the determination of stress-strain relation model.

Sub-model for Transition Point at Elevated Conditions

For the case of heat-damaged concrete with FRP confinement, by adopting the formulation suggested by Shayanfar et al. [13] developed for cases at room temperature, the axial strain ($\varepsilon_{ctr,T}$) corresponding to the transition zone was suggested as:

$$\frac{\varepsilon_{ctr,T}}{\varepsilon_{c0}^{T}} = 0.45\left(f_{c0}^{T}\right)^{0.25} + 0.0075K_L^{0.37} \geq 1 \tag{19}$$

Therefore, through calculating $\varepsilon_{ctr,T}$ by Eq. (19), the corresponding stress ($f_{ctr,T}^{Exp}$) can be found from experimental axial responses of FCHCC/FCHSC. Experimental observations (i.e. Bisby *et al.* [3]) have evidenced that by increasing the level of thermal damage (T_m), the difference between column axial stiffness at the transition zone ($E_{ctr} = f_{ctr,T}/\varepsilon_{ctr,T}$) and at the ultimate stage ($E_{cu} = f_{cu,T}/\varepsilon_{cu,T}$) decreases considerably. For FCHCC/FCHSC with severe thermal damage (around $T_m = 800$ °C), the column behaves almost linearly with a constant axial stiffness ($E_{ctr} \simeq E_2$). Therefore, by introducing ψ_T as the ratio of E_{ctr} and E_{cu} ($\psi_T = E_{ctr}/E_{cu}$), $f_{ctr,T}$ can be expressed as $f_{ctr,T} = \psi_T E_{cu}\varepsilon_{ctr,T}$. In Figure 4a is represented the variation of ψ_T with T_m based on the test data extracted from the experiments [3-6]. It can be seen that ψ_T decreases with the increase of T_m. By performing regression analysis with the experimental results, it was obtained $\psi_T = 6.74\left[4.5 - 3.5\left(T_m/1000\right)\right]$ for the best fit relation. By considering other influential factors (K_L and R_b) in the regression analysis of ψ_T and T_m variables, a new expression was proposed for the calculation of $f_{ctr,T}$ as follows:

$$f_{ctr,T} = \psi_T \frac{f_{cu,T}\varepsilon_{ctr,T}}{\varepsilon_{cu,T}} \geq f_{c0}^{T}\left(1 + 0.029\sqrt{\frac{K_L}{f_{c0}^{T}}}\right) \leq f_{cu,T} \tag{20}$$

in which

$$\psi_T = \frac{\left(K_L\right)^{0.3}}{\psi_0\left(R_b\right)^{0.15}}\left[0.43 - 0.33\left(\frac{T_m}{1000}\right)\right] \tag{21}$$

$$\psi_0 = \left(\frac{200}{T_m}\right) \geq 1 \tag{22}$$

Figure 4b shows the performance of Eq. (20) against the experimental results ([3-6]), being evident the capability of the model to provide accurate predictions of the counterpart data.

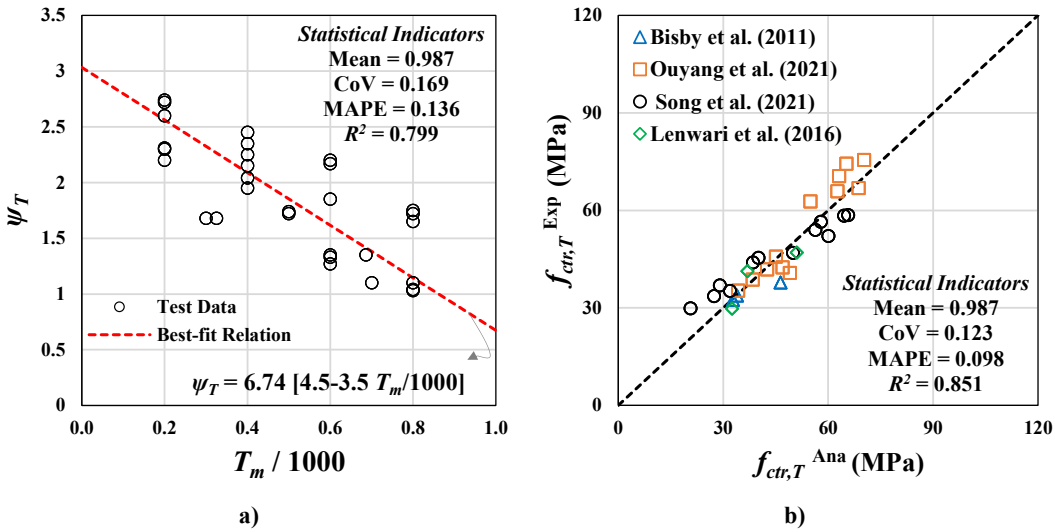

Figure 4. a) Relation of ψ_T with T_m; b) Predictive performance of Eq. (20)

Verification of the Proposed Design-oriented Model

In this section, the verification of the design-oriented model (DOM) developed in the present study to predict the axial stress versus axial strain relationship of FRP fully confined heat-damaged circular/square cross-section concrete columns under axial compressive loading is demonstrated. For this purpose, experimental stress-strain data are compared to those obtained analytically from the proposed DOM. For a further assessment of the developed stress-strain model (Eq. (1)), the well-established stress-strain model developed by Teng *et al.* [23] (suggested exclusively for cases at room temperature) was generalized for FRP fully confined concrete with pre-existing thermal damage. In this model, ultimate stress and strain values were calculated based on the well-calibrated models proposed in this study (Eqs. (11) and (18)).

The calculation process of the proposed DOM to obtain the axial stress versus strain relationships of heat-damaged/unheated concrete confined by FRP is based on the following steps:

i) Calculate the axial strain at the ultimate stage ($\varepsilon_{cu,T}$) using Eq. (18)

ii) Calculate the axial stress at the ultimate stage ($f_{cu,T}$) using Eq. (11)

iii) Calculate the axial strain at the transition zone ($\varepsilon_{ctr,T}$) using Eq. (19)

iv) Calculate the axial stress at the transition zone ($f_{ctr,T}$) using Eq. (20)

v) Assume a level of axial strain (ε_c)

vi) Calculate the corresponding axial stress (f_c) using Eq. (1)

vii) Draw f_c versus ε_c relationship

In the present study, the well-calibrated models developed by Shayanfar *et al.* [16] was followed to calculate the mechanical characteristics of unconfined heat-damaged concrete columns (f_{c0}^T and ε_{c0}^T). Furthermore, to calculate axial strain (ε_{c0}) corresponding to f_{c0}, the well-calibrated formulation recommended by Shayanfar *et al.* [12] was adopted as $\varepsilon_{c0} = 0.0011\left(f_{c0}L/b\right)^{0.25}$ where L is the height of the specimens.

Figure 11 compares analytical simulations obtained from the proposed model and the generalized Teng *et al.* [23]'s model with results measured experimentally [3-6, 23, 25]. As can be seen, by using the generalized Teng *et al.* stress-strain base model [23], despite accurate agreement between analytical and experimental results for the unheated case, misleading predictions are obtained, particularly for FCHCC/FCHSC with severe thermal-induced damage. However, the proposed DOM is able to predict the experimental counterparts with the various levels of pre-existing thermal-induced damage with a good precision.

SUMMARY and CONCLUSIONS

This paper proposed a new generalized design-oriented (DOM) model to analytically calculate the axial response of FRP confined heat-damaged circular/square concrete columns (FCHCC/FCHSC). Based on experimental observation of axial stress-strain curves, a closed-form formulation including parabolic and linear functions was developed that integrates a set of strength and strain sub-models to calculate the stress/strain information at the transition and ultimate points. To have a unified model for concrete at the room and elevated temperature conditions, initially, predictive formulations calculating stress/strain information at the transition and ultimate stages were adopted. Then, by applying them to 109 FCHCC and 35 FCHSC test specimens, the substantial influence of thermal-induced damages on these key stages was investigated and reflected empirically in the model establishment as a function of the level of maximum temperature exposed to the concrete. The proposed DOM model demonstrated an appropriate performance in the simulation of the axial stress-strain of FCHCC/FCHSC, compared to existing modeling solutions.

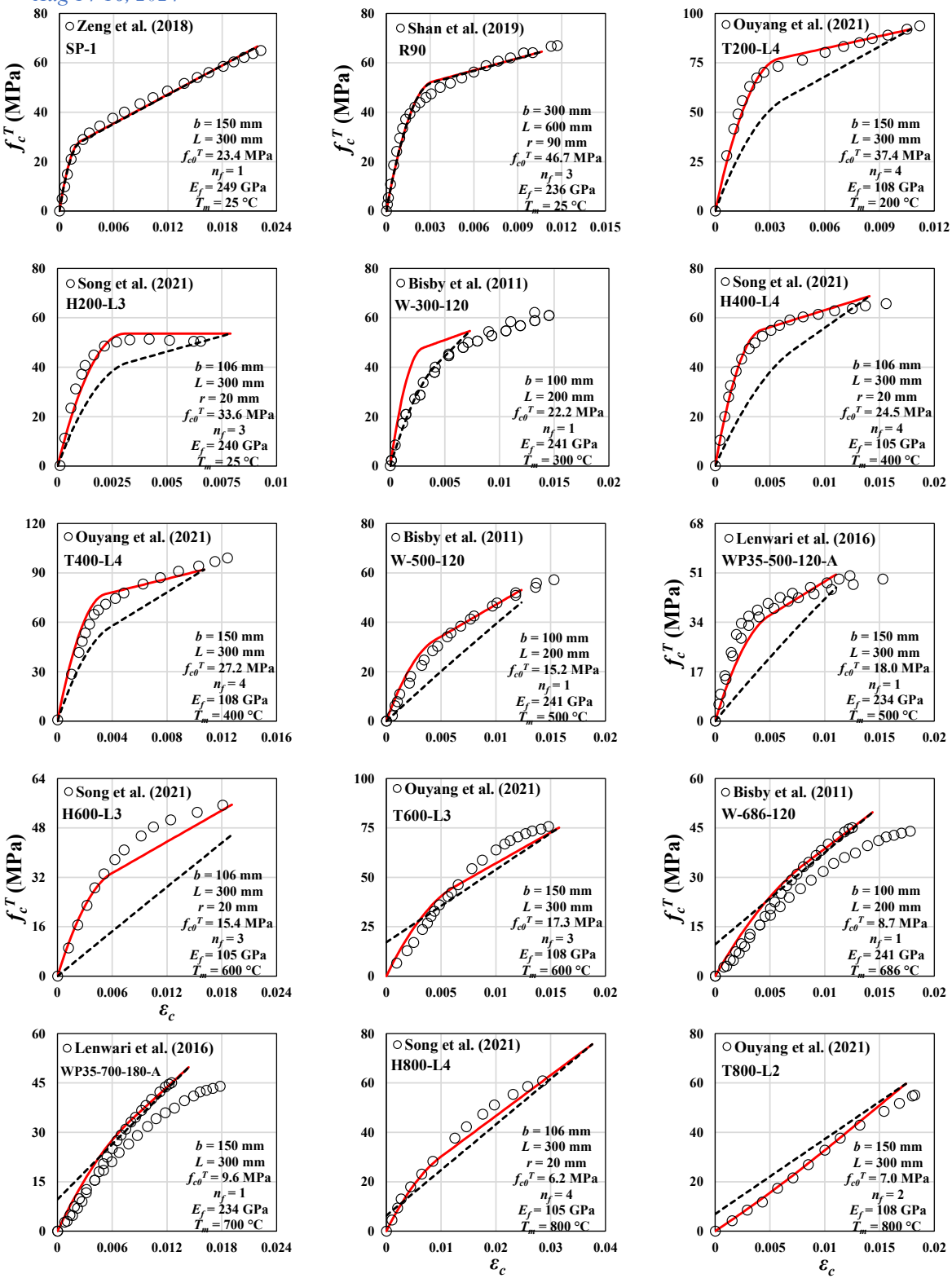

Figure 5. Anaytical simulations against experimental data

ACKNOWLEDGMENTS

This study is a part of the project "Sticker –Innovative technique for the structural strengthening based on using CFRP laminates with multifunctional attributes and applied with advanced cement adhesives", with the reference POCI-01-0247-FEDER-039755. The first author also acknowledges the support provided by CAIXILHARIA MINIMALISTA project with the reference of "FELLOW_BI/I&D/PIEP/01-2023/2023". This work was partly financed by FCT / MCTES through national funds (PIDDAC) under the R&D Unit Institute for Sustainability and Innovation in Structural Engineering (ISISE), under reference UIDB/04029/2020, and under the Associate Laboratory Advanced Production and Intelligent Systems ARISE under reference LA/P/0112/2020.

REFERENCES

[1] Kodur, V. (2014). Properties of concrete at elevated temperatures. *International Scholarly Research Notices*.

[2] Demir, U., Green, M. F., & Ilki, A. (2020). Postfire seismic performance of reinforced precast concrete columns. *PCI Journal*, 65(6).

[3] Bisby, L. A., Chen, J. F., Li, S. Q., Stratford, T. J., Cueva, N., & Crossling, K. (2011). Strengthening fire-damaged concrete by confinement with fibre-reinforced polymer wraps. *Engineering Structures*, 33(12), 3381-3391.

[4] Lenwari, A., Rungamornrat, J., & Woonprasert, S. (2016). Axial compression behavior of fire-damaged concrete cylinders confined with CFRP sheets. *Journal of Composites for Construction*, 20(5), 04016027.

[5] Ouyang, L. J., Chai, M. X., Song, J., Hu, L. L., & Gao, W. Y. (2021). Repair of thermally damaged concrete cylinders with basalt fiber-reinforced polymer jackets. *Journal of Building Engineering,* 44, 102673.

[6] Song, J., Gao, W. Y., Ouyang, L. J., Zeng, J. J., Yang, J., & Liu, W. D. (2021). Compressive behavior of heat-damaged square concrete prisms confined with basalt fiber-reinforced polymer jackets. *Engineering Structures,* 242, 112504.

[7] Elhamnike, S. M., Abbaszadeh, R., Razavinasab, V., & Ziaadiny, H. (2022). Behavior and modeling of post-heated circular concrete specimens repaired with fiber-reinforced polymer composites. *Advances in Structural Engineering*, 25(3), 541-551.

[8] Teng J, Huang YL, Lam L, Ye LP. Theoretical model for fiber-reinforced polymer-confined concrete. *Journal of Composites for Construction*, 2007;11(2):201-210.

[9] Lim JC, Ozbakkaloglu T (2014). Unified stress-strain model for FRP and actively confined normal strength and high-strength concrete. . *J Compos Constr,* 19(4):04014072.

[10] Shayanfar, J., Barros, J. A., & Rezazadeh, M. (2021). Generalized analysis-oriented model of FRP confined concrete circular columns. *Composite Structures*, 270, 114026.

[11] Shayanfar, J., Barros, J. A., & Rezazadeh, M. (2022). Unified model for fully and partially FRP confined circular and square concrete columns subjected to axial compression. *Engineering Structures*, 251, 113355.

[12] Shayanfar, J., Barros, J. A., & Rezazadeh, M. (2023). Analysis-oriented model for partially FRP-and-steel-confined circular RC columns under compression. *Engineering Structures*, 276, 115330.

[13] Shayanfar, J., Barros, J. A., & Rezazadeh, M. (2024). Design-oriented stress–strain model for RC columns with dual FRP-steel confinement mechanism. *Composite Structures*, *330*, 117821.

[14] Shayanfar, J., Barros, J. A., & Rezazadeh, M. (2024). Stress–Strain Model for FRP-Confined Circular Concrete Columns Developing Structural Softening Behavior. *Journal of Composites for Construction*, 28(1), 04023065.

[15] Shayanfar, J., Barros, J. A., Abedi, M., & Rezazadeh, M. (2023). Unified compressive strength and strain ductility models for fully and partially FRP-confined circular, square, and rectangular concrete columns. *Journal of Composites for Construction,* 27(6), 04023053.

[16] Shayanfar, J., Barros, J. A., & Rezazadeh, M. (2023). Stress–strain model for FRP confined heat-damaged concrete columns. *Fire Safety Journal,* 136, 103748.

[17] Shayanfar, J., Kafshgarkolaei, H. J., Barros, J. A., & Rezazadeh, M. (2022). Unified Strength Model for FRP Confined Heat-damaged Circular and Square Concrete Columns. *Composite Structures*, 116647.

[18] Shayanfar, J., Barros, J. A., & Rezazadeh, M. (2023). Analytical model to predict axial stress-strain behavior of heat-damaged unreinforced concrete columns wrapped by FRP jacket. *Engineering Structures*, *289*, 116244.

[19] ACI. Guide for the design and construction of externally bonded FRP systems for strengthening concrete structures, ACI 440.2R-08. *Farmington Hills (MI, USA): American Concrete Institute;* 2008.

[20] Lam, L., and Teng, J. G. (2003). "Design-oriented stress-strain model for FRP-confined concrete." *Constr. Build. Mater.,* 17(6), 471–489.

[21] Ozbakkaloglu, T., & Lim, J. C. (2013). Axial compressive behavior of FRP-confined concrete: Experimental test database and a new design-oriented model. *Composites Part B: Engineering,* 55, 607-634.

[22] Fib Bulletin 90 (2019). Externally applied FRP reinforcement for concrete structures. Task Group 5. 1, *International Federation for Structural Concrete*.

[23] Teng, J. G., Jiang, T., Lam, L., & Luo, Y. Z. (2009). Refinement of a design-oriented stress-strain model for FRP-confined concrete. . *J Compos Constr*, 13(4), 269.

[24] Zeng JJ, Guo YC, Gao WY, Chen WP, Li LJ (2018). Stress-strain behavior of concrete in circular concrete columns partially wrapped with FRP strips. *Compos Struct*, 200:810-828.

[25] Shan B, Gui FC, Monti G, Xiao Y (2019). Effectiveness of CFRP confinement and compressive strength of square concrete columns. *J Compos Constr* 23(6):04019043.

NUMERICAL STUDY ON THE PERFORATION OF COATED RC PANELS BY HARD PROJECTILES

Roouf Un Nabi Dar[1] and Dr. P. Alagappan[2]

[1] PhD scholar, Department of Civil Engineering, Indian Institute of Technology Madras, Chennai, Tamil Nadu - 600036, India., roufunnabi16@gmail.com

[2]Assistant Professor, Department of Civil Engineering, Indian Institute of Technology Madras, Chennai, Tamil Nadu - 600036, India., alagappan@civil.iitm.ac.in

Corresponding Author: Dr. P. Alagappan, PhD

Department of Civil Engineering, Indian Institute of Technology Madras, Chennai, Tamil Nadu, India, 600036

Email: alagappan@civil.iitm.ac.in

ABSTRACT

Limited literature is available on strengthening techniques of reinforced concrete (RC) panels for extreme loading like hard projectile impact. This paper critically investigates the ballistic behavior of RC panels safeguarded by protective layers when subjected to hard projectile impact. RC panel of size 1 m × 1 m× 0.12 m along with hemispherical nosed projectile are modeled and analysed numerically using LS Dyna. The ballistic limit of the uncoated RC panel is studied, followed by studying the influence of polyurea coatings on its perforation characteristics. Various thicknesses of polyurea coatings are considered on the front and back faces of the panel. The ballistic resistance is studied in terms of crater formation, depth of penetration (DOP), and deceleration of the projectile. Results show that polyurea thickness in the range of 2 to 5 mm on the front/impact face plays a significant role in enhancing the ballistic resistance of the RC panel. Notably, improvements beyond 5 mm thickness are negligible. Additionally, the study reveals that applying polyurea coating on the impact face of the panel proves more effective than on its back face.

Keywords: *Impact, RC panel, Polyurea, Damage, Penetration, Crater, Finite element modeling*

1. INTRODUCTION

Critical structures and facilities, such as the walls of nuclear power plants, military bunkers, and the shelters of surface amenities like runways, are made of concrete [6, 7, 8, 28]. Due to immense applications and strategic importance, it is crucial to protect these facilities against projectile impact. The hard projectile impact can result in localised damage or even the collapse of the entire structure, especially reinforced concrete (RC) structures. Typical failure modes of RC panels under hard projectile impact are perforation of the projectile, spalling (ejection of material from the impact face), scabbing (ejection of material from the back face), cone cracking, and global failure [15, 18].

Consequently, extensive experimental and numerical studies were carried out on the effects of projectiles/missiles concrete panels by various researchers [1, 14, 15, 21, 22, 26, 36]. Studies considered various factors like concrete grades, thicknesses, carbon fiber-reinforced plastic (CFRP), projectile and target geometries, and velocity ranges. The use of high-strength concrete, along with ultra-high-performance concrete (UHPC) were considered in various studies [5, 15, 26, 30]. The use of high-strength concrete, ultra-high-performance concrete (UHPC), different reinforcement ratios, CFRP, and high thickness are attempted to improve the ballistic performance of RC panels under hard projectile impact. However, polyurea, a new protective material, has attracted a large number of researchers in different protective fields [4, 16, 17, 23, 29, 32, 33]. Polyurea is regarded to have high energy absorbing capacity due to excellent quasi-static and dynamic mechanical properties [35]. Under high-strain loading conditions, the predominant mechanisms of energy dissipation in polyurea are regarded as shock-wave-induced hard domain ordering and crystallization, alongside rearrangements and neutralization. These processes are accompanied by viscoelastic dissipation within the material, leading to improved mechanical characteristics owing to the strain rate effect and the impedance mismatch between the polyurea and its substrate. The protection mechanism is shown in Figure1. Most of the studies using polyurea coating as a strengthening technique focused on improving the ballistic resistance of metallic structures [18, 23]. Also, the use of polyurea coatings in the case of RC structural components was examined majorly for blast loading only. The same was observed to improve the blast resistance of RC structures [35]. Very few impact studies on polyurea coated concrete structures focused on low velocity impacts (drop weight) and global behaviour [29, 34]. The influence of polyurea coating on local damage parameters and the effect of polyurea thickness and location remains to be comprehensively evaluated. Hence, this study examines the impact perforation characteristics of polyurea-coated RC panels. The influence of different thicknesses of coatings on the front and back faces of RC panels is studied in terms of penetration, crater formation, and projectile deceleration.

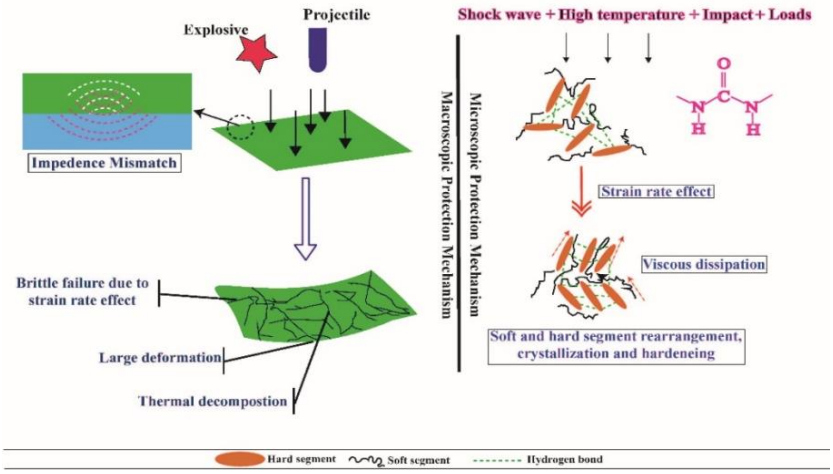

Figure 1: Schematic representation of the protection mechanisms of polyurea coatings [35]

2. NUMERICAL MODELING

2.1 FE modeling

A 3D FE model is created to simulate the RC target and projectile using LS-Dyna [24]. RC panels of dimensions 1 m×1 m with varying thicknesses are modeled based on the experimental work of Kojima [20] (see Figure 2). Numerous uncoated RC panels of different thicknesses subjected to ogive-nosed hard projectile impact are first validated from the experimental results of Kojima [20]. Uncoated RC panels are considered for validation purposes due to a lack of experimental data for coated panels. After successful validation, extended analyses are carried out on a coated RC panel sized 1 m × 1 m × 0.12 m. The RC panel is protected by polyurea coating of varying thick-nesses. A hemispherical-nosed rigid projectile is used in the study (see Figure 2).

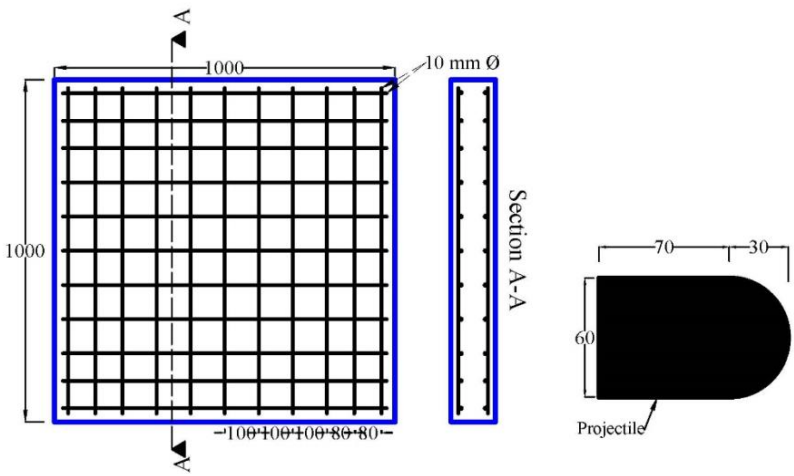

Figure 2: RC panel and projectile. All dimensions in mm

The dynamic explicit algorithm in LS-Dyna is used for this nonlinear dynamic analysis. A mesh convergence study was carried out, and consequently, a refined mesh consisting of 1 mm mesh size across the face and 3 mm mesh size along the depth in the impact region of the concrete panel was used. Mesh size is spatially increased from the impact area towards the boundary of the panel. The criterion used for mesh convergence was the convergence of residual velocity (RV) as followed in most projectile impact studies [19, 31]. The meshed model is shown in Figure 3. An eight-noded brick element with reduced integration was

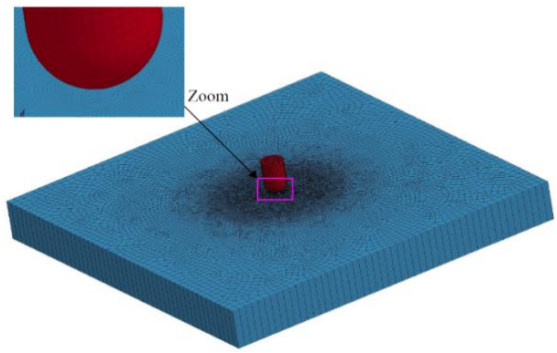

Figure 3: Finite element meshed model showing the projectile and panel. A close-up view of the impacting region is also shown.

adopted to model concrete. Hourglass control was employed in the study along with the Flanagan-Belytschko stiffness form to avoid the hourglassing issue. Reinforcement was modeled as a beam element). The polyurea was modeled using a four-noded quadrilateral, Belytschko–Tsay shell element. The projectile was modeled as a rigid shell element. A rigid support condition is considered for the RC panel in all the simulations since the boundary conditions have the least effect on local damage parameters when the diameter of a projectile is small compared to the panel length and width [2, 10]. Loading scenarios are created by imparting velocity to the projectile. Eroding surface-to-surface contact is employed wherein the whole projectile acts as the master surface and concrete/polyurea as the slave surfaces. Eroding con-tact types are used when the solid components in the contact definition may undergo erosion, leading to the deletion of elements due to material failure criteria. Moreover, for simplicity, no slip is ensured between the polyurea coating and the RC surface. The constitutive models used for concrete, steel reinforcement, and polyurea are described in section 2.2.

2.2 Constitutive models

The Continuous Surface Cap Model (CSCM) is used to model concrete. This model assumes that yielding is a result of the prolonged hydrostatic loading. The model uses a combined deviatoric and volumetric failure sur-face to represent the yield and flow of concrete. The model accounts for triaxial stress, damage, and strain rate effects in addition to employing an ultimate failure surface to simulate shear failure and cap hardening. The third invariant of the deviatoric stress tensor, which is directly proportional to the angle in the deviatoric plane, affects the strength model and is rep-resented by the Rubin scaling function. The mathematical background and formulations of the model are detailed in the LS-Dyna manual [12].

Rebars are modeled using a Plastic Kinematic model, an elastoplastic material with failure strain. A 20 % failure strain is assigned for eroding the reinforcement [13]. This model is suitable for simulating both isotropic and kinematic hardening plasticity. Isotropic, kinematic, or a combination of isotropic and kinematic hardening parameters may be obtained by varying hardening parameter (β) between 0 and 1. The whole mathematical formulations of the model are given in the LS-Dyna manual [11]. The rigidity of the projectile allocates a high failure strain to the missile, which is not eroding.

Polyurea, an important component for strengthening of RC panel, is modeled using elastoplastic material code in LS Dyna. MAT Piecewise Linear Plasticity, which is used for modeling polyurea, accounts for failure criteria and strain rate effects that are incorporated using experimental data to model the hardening response for a wide range of strain rates [3]. Defining the polyurea's elastic response involves an elastic modulus of 2520 MPa and a yield stress of 10 MPa. Polyurea properties were taken from a series of high strain rate tensile and compressive tests conducted by Roland et al. [27]. To ensure accuracy, engineering stress (σ_e) and strain (ϵ_t) curves were transformed into true stress (σ_t) and strain (ϵ_e) using the equations:

$$\sigma_t = \sigma_e(1 + \epsilon_e) \quad (1)$$

$$\epsilon_t = \ln(1 + \epsilon_e) \quad (2)$$

The true stress strain plots are shown in Figure 4.

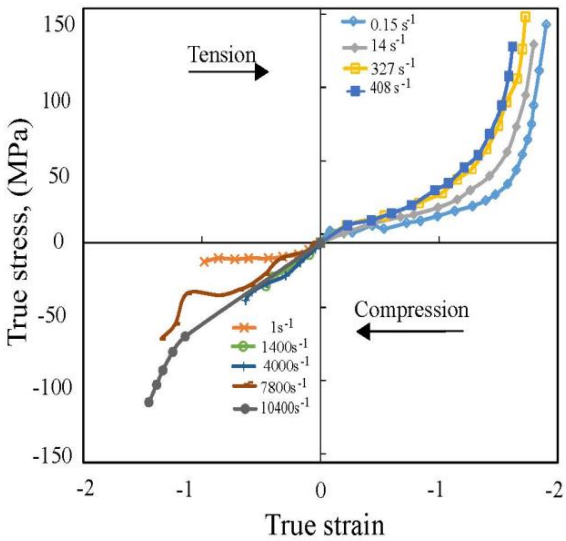

Figure 4: Stress–strain plots of Polyurea at different strain rates Roland et al.

3. VALIDATION OF THE FINITE ELEMENT MODEL

The parameters like DOP and equivalent front crater (FC) and back crater (BC) diameter for the uncoated RC panel due to projectile impact were validated with the experimental results from Kojima [20]. An RC panel of size 1 m × 1 m with varying thickness having concrete strength 27 MPa and ratio of the reinforcement as 0.6 % (longitudinal and transverse) was subjected to impact using a 2 kg rigid hemispherical projectile. The CSCM concrete model, having fewer inputs than other concrete models, effectively aligns with the test results of Kojima [20]. Its inputs encompass parameters like density, rate effects, erosion, compressive strength, and maximum aggregate size. The unconfined compression strength influences all components of the fit, including stiffness, three-dimensional yield strength, hardening, and damage. The CSCM concrete density of 2400 kg/m^3, compressive strength of 27 MPa, and maximum aggregate size of 20 mm are used in this study for validation. This model accommodates inherent strain rate effects associated with the Dynamic Increase Factor (DIF). Static compressive strength of the 27 MPa [20] was calibrated by a single element FE compression test on 150 mm × 150 mm × 150 mm, wherein compressive strength of 26 MPa was obtained. The steel reinforcement is set with a failure strain of 20 %. It is modeled as a 1D-element, utilizing the Belytschko-Schwer resultant beam element form, a choice made to decrease computational time ultimately. Firstly, the DOP of the projectile into the RC target captured by FE simulation was compared experimental study, as shown in Figure 5.

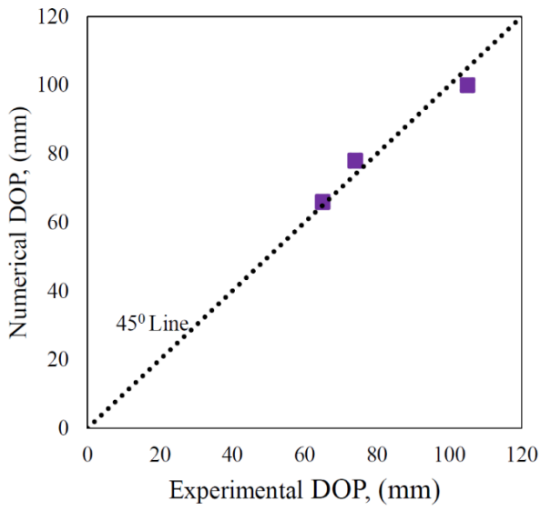

Figure 5: Numerical vs experimental [20] comparison of DOP

Reasonable agreement was observed between numerically captured DOP and experimental results of Kojima [20]. Also, the numerically obtained FC and BC sizes were compared for various cases with experimental results and are shown in Tables 1 and 2. Further, extended analyses that have been carried out are discussed in the next section.

Table 1: Comparison of numerical and experimental FC [20]

Panel thickness (mm)	Impact velocity (m/s)	Numerical FC (mm)	Experimental FC (mm)
120	215	233 × 200	205 × 226
180	211	243 × 210	282 × 217

Table 2: Comparison of numerical and experimental BC [20]

Panel thickness (mm)	Impact velocity (m/s)	Numerical BC (mm)	Experimental BC (mm)
120	164	471 × 457	561 × 480
180	211	449 × 479	445 × 435

An experimental study conducted by Rajput and Iqbal [26] was considered to strengthen the numerical model's validation. A plain concrete panel with dimensions of 450 × 450 mm × 100 mm, 2400 kg/m^3 density, designed with M40 concrete grade impacted by a 1 kg ogive-nosed hard projectile of 19 mm diameter and 450 mm length is modeled and analysed. The concrete panel's ballistic limit (V_{bl}) as established numerically. V_{bl} was found to be 98 m/s (see Table 3). Velocity was varied from 90 m/s to 105 m/s, 98 m/s was observed as the minimum velocity necessary for perforation of the panel. Hence, 98 m/s was designated as the ballistic limit, closely matching the experimental value of 107 m/s. Further, the numerical value of the ballistic limit (98 m/s) matches closely with 106 m/s given by CEA-EDF empirical formula shown in Eq. 3 as

$$V_{bl} = 1.3 \times \rho_c{}^{1/6} \times f_c^{0.5} \times \left(\frac{d_p t^2}{M_p}\right)^{2/3}, \quad (3)$$

where, ρ_c, f_c, d_p, M_p and t are the density of concrete (kg/m3), concrete compressive strength (Pascal), projectile diameter (m), projectile mass (kg) and target thickness (m), respectively.

Table 2: Numerically obtained ballistic limit for 450 mm × 450 mm×100 mm PC panel

Impact velocity (m/s)	DOP (mm)	Residual velocity (m/s)
90	88	-
95	95	-
98	-	3
105	-	140

Zhang et al [37] studied the impact response of RC beams coated with polyurea layers subjected to drop weight. This paper numerically simulates this experimental work for further validation. Firstly, the impact force of the uncoated RC beam was validated along with failure mode (see Figure. 6). Secondly, an RC beam coated with 8 mm thick polyurea was simulated and the impact force compared to the coated RC beam was validated (see Figure 7). Reduced impact force was observed in the case of an uncoated RC beam compared to a coated RC beam when subjected to a hemispherical-nosed drop wight impactor.

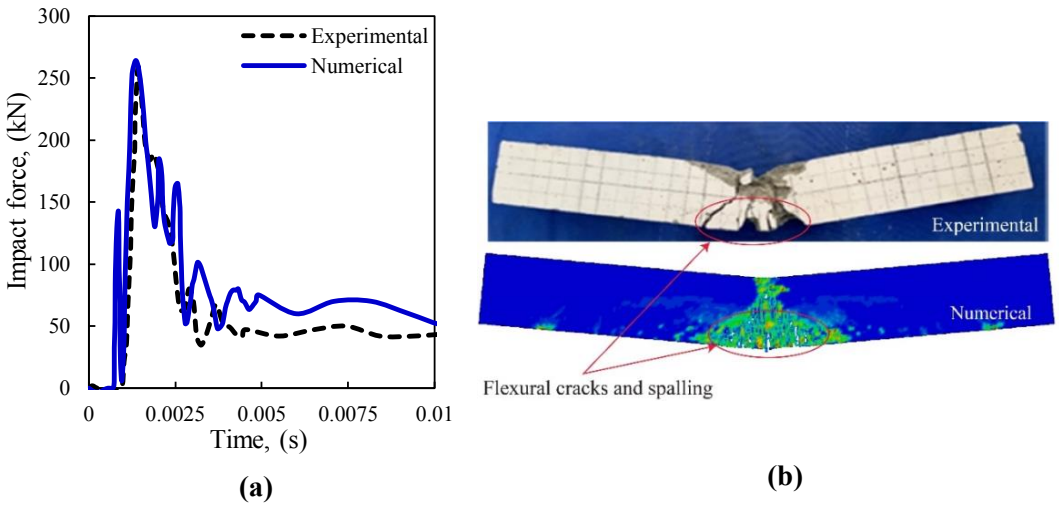

Figure 6: Numerical vs experimental [37] comparison of (a) impact force and failure mode of uncoated RC beam

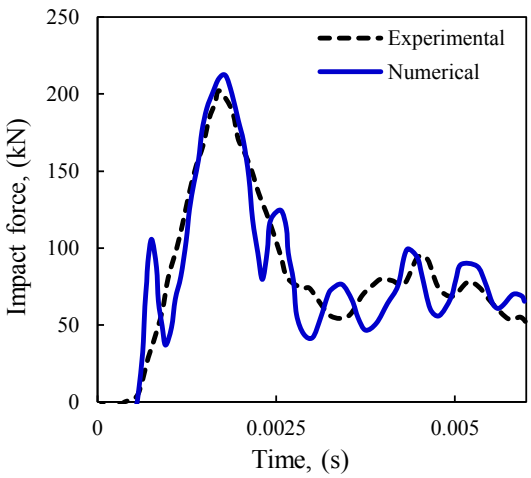

Figure 7: Numerical vs experimental [37] comparison of (a) impact force of coated RC beam

4. STRENGTHENING OF RC PANELS

After successful validation, ballistic resiliency of 1 m × 1 m × 0.12 m RC panel is evaluated when strengthened by polyurea coating. The ballistic performance of coated RC panels is compared with uncoated RC panels. The ballistic limit, i.e., the minimum projectile velocity required to perforate the uncoated target panel, is evaluated as 135 m/s and is taken as reference velocity for all panels. RC panels coated with 2 mm, 5 mm, 7 mm and 10 mm thicknesses of polyurea on the impact side were considered. Similarly, the RC panel is coated with 2 mm and 5 mm polyurea on the backside were considered.

The performance of panels was studied in terms of DOP, crater formation, and projectile deceleration. The uncoated RC panel was completely perforated and resulted in FC and BC as 90 mm × 105 mm and 180 mm ×190 mm, respectively. The hard projectile impact also resulted in a hole of size 65 mm × 65 mm. Then RC panel was strengthened by polyurea on the front/impact face and back face. Polyurea with thicknesses of 2 mm, 5 mm, 7 mm and 10 mm were applied on the front/impact face, and 2 mm and 5 mm were applied on the back face. Polyurea of thickness 2 mm and 5 m on the back side of the RC panel were found ineffective in resisting penetration of the projectile and crater damage. Increasing polyurea thickness beyond 5 mm on the back face is expected to be not a viable option in terms of cost. As shown in Table 3, it was observed that upon application of 2 mm polyurea coating on the front face, the rigid projectile is no longer able to perforate the target, and no hole is observed. DOP of 110 mm was observed for the RC panel coated. Also, FC and BC decreased as shown in Table 3 and Figure 8.

Table 3: DOP, FC, BC and hole quantification in Polyurea coated RC panels

	Polyurea thickness (mm)	DOP (mm)	FC (mm)	BC (mm)	Hole (mm)
Uncoated RC panel	0	Perforated	90 × 105	180 × 190	65 × 65
Front coated RC panel	2	110	71 × 75	130 × 144	No hole
	5	87	75 × 75	100 × 110	No hole
	7	90	90 × 90	100 × 120	No hole
	10	89	98 × 100	100 × 110	No hole
Back coated RC panel	2	Perforated	85 × 88	130 × 140	65 × 66
	5	Perforated	70 × 70	140 × 150	66 × 67
	7	Perforated	75 × 70	141 × 148	64 × 68

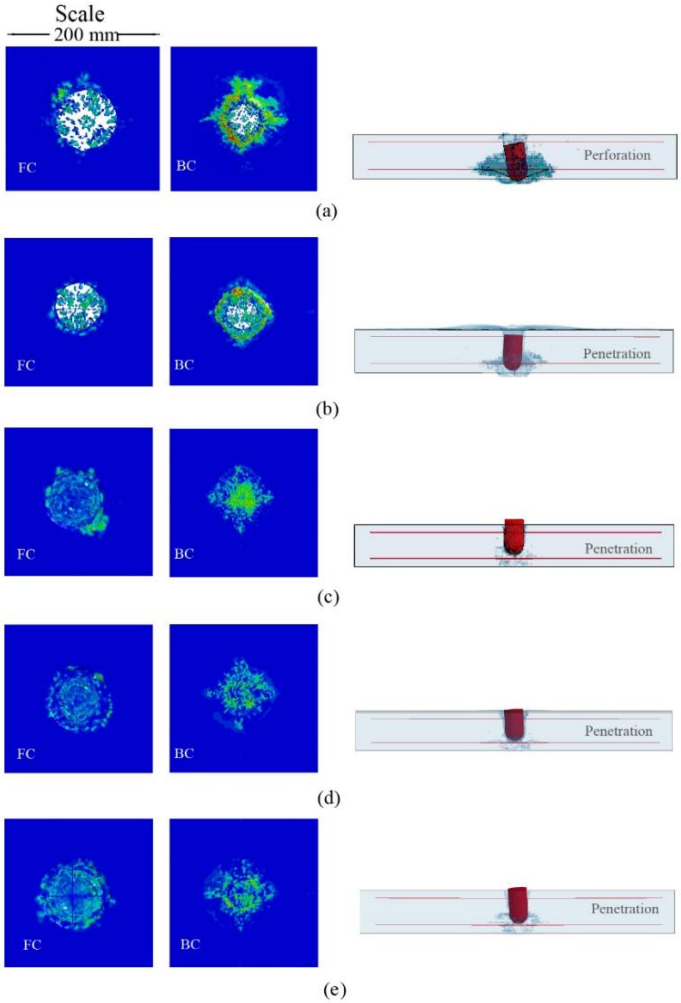

Figure 8: Crater formation and penetration in (a) Uncoated RC panel, (b) Front coated RC panel by 2 mm polyurea, (c) Front coated RC panel by 5 mm polyurea, (d) Front coated RC panel by 7 mm (e) Front coated RC panel by 10 mm polyurea.

The application of 5 mm thick polyurea further resulted in a reduced DOP of 87 mm. No further improvement in reducing FC was observed. However, BC was further decreased. Upon further increase in polyurea thickness to 7 mm and then 10 mm, no further improvement in either penetration or crater resistance was observed. With regard to blast protection enhancement of RC panel, 1-6 mm thickness of polyurea is considered optimum [33]. Also, the same can be stated for impact resistance. With the increase in polyurea thickness on the front face, projectile deceleration is enhanced by improving the penetration resistance of the RC panel (see Figure 9 (a)).

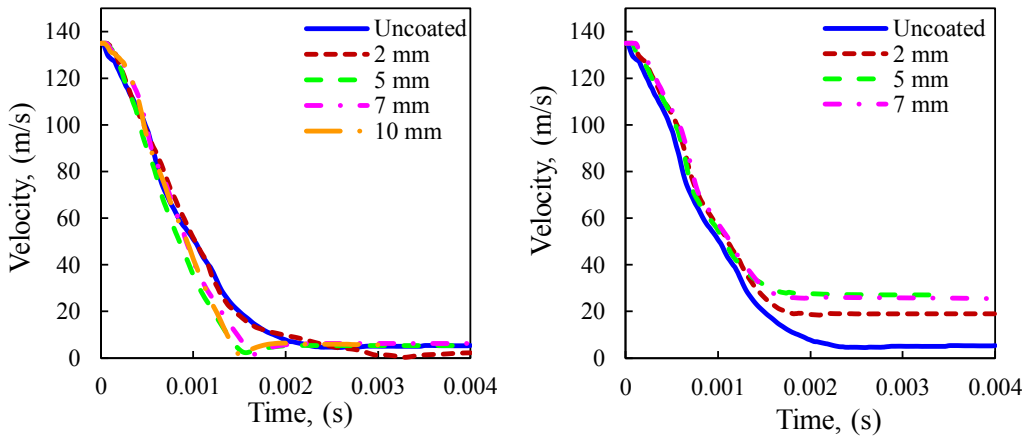

(a) Polyurea on impact face (b) Polyurea on back face

Figure 9: Deceleration of the projectile

Like the front side, polyurea was also used on the back side of the RC panel. Only a marginal increase in crater resistance was observed with no resistance to penetration (see Figure 10).

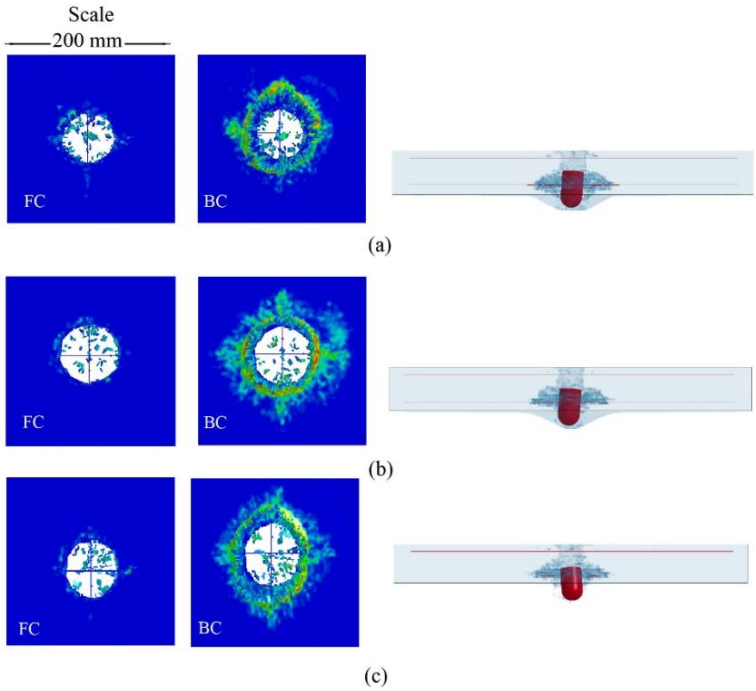

Figure 10: Crater formation and penetration in (a) Back coated RC panel by 2 mm polyurea (b) Back coated RC panel by 5 mm polyurea and (c) Back coated RC panel by 7 mm polyurea

For the 2 mm thick polyurea coating on the back side, complete perforation of the projectile through the RC panel was noticed, as in the case of the uncoated RC panel. Both FC and BC were marginally reduced. Upon the application of 5 mm polyurea coating on the back side, no penetration resistance was observed again, and the projectile perforated the target as in the case

of the uncoated RC panel. Again, FC crater resistance can be stated to have increased, and improvement in BC was marginal only. An interesting observation was made in back coated RC panel, the uncoated RC panel was perforated with an RV of 4 m/s, and hence the impact velocity was regarded as the ballistic limit of the RC panel. In the case of a 2 mm polyurea coating on the back face, a projectile RV of 19 m/s was observed. The RV observed for the 5 mm coated RC panel was 27 m/s (see Figure 9). It can be stated that an increase in polyurea coating on the back face of the RC panel might have marginally improved crater resistance; however, this resulted in a decrease in the penetration resistance of the RC panel. This could be due to the assumed full adhesion between polyurea coating and RC surface. Polyurea coating on the back side may increase the tension on the back face of the panel during impact and hence reduce penetration capacity. This phenomenon needs to be thoroughly examined. With polyurea coating on the impact face, the failure mode of the RC panel was changed from shear punching failure (as in an uncoated RC panel) to tensile failure and resulted in a transformation from local burst induced perforation to overall plastic yielding of the RC slab (see Figure 8). The front coated RC panel has higher deceleration than the back coated because of the projectile's impact energy absorption. This, in turn, influences the penetration and crater performance of the RC panel. Polyurea strengthening on the front face of the RC panel was found to have the effect of delocalising the damage. However, this effect was more pronounced in polyurea due to its high energy absorbing capacity. Some limitations of polyurea coating were reported by Zhang et al. [35], which are high demands on the spraying process, difficulty in the repair of damaged coatings, and associated high costs. In that case, other alternatives, like steel sheets or soft armor materials, can be explored to strengthen RC panels. Regarding the location, the front/impact side coating is the most effective of the RC panel protection against rigid projectile impact, unlike in the case of blast loading as reported by Lyu et al. [25], Zhang et al. [35]. Based on this analysis, a thickness of 5 mm is considered optimum for the ballistic resistance of the RC panel. The polyurea layer's contribution is progressively increased by increased polyurea thickness. It should be mentioned that the absorbed energy of the polyurea layer stays constant once the polyurea thickness exceeds 5 mm. This is in line with earlier research showing that concrete panels can be strengthened up to a certain polyurea thickness only [33]. It is therefore recommended that the effective thickness of the polyurea layer for the RC panel be between 1-5 mm, taking into account the cost and strengthening effect of polyurea.

5. CONCLUSION

This paper numerically investigates the ballistic performance of RC panels coated with polyuria when subjected to hard projectile impact. RC panel of size 1 m × 1 m × 0.12 m along with hemispherical nosed projectile are modeled and analysed numerically using LS Dyna. The validated numerical model is used to investigate the influence of polyurea coatings on the perforation characteristics of RC panels. Various thicknesses of polyurea coatings are considered on the front and back faces of the panel. The results show that the polyurea thickness on the front face, in the range of 2 to 5 mm, is a significant parameter in enhancing the ballistic limit of the RC panel. The improvements beyond 5 mm are negligible. In an uncoated RC panel

of 120 mm thickness, the projectile perforated the target however, for 2 mm and 5 mm thick polyurea coatings on the impact face, the projectile penetrated the target up to 110 mm and 87 mm, respectively. For 7 mm and 10 mm thick polyurea on the impact face, a DOP of 90 mm and 89 mm was observed. Additionally, the study reveals that applying polyurea coating on the impact face of the panel proves more effective than on its back face.

ACKNOWLEGEMENT

The authors acknowledge the financial support from the Ministry of Human Resource Development (MHRD) Government of India.

DECLARTION OF COMPETING INTERST

The authors have no competing interests to declare that are relevant to the content of this article

REFERENCES

[1] Abbas, H., Al-Dabaan, M., Siddiqui, N., Almusallam, T., Al-Salloum, Y. (2023). Performance of reinforced concrete composite wall systems under projectile impact. *Journal of Materials Research and Technology* 23, 3062–3090. doi:https://doi.org/10.1016/j.jmrt.2023.01.187.

[2] Abdel-Kader, M., Fouda, A., (2019). Improving the resistance of concrete panels to hard projectile impact. *International Journal of Protective Structures* 10, 510–538. doi:10.1177/2041419619834568.

[3] Chen, C.C.a. (2014). Numerical simulations of dynamic behavior of polyurea toughened steel plates under impact loading. *Journal of Computational Engineering* doi:https://doi.org/10.1155/2014/416049.

[4] Chen sun, Y., Wang, B., Zhang, B., Zheng, Q., nan Zhou, J., nian Jin, F., lin Fan, H. (2020). Polyurea coating for foamed concrete panel: An efficient way to resist explosion. *Defence Technology* 16, 136–149. doi:https://doi.org/10.1016/j.dt.2019.06.010.

[5] Dapper, P.R., Ehrendring, H.Z., Pacheco, F., Christ, R., Menegussi, G.C., Oliveira, M.F.d., Tutikian, B.F. (2021). Ballistic impact resistance of uhpc plates made with hybrid fibers and low binder content. *Sustainability* doi:10.3390/su132313410.

[6] Dar, R.U.N., Anas, S.M., Alam, M. (2022) Effect of skew angle on the dynamic response of a reinforced concrete bridge under blast loading. *ASPS Conference Proceedings*, 555–561 https://doi.org/10.38208/acp.v1.548

[7] Dar, R.U.N., Alagappan, P. (2023). Response of Reinforced Concrete Bridge Subjected to Blast Loading. In: Marano, G.C., Rahul, A.V., Antony, J., Unni Kartha, G., Kavitha, P.E., Preethi, M. (eds) *Proceedings of SECON'22. SECON 2022. Lecture Notes in Civil Engineering*, vol 284. Springer, Cham. https://doi.org/10.1007/978-3-031-12011-4_75

[8] Dar, R.U.N., Alam, M. (2021). Damage Evaluation of Reinforced Concrete Bridge Subjected to Blast Loading. In: Chandrasekaran, S., Kumar, S., Madhuri, S. (eds) *Recent Advances in Structural Engineering. Lecture Notes in Civil Engineering*, vol 135. Springer, Singapore. https://doi.org/10.1007/978-981-33-6389-2_14

[9] Fang, C., Linzell, D.G., Yosef, T.Y., Rasmussen, J.D. (2022). Numerical modeling and performance assessment of bridge column strengthened by frp and polyurea under combined collision and blast loading. *Journal of Composites for Construction* 26, 04022002. doi:10.1061/(ASCE)CC.1943-5614.0001188.

[10] Feng, J., Sun, W., Wang, L., Chen, L., Xue, S., Li, W. (2020). Terminal ballistic and static impactive loading on thick concrete target. *Construction and Building Materials* 251, 118899. doi:10.1016/j.conbuildmat.2020.118899.

[11] FHWA-HRT-05-062, 2001a. LS-DYNA keyword user's manual, VOLUME II Material Models, References and Appendices.

[12] FHWA-HRT-05-062, 2007b. Users Manual for LS-DYNA Concrete Material Model 159.

[13] Gangolu, J., Kumar, A., Bhuyan, K., Sharma, H. (2022). Performanc ebased probabilistic capacity models for reinforced concrete and prestressed concrete protective structures subjected to missile impact. *International Journal of Impact Engineering* 164, 104207. doi:10.1016/j.
ijimpeng.2022.104207.

[14] Huang, R., Wen, Y., Li, Y., Zhou, H., Yang, X., Qin, J., Chi, H., Lai, Z. (2024). Application of concrete damage evolution equation considering confining pressure and strain rate effects in projectile penetration. *Engineering Failure Analysis* 107916doi:https://doi.org/10.1016/ j.engfailanal.2023.107916.

[15] Iqbal, M., Rajput, A., Bhargava, P. (2017). Plain and reinforced concrete targets subjected to projectile impact. *Procedia Engineering* 173, 138–144. doi:10.1016/j.proeng.2016.12.050.

[16] Iqbal, N., Sharma, P., Kumar, D., Roy, P. (2018). Protective polyuria coatings for enhanced blast survivability of concrete. *Construction and Building Materials* 175, 682–690. doi:https://doi.org/10.1016/j.conbuildmat.2018.04.204.

[17] Ji, L., Wang, P., Cai, Y., Shang, W., Zu, X. (2022). Blast resistance of 240 mm building wall coated with polyurea elastomer. *Materials* 15. doi:https://www.mdpi.com/1996-1944/15/3/850.

[18] Jiang, Y., Zhang, B., Wei, J., Wang, W. (2020). Study on the dynamic response of polyurea coated steel tank subjected to blast loadings. *Journal of Loss Prevention in the Process Industries* 67, 104234. doi:https://doi.org/10.1016/j.jlp.2020.104234.

[19] Khan, S.H., Agnihotri, S.K., Khan, A.A., Husain, A. (2020). Finite element modeling and simulation of projectile impact on ductile target, in: *Recent Advances in Mechanical Engineering, Springer Singapore*. pp. 429–437.

[20] Kojima, I. (1991). An experimental study on local behavior of reinforced concrete slabs to missile impact. *Nuclear Engineering and Design* 130, 121–132. doi:10.1016/0029-5493(91)90121-W.

[21] Kumaran, S., Lim, C., Ong, K., Tan, G. (2000). Effects of different nose-shaped projectiles on the high speed perforation of concrete, *AIP Conference Proceedings*, Volume 505, pp. 1233-1236 (2000). doi:10.1063/1.1303684.

[22] Li, X., Liu, Y., Yan, J., Shi, Z., Wang, H., Xu, Y., Huang, F. (2023). High-speed penetration of ogive-nose projectiles into thick concrete targets: Tests and a projectile nose evolution model. *Defence Technology,* doi:https://doi.org/10.1016/j.dt.2023.03.010.

[23] Li, Y., Chen, Z., Zhao, T., Cao, X., Jiang, Y., Xiao, D., Fang, D. (2019). An experimental study on dynamic response of polyurea coated metal plates under intense underwater impulsive loading. *International Journal of Impact Engineering* 133, 103361. doi:https://doi.org/10.1016/j.ijimpeng.2019.103361.

[24] Livermore. California: Livermore Software Technology Corporation (2006). LS-DYNA. Keyword User's Manual.

[25] Lyu, P., Fang, Z., Wang, X., Huang, W., Zhang, R., Sang, Y., Sun, P. (2022). Explosion test and numerical simulation of coated reinforced concrete slab based on blast mitigation polyurea coating performance. *Materials* 15. URL: https://www.mdpi.com/1996-1944/15/7/2607.

[26] Rajput, A., Iqbal, M., 2017. Ballistic performance of plain, reinforced and pre-stressed concrete slabs under normal impact by an ogival-nosed projectile. *International Journal of Impact Engineering* 110, 57–71.doi:10.1016/j.ijimpeng.2017.03.008.

[27] Roland, C., Twigg, J., Vu, Y., Mott, P. (2007). High strain rate mechanical behavior of polyurea. *Polymer* 48, 574–578. doi:https://doi.org/10.1016/j.polymer.2006.11.051.

[28] Song, D., Tan, Q., Zhan, H., Liu, F., Jiang, Z. (2019). Experimental investigation on the cellular steel-tube-confined concrete targets against projectile impact. *International Journal of Impact Engineering* 131, 94– 110. doi:10.1016/j.ijimpeng.2019.05.004.

[29] Sonoda, Y., Tamai, H., Ifuku, T., Koshiishi, M. (2022). Reinforcing effect of polyurea resin coating on rc members subject to low-speed and medium-speed impact. *Advances in Structural Engineering* 25, 1609– 1621. doi:10.1177/13694332221088945.

[30] Sovj´ak, R., Vav˘rin´ık, T., Zatloukal, J., M´aca, P., Mi˘cunek, T., Frydr´yn, M. (2015). Resistance of slim uhpfrc targets to projectile impact using in-service bullets. *International Journal of Impact Engineering* 76, 166–177. doi:10.1016/j.ijimpeng.2014.10.002.

[31] Sundaram, S., G., B., B., A. (2020). Influence of target dynamics and number of impacts on ballistic performance of 6061-t6 and 7075-t6 aluminum alloy targets. *Mechanics Based Design of Structures and Machines*50, 1–20. doi:10.1080/15397734.2020.1738245.

[32] Wu, G., Wang, X., Ji, C., Gao, Z., Jiang, T., Zhao, C., Liu, Y. (2021). Anti-blast properties of 6063-t5 aluminum alloy circular tubes coated with polyurea elastomer: Experiments and

numerical simulations. *Thin-Walled Structures* 164, 107842. doi:https://doi.org/10.1016/j.tws.2021.107842.

[33] Wu, J., Liu, Z., Yu, J., Xu, S. (2022). Experimental and numerical investigation of normal reinforced concrete panel strengthened with polyuria under near-field explosion. *Journal of Building Engineering* 46, 103763. doi:https://doi.org/10.1016/j.jobe.2021.103763.

[34] Zhang, B., Jiang, Y., Wang, W., Zhai, D. (2023). Impact response of rc beams coated with polyurea layers. *International Journal of Structural Stability and Dynamics* 23, 2330002. doi:10.1142/S0219455423300021.

[35] Zhang, R., Huang, W., Lyu, P., Yan, S.,Wang, X., Ju, J. (2022). Polyurea for blast and impact protection: A review. *Polymers* (Basel) 14. doi:10.3390/polym14132670.

[36] Zhou, F., Wu, H., Cheng, Y. (2023). Perforation studies of concrete panel under high velocity projectile impact based on an improved dynamic constitutive model. *Defence Technology* 27, 64–82. doi:https://doi.org/10.1016/j.dt.2022.09.004.

[37] Zhang, B., Jiang, Y., Wang, W., Zhai, D. Impact response of rc beams coated with polyurea layers, International Journal of Structural Stability and Dynamics 23 (2023) 2330002. doi:10.1142/S0219455423300021.

EXPLOSION ANALYSIS ON PROTECTION WALL OF HYDROGEN STORAGE TANK WITH TNT EQUIVALENT WEIGHT METHOD

Topendra Oli[1], Abidemi Bashiru Folorunsho [1], Gihyun Kim[1], Taejin Jang[1], Cheolwoo Park[1], and Seungwon Kim[1]

[1] Department of Civil Engineering, Kangwon National University, marvin.topu@gmail.com.

Corresponding Author: Seungwon Kim.

346 Jungang-ro, Samcheok-Si, Gangwon-do, Republic of Korea, 25913

Email: seungwon.kim@kangwon.ac.kr

ABSTRACT

The daily increase in hydrogen gas storage facilities reflects the growing demand and recognition of hydrogen as a promising fuel for the future, bringing numerous social, economic, and environmental advantages. Despite its potential benefits, the accidental explosions of hydrogen storage tanks have posed significant challenges, impacting the economy, infrastructure, and living conditions. This study used an 8 kg trinitrotoluene (TNT) explosion test between reinforced concrete walls for a 25 kg hydrogen gas explosion through the TNT equivalent weight method. The dimensions of the reinforced concrete wall were 2 m in height, 5 m in length, and 0.2 m and 0.25 m in width. In addition, the experimental pressure was compared with the TNT explosion simulation results. LS-DYNA, a commercial software, was used to study the TNT explosion near a reinforced concrete protection wall through simulation. The experimental and simulation pressure curves had a good agreement. For further simulation analysis, the TNT equivalent weight method was studied for hydrogen gas, and the behavior of the protection wall under explosion was analyzed. From experimental and simulation results, it was confirmed that pressure decreases when the upward flow of blast load increases at the time of near-field denotation. Numerical simulation concludes that increasing the thickness of the protection wall decreases the displacement on the protection wall.

Keywords: *Hydrogen Gas Explosion, Reinforced Concrete, Protection Wall, TNT Equivalent Weight Method, Trinitrotoluene Explosion, Accidental Explosion.*

1. INTRODUCTION

The global community has been faced with an energy crisis in recent times due to the depletion of resources and rising environmental problems [1]. In the global market, hydrogen gas has a crucial role as an energy carrier and is one of the most promising clean fuel options. Given the possibility of almost unlimited renewable production, its impact on sustainable development would be significant. The key factors affecting future hydrogen markets are the price of hydrogen, technical progress, competition costs for energy systems, and potential longer-term restrictions on greenhouse gas emissions. Hydrogen has been envisaged as a future dream fuel,

providing many benefits for society and the environment. With South Korea focusing on the hydrogen economy for economic growth and industrial competitiveness rather than solely on climate change goals, its consumption is increasing worldwide. South Korea considers hydrogen an economic growth driver of around $43 billion, creating 420,000 new jobs. Hydrogen gas accidents pose risks, with explosions causing infrastructure damage and harm to living beings, despite its benefits. Handling hydrogen requires caution due to its flammability, with frequent explosion incidents globally. Notable accidents include those in Gangwon, South Korea (2019), Santa Clara, CA (2019), and Texas City (2020). Ensuring high-scale hydrogen production and distribution infrastructure safety in cities is essential to implementing rigorous standards and best practices [2].

The experimental detonation of TNT between the different thicknesses of reinforced concrete barrier walls was carried out in this study. An experiment of 25 kg hydrogen gas explosion was used to calculate the TNT equivalent weight, and the TNT weight was 8 kg. This study compared the experimental and simulation pressure results under the TNT explosion at a 2 m distance from TNT. Furthermore, the blast experiment is expensive to conduct many times, so, during the experiment, two barrier walls with thicknesses of 0.2 m and 0.25 m were conducted at a time. So, in this study, the barrier walls with 0.2 m and 0.25 m thicknesses were simulated separately under the explosion of 25 kg of hydrogen gas cylinder through TNT equivalent weight method and using LS-DYNA. The pressure was analyzed, simulating the different thicknesses of reinforced concrete barrier walls. In addition, the effect of rebar diameter and compressive strength of concrete under the blast load was analyzed.

2. TNT EQUIVALENT WEIGHT METHOD

Estimating the TNT equivalent method is a common approach for determining damages caused by hydrogen explosions. The equivalent weight of TNT can be calculated with equation 1 in a vapor cloud explosion. As hydrocarbons, relatively weak explosives are the most common substance involved in the vapor cloud explosion, and only a tiny part of the energy released is used to create the explosion wave; different authors have proposed values between 1% and 10%. However, the value of explosion efficiency (η) is probably influenced by the fuel's reactivity and the cloud's eventual partial confinement. The main characteristics of the explosions of TNT and vapor clouds are different; TNT is a high-energy density explosive, and vapor clouds are a low-energy-density source. The explosion of TNT is a detonation, whereas the explosion of the vapor cloud is a deflagration, i.e., the shape and velocity of its respective explosion waves are different. In addition, it is necessary to consider that uncertainties concerning the size, shape, and composition of the vapor cloud and their influence on confinement and congestion in areas covered by a flammable mixture will give rise to errors if another alternative method is used. Therefore, as the TNT equivalency method is straightforward, it remains widely used [3,4]. Exploding can occur in the present 4% to 75% hydrogen ratio with air [4,5]. A 25% volume of hydrogen with air has been used in this study. The equivalent mass of TNT is about 8 kg, according to expression 1.

$$M_{TNT} = \eta M_{H_2} \frac{Q_{H_2}}{Q_{TNT}} \quad (1)$$

where,

M_{H2} is the mass of the hydrogen gas = 25 kg

Q_{H2} is Explosion energy of Hydrogen gas = 142.5 MJ/kg

Q_{TNT} is explosive energy of TNT = 4.6 MJ/kg

η is Explosion efficiency for this 0.042 was taken.

3. EXPERIMENT METHOD

The 8 kg of TNT was placed at a standoff distance of 1 m between a reinforced concrete barrier wall of 0.2 m and 0.25 m thickness. The center-to-center distance of the rebar was 0.25 m, and the clear cover was 0.02 m. The TNT equivalent weight of 25 kg hydrogen gas cylinder explosion was considered 8 kg. The position of the pressure gauge was at a distance of 2 m from the TNT. The pressure gauge was placed 0.92 m above the ground level. Pressure at a distance of 2 m was measured in the experiment. The position of the TNT was 0.92 m above ground level. The compressive strength of the concrete from the experiment was 21 MPa. A 0.01 m diameter of the rebar was used to reinforce the barrier wall. Figure 1 shows the outline of the experimental setup.

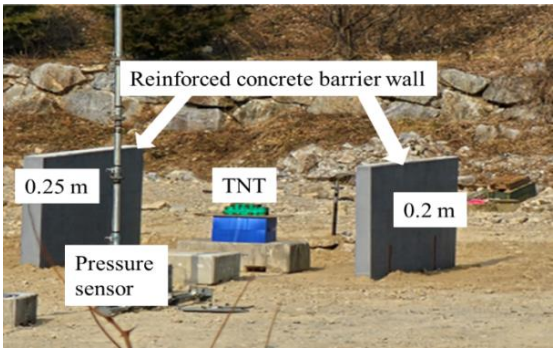

Figure 1. Experimental blast test setup.

4. SIMULATION METHOD

The commercial software LS-DYNA was used to do simulation work. The model was modeled as in the experiment, and the position of the TNT and the pressure gauge was the same as in the experiment. Figure 2 shows the simulation model. The material model was taken from the material library of LS-DYNA. In this paper, the MAT_72R3, MAT_PLASTIC_KINEMATIC. *NULL material, *MAT_HIGH_EXPLOSIVE_BURN, and *MAT_SOIL_MATERIAL_MODEL_147 models were used for concrete, rebar, air, TNT, and soil, respectively.

LS-DYNA material library has different material models for concrete. Among concrete constitutive models introduced in LS-DYNA, the K&C and CSCM models are plastic-based damage models developed based on plain concrete. In this paper, the MAT_72R3 model allows parameters to be automatically generated based on the unconfined compressive strength as the only input parameter. The automatically generated parameters reflect the behavior of a regular concrete material under blast load and thus are employed in the finite element (FE) models. The compressive strength of the concrete from the experiment was 21 MPa and was used to validate the simulation. The compressive strength of the concrete was set to 28 MPa for additional simulations. Similarly, the density of 7850 kg/m^3, 1.293 kg/m^3, and 1630 kg/m^3 were used for rebar, air, and TNT, respectively. The equation of state (EOS) assigned for air and explosive were LINEAR_POLYNOMIAL and JONES_WILKINS_LEE (JWL), respectively. The finite element mesh size for this study's concrete structural part and TNT was 0.02 m, whereas the mesh size for the air was 0.05 m for length and height and 0.08 m for breadth. Figure 2 shows the model for the simulation.

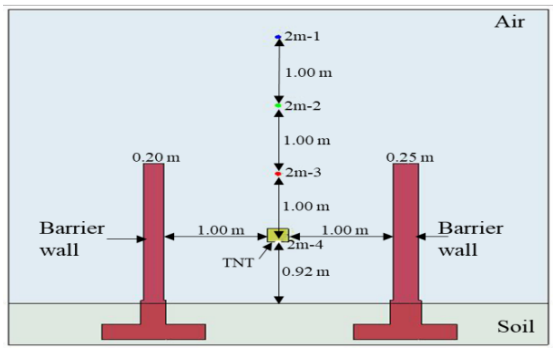

Figure 2. Simulation model with dimension.

The bottom side of the foundation of the reinforced concrete barrier wall was fixed. Among 6 sides 5 sides of the air had a non-reflective boundary condition expect bottom. *CONSTRAINED_LANGRANGE_IN_SOLID was used for coupling between Arbitrary-Lagrangian-Eulerian (ALE) and Lagrangian. Similarly, *CONSTRAINED_LANGRANGE_IN_SOLID was used between rebar and concrete structure for coupling. The detonation point of the TNT was at the center of the TNT. The Arbitrary-Lagrangian-Eulerian (ALE) method was used, a straightforward modeling strategy for shock wave propagation. The explosive and the air are separately modeled using the ALE formulation with a multi-material option. Appropriate Equations of State (EOS) were assigned to the materials (air and TNT). The shock wave travels through the ALE air domain and impinges the target structure. The termination time for the simulation was ten milliseconds.

5. RESULTS AND DISCUSSION

5.1. Validation of Simulation

Figure 3 represents the pressure-time curve between the structures from the simulation at a distance of 2 m from the TNT explosion. The position and symbol of the pressure gauge are shown in Figure 2. 2m-1, 2m-2, 2m-3 and 2m-4 are the pressure sensors used for the numerical

simulation and at 2 m from the TNT between the structures. 2m-1, 2m-2, 2m-3 and 2m-4 are at the height of 0.92 m, 1.92 m, 2.92 m and 3.92 m respectively, from the ground level. The experiment found that the pressure at 0.92 m from the ground level at a 2 m distance from TNT was 717.2 kPa, and from the simulation, the pressure was 712 kPa for the same position. In addition, this study analyzed the different pressures from the simulation. It was found that the pressure decreases when the upward flow of blast load increases at the time of near-field denotation. According to the American Society of Civil Engineers, blast loads with a scaled distance of less than 1.2 m/kg$^{1/3}$ are identified as close in detonations [6]. It was confirmed that the equivalent pressure was non-uniformly distributed under a near-field detonation.

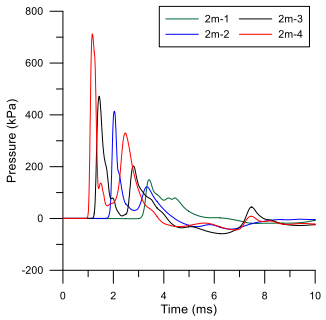

Figure 3. Pressure versus time curve at different heights.

5.2. Displacement on Barrier Wall

Figure 4 shows the position of the displacement probe and displacement results after the explosion of 25 kg of hydrogen gas cylinder. Displacement from the simulation was taken from the element selection at the position as in Figure 4 (a). Figure 4 (b) shows that the shortest distance from the explosion gets more displacement than others. In Figure 4(b), high displacement was observed at the center for both thicknesses of the barrier wall. The thickness of the barrier wall plays a vital role in decreasing the displacement under the explosion loads.

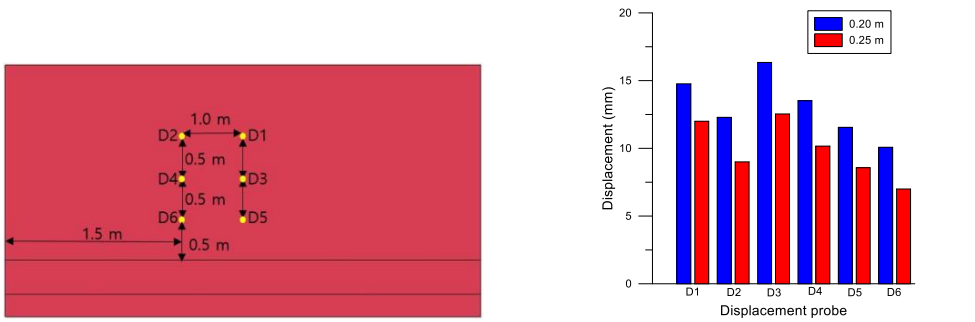

(a) Position of displacement probe (b) Displacement from simulation results

Figure 4. The position of the displacement probe and displacement results.

5.3. Pressure under the Explosion of 25 kg Hydrogen gas

The blast experiment is expensive to conduct many times, so during the experiment, two barrier walls with thicknesses of 0.2 m and 0.25 m were conducted at a time. So, in this simulation section, the two models with 0.2 m and 0.25 m thicknesses were simulated separately under

the explosion of 25 kg of hydrogen gas cylinder through the TNT equivalent weight method and analyzed the pressure. Figure 5 shows the pressure-time curve after the blast with different thicknesses of 0.2 m and 0.25 m. It was observed that the blast pressure was less with the barrier thickness of 0.25 m compared with the 0.2 m. The pressure at the height of 3.92 m (2m-1) was observed to be the same for both cases. In addition, Figure 5 confirmed that the equivalent pressure was non-uniformly distributed under a near-field detonation.

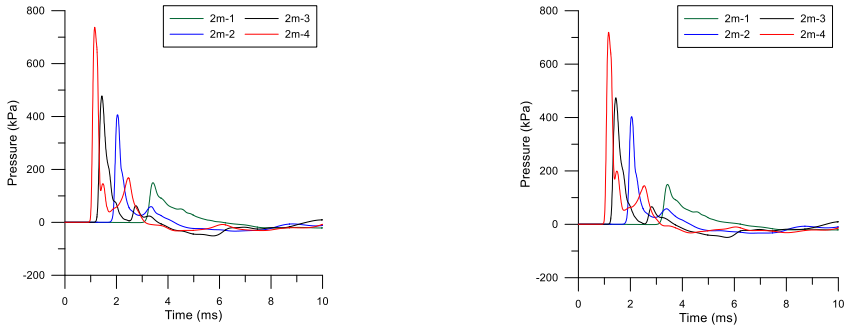

(a) Pressure versus time plot at a thickness of 0.2 m

(b) Pressure versus time plot at a thickness of 0.25 m

Figure 5. Pressure versus time curve with different thicknesses of barrier wall.

5.4. Effect of Rebar Diameter and Compressive Strength of Concrete

In this study section, the thickness of the barrier wall was taken as 0.2 m to run the simulation. According to the UFC 3-340-02 concrete strength, it should be 28 MPa or higher strength concrete to design a barrier wall for blast load [7]. In this experiment, the strength of the concrete was 21 MPa, and the diameter of the rebar was 0.01 m. This section compares the effect of rebar diameter and compressive strength of the concrete to compare the displacement on the barrier wall under the explosion of 25 kg of hydrogen gas. The rebar diameter was taken as 0.01 m and 0.016 m [2], whereas the compressive strength of 21 MPa and 28 MPa. From the simulation displacement results of the barrier wall under the explosion of 25 kg of hydrogen gas, it was observed that the use of 0.016 m of rebar reduces the displacement on the barrier wall compared with 0.010 m of rebar diameter. Similarly, using 28 MPa concrete compressive strength for the barrier wall reduced the displacement compared to 21 MPa.

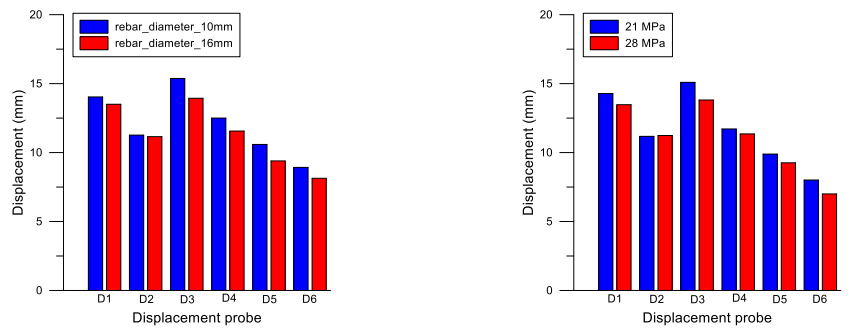

(a) Effect of rebar

(b) Displacement from simulation results

Figure 6. Displacement results in different diameters of rebar and compressive strength of concrete.

6. CONCLUSION

The pressure under the hydrogen gas tank explosion was studied through experiment and simulation. The TNT equivalent weight method was used to calculate the TNT weight of hydrogen gas. Notably, the experimental pressure results after the explosion demonstrated a good agreement with the simulation at a distance of 2 m from the TNT position. In addition, the effect of rebar diameter and compressive strength of concrete had been studied through simulations. Following are the key conclusions drawn from this study.

1. According to the simulation results, the pressure decreases when the blast load's upward flow increases during near-field denotation. It was confirmed that the equivalent pressure was non-uniformly distributed under a near-field detonation.
2. When the blast pressure was analyzed with the different thicknesses of the barrier wall, the blast pressure was reduced from 737 kPa to 719 kPa at 0.2 m and 0.25 m thickness, respectively. It was concluded that the near-field blast pressure decreases with an increase in the thickness of the barrier wall.
3. The effect on the barrier wall area was directly proportional to the shortest distance from the explosion. In this study, the simulation results show that the center displacement was higher than in the other areas of the barrier wall.
4. Increasing the rebar's diameter and the concrete's compressive strength reduces the barrier wall's displacement under explosion.

ACKNOWLEDGMENTS

This research was supported by the Korea Institute of Energy Technology Evaluation and Planning (KETEP) and the Ministry of Trade, Industry & Energy (MOTIE) of the Republic of Korea (No. 20215810100020).

REFERENCES

[1] Balat, M. (2008). Potential importance of hydrogen as a future solution to environmental and transportation problems. *International Journal of Hydrogen Energy*, 33(15), 4013–4029.

[2] Kim, S., Jang, T., Oli, T., & Park, C. (2023). Behavior of Barrier Wall under Hydrogen Storage Tank Explosion with Simulation and TNT Equivalent Weight Method. *Applied Sciences* (Switzerland), 13(6).

[3] Casal, J. (2017). Evaluation of the effects and consequences of major accidents in industrial plants. Elsevier.

[4] Kwon, S., & Park, J. (2015). A Review of TNT Equivalent Method for Evaluating Explosion Energy due to Gas Explosion. *Korea Society for Explosives and Blasting Engineering*, 33(3), 1–13.

[5] López, E., Rengel, R., Mair, G. W., & Isorna, F. (2015). Analysis of high-pressure hydrogen and natural gas cylinders explosions through TNT equivalent method. *V Iberian Symposium on Hydrogen, Fuel Cells and Advanced Batteries (HYCELTEC)*, July.

[6] Zhang, C., Gholipour, G., & Mousavi, A. A. (2020). Blast loads induced responses of RC structural members: State-of-the-art review. *Composites Part B: Engineering*, 195, 108066.

[7] U.S. Department of Army Unified Facilities Criteria (UFC). (2008). Structures to resist the effects of accidental explosions. In Washington, DC, USA (UFC 3-340-02).

RESISTANCE OF COMPOSITE BEAM WITH VARIOUS TYPES OF CONNECTIONS UNDER MIDSPAN IMPACT SCENARIOS

Wenbing Han[1], Kang Chen[2], Daming Wang[1], and Bo Yang[1]

[1] School of Civil Engineering, Chongqing University, Chongqing 400045, China.

[2] Department of Civil Engineering, Xi'an Jiaotong-Liverpool University, Suzhou 215123, China.

Corresponding Author: Kang Chen, PhD.

EB552 (SIP Campus-Engineering Building (EB)) Suzhou Dushu Lake Science and Education Innovation District

Suzhou Industrial Park, Suzhou 215123, P.R. China

Email: kang.chen@xjtlu.edu.cn

ABSTRACT

The buildings may encounter unexpected events such as explosions and impacts, leading to the initial failure of some structural elements, and eventually leading to progressive collapse. The falling-debris-impact scenario is one of the triggers for the progressive collapse of building structures. Therefore, this paper investigated the impact behaviour of three half-scale composite beam subassemblies with different types of connections under the falling-debris-impact scenarios by conducting both experimental tests and finite element analyses. To resist the impact load, structures must exhibit favourable flexural resistance and deformation capacity. The influence of the thickness of concrete in the composite slab, the thickness of profiled steel plate, and the ratio of longitudinal reinforcement on the impact load resistance of the structure are discussed. Parametric analysis indicated that the composite plate can significantly improve the energy absorption capacity. With the increase of the aforementioned parameters, the impact load resistance performance of the structure was significantly improved. The impact resistance of welded unreinforced flange-bolted web (WUF-B) specimens was significantly affected by the thickness of the concrete and the thickness of the profiled steel plate, whereas the ratio of longitudinal reinforcement was the critical factor for the impact resistance of fin plate (FP) and reverse channel connection (RCC) specimens. As the span-to-depth ratio increases, the failure displacement increased while the energy absorption capacity and maximum structural resistance decreased.

Keywords: *Progressive Collapse, Planar Composite Frames, Impact Tests, Numerical Simulations, Energy Absorption.*

1. INTRODUCTION

The structure within the service life is likely to encounter accidental loads, such as explosion and impact, which can cause severe initial damage to the key structural elements. This initial damage can set off a chain reaction that can lead to extensive damage and progressive collapse, resulting in significant loss of life and property [1]. Many reasons lead to the expansion of the scope of structural failure, and the falling-debris-impact scenario is one of them [2]. Falling-debris-impact refers to the initial failure of a structure after it encounters an extreme accidental load, and the structure collapses downward and impacts the remaining structure below [3,4]. In recent years, the accidents caused by the falling-debris-impact have occurred constantly (in the Ronan Point apartment collapse in London, the World Trade Center collapse in New York and the recent apartment collapse in Florida). Therefore, it is necessary to study the resistance of the structure under the impact of falling-debris.

The composite structure has many advantages, and it has been widely used in various types of practical engineering [5]. A large number of researchers have carried out experimental research and numerical analysis on the impact performance of composite structures and achieved a lot of results. The impact test and finite element analysis of steel-framed substructures with five types of beam-column connections under falling-debris impact were carried out by Wang et al. [6]. The results showed that the failure modes of specimens showed flexural and tensile modes under mid-span impact and shear modes under beam-end impact. The rigid connection may have better impact resistance when the composite slab was added in a bare steel frame [7]. The experimental and numerical analysis of welded beam-column joints subjected to falling-debris-impact revealed that composite slabs played a key role in the joint impact resistance (Yang et al. [8], Chen et al. [9], Lin et al. [10], and Wang et al. [11,12]). A design method to predict the behavior of progressive collapse for structures subjected to failed-floor impact was proposed by Vlassis et al. [13]. Huo et al. [14] carried out a series of experimental tests to investigate the dynamic behavior of steel beams subjected to free-fall impact.

Currently, there is a lack of research on the impact behavior of composite framed specimens. This study intends to address this gap by conducting impact tests and finite element (FE) analyses on composite framed specimens with different types of connections. The effect of several parameters (i.e., slab type, compressive strength of concrete, slab thickness, profiled steel plate thickness, reinforcement ratio, shear stud distance, and span-to-depth ratio) on the impact resistance was discussed. The load-resisting mechanisms were analyzed. The contribution of structural resistance [15,16] (i.e., flexural action (FA), compression arch action (CAA), and catenary action (CA)) on resisting the impact force of composite frame members was also evaluated.

2. EXPERIMENTAL INVESTIGATION

2.1. Specimen design and preparation

In order to study the dynamic response of composite structures with different connections under the falling-debris-impact scenario, a large impact loading testing machine was used to carry out the impact tests at the mid-span position on three 1/2-scale composite frame substructure

specimens. The beam-column connection types are welded unreinforced flange and bolted web (WUF-B), fin plate (FP), and reverse channel connection (RCC), which represent three different types of connections: rigid, pin, and semi-rigid connections. Meanwhile, the stiffeners were welded on the steel beam to prevent excessive local deformation at the impact position of the specimen. Figure 1 shows the schematic diagram of the composite structure specimen WUF-B as an example.

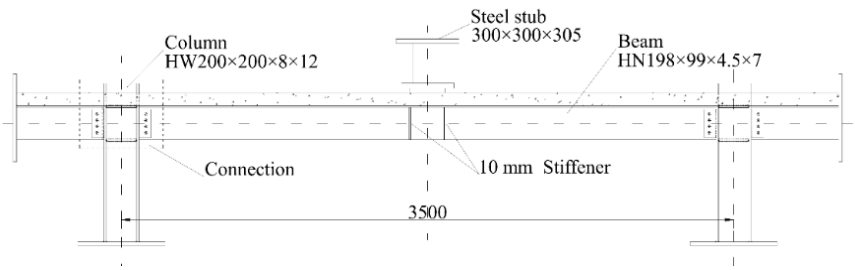

Figure 1. Details of composite structure specimen (unit: mm) [8]

Figure 2 shows the detailed size of the connections. The steel beams, steel columns, end plates, and fine plates were all made of Grade Q345 steel, while the channel and profiled steel plates were made of Q235. The high-strength bolts (Grade 12.9 M16) were used in specimen RCC. For specimens WUF-B and FP, Grade 8.8 M10 high-strength bolts were used. The measured compressive strength of the concrete cube is 47.0 MPa.

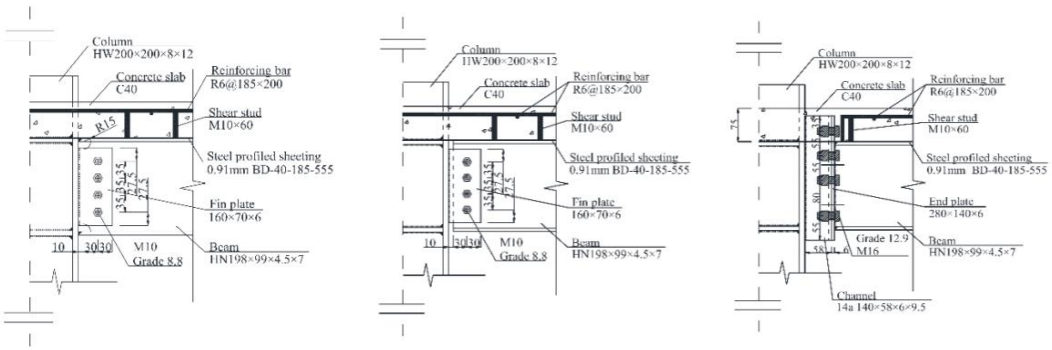

(a) WUF-B (b) FP (c) RCC

Figure 2. Details of connections (unit: mm) [8]

2.2. Impact experimental test

The single-layer single-span plane composite frame substructure was selected from the prototype structure. The dynamic response process and load resistance mechanism under impact load were studied. In order to simulate the constraint of the prototype structure on the specimens, the hinged supports were set at the position of the reverse bending point of the column and the position of 1/4 span of the adjacent span. The test setup is shown in Figure 3.

Two A-frames can be used to provide horizontal constraints on the beam end of the specimen during testing. The testing machine mainly includes a drop hammer, guide rails, a lifting system, and a data acquisition system. The drop hammer was composed of a hammerhead, a force sensor, a hammer body, and counterweight blocks. The weight of the drop hammer is 600 kg. By adding a counterweight block, the maximum mass of the drop hammer can reach 1000 kg. During the test, the drop weight was lifted to the specified height through the lifting system, and then released. The drop weight will freely fall along the guide rails under the action of gravity and contact with the test specimens, to impose the impact loading of the specimens.

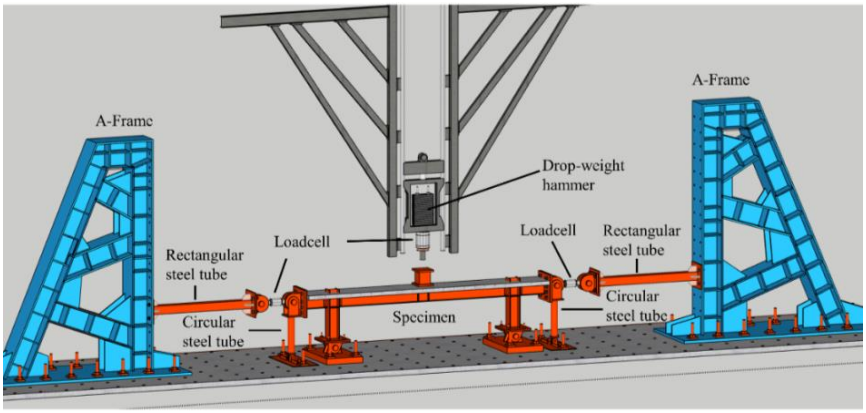

Figure 3. Test setup [8]

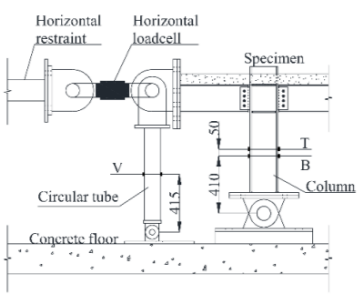

(a) Front view [8]

(b) Cross-section of a column

(c) Cross-section of a tube

Figure 4. The layout of strain gages (unit: mm)

To obtain the dynamic response process and load resistance mechanism of the specimen under the impact load, it is necessary to obtain the impact velocity, impact force, displacement of the drop hammer, and the internal force at the beam-column connections. A variety of measuring equipment was used for test data acquisition. For example, high-speed cameras can obtain the impact velocity of the drop hammer at the moment of impact, and force sensors were used to measure the time history curves of the impact force during the impact test. As shown in Figure 4, the internal forces at the beam and column of the specimens were obtained by arranging strain gages. The horizontal reaction force at the end of the beam was measured by the

horizontal force sensor, and the vertical reaction force was calculated according to the strain data on the vertically constrained circular steel tube. The data acquisition system consisted of NATIONAL INS TRUMENTS NIPXIe-1085 Chassis with NI TB-4300 and NI TB-4330 board cards.

3. THE TEST RESULTS AND DISCUSSIONS

Table 1 summarizes the results of all the specimens during a single impact test, including impact velocity v_0, impact force peak $F_{I,p}$, impact force $F_{I,s}$ at the stable stage, duration t during the impact process, maximum vertical displacement u_{max}, axial force $N_{B,s}$ at the stable stage, and shear force $V_{B,s}$ at the stable stage.

3.1. Load-deflection curves and failure modes

Figure 5 shows the time history curves of impact force and mid-span vertical displacement during the single impact test. Combined with the results of the impact test in Table 1, the higher the impact velocity, the greater the peak impact force would be. Besides, values of $F_{I,p}$ of the WUF-B and the FP specimens were obtained through the test. WUF-B specimen was subjected to a higher impact velocity, so its $F_{I,p}$ was much larger than that of the FP specimen. At the same time, it can be seen that the impact force in the stable stage of specimen WUF-B was greater than that of specimen FP. In general, the impact force of the impact load on the specimen is far greater than the weight of the drop hammer itself. For the drop hammer with a mass of 1000 kg, it will produce a load of 9.8 kN on the structure under a static loading condition. When it falls from a height of 1.5 m, it will produce an instantaneous impact force of 1637 kN and a stable impact force of 130 kN on the structure, which is dozens of times more than that under the static loading condition. As the height of the fall increases, the impact force will increase further.

Table 1. Test results under single impacts

Specimen ID	Mass m (kg)	Height h (m)	Impact velocity v_0 (m/s)	Peak impact force $F_{I,p}$ (kN)	Maximum displacement u_{max} (mm)	Duration t (ms)	Shear force $V_{B,s}$ (kN)	Axial force $N_{B,s}$ (kN)
WUF-B	1000	4.5	9.29	2943	249.1	75.3	62 (left) 84 (right)	175 (left) 175 (right)
FP	1000	1.5	5.37	1637	115.8	73.0	80 (left) 61 (right)	5 (left) 6 (right)
RCC	1000	4.5	9.29	-	229.2	73.7	77 (left)） 78 (right)	86 (left) 87 (right)

Note: During the impact test of specimen RCC, the impact force time history curve of specimen RCC could not be obtained because the connection wire of the hammer force sensor was damaged in the impact process, so the data of specimen RCC in the table was missing.

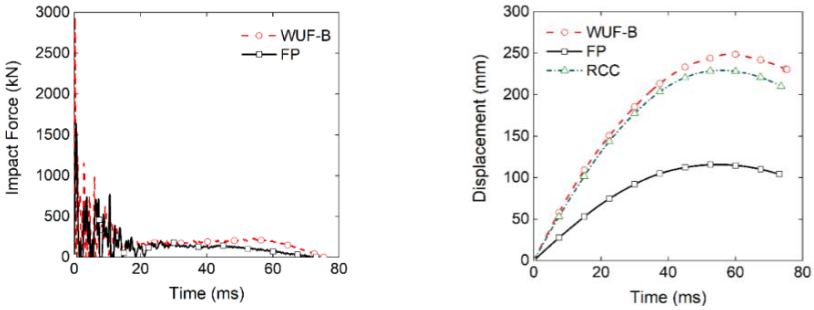

(a) Impact force (b) Midspan displacement

Figure 5. Time-history curves of impact force and displacement under a single impact

The resistance of the specimen to the impact load is a process of energy absorption. Therefore, when the impact energy is large, the specimen needs to undergo larger deformation to absorb the impact energy. According to the impact velocity of the drop hammer given in Table 3, the initial kinetic energy E_k of the drop hammer in the test can be calculated. For specimens WUF-B and FP, the values of E_k of the drop hammer in the test were 43.15 kJ and 14.42 kJ, respectively. The stable impact force of specimen FP was smaller than that of specimen WUF-B. Its maximum displacement was only 115.8 mm, which was smaller than the latter (249.1 mm). For specimen RCC, although its input energy was the same as that of specimen WUF-B, its deformation was also slightly smaller than that of specimen WUF-B, with a maximum displacement of 229.2 mm. When the impact energy increased, the duration of the impact process would be longer.

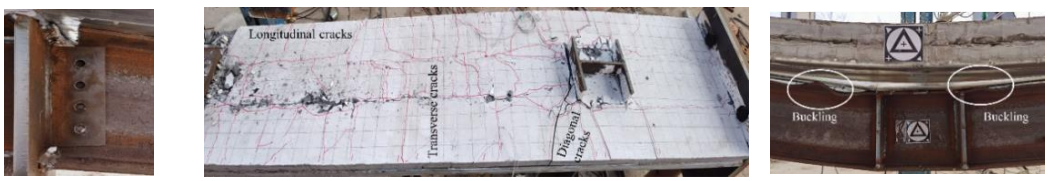

(a) Left connection (b) Top slab. (c) Midspan

Figure 6. Failure modes of WUF-B under a single impact

Figure 6 shows the deformation and failure modes of the WUF-B specimen after the first impact loading. In the impact loading, a negative bending moment appeared at the connection position. The left connection was damaged while the upper flange of the steel beam near the connection was tensioned and broken. Besides, the bolt was fractured (Figure 6(a)). The positive bending moment occurred at the impact position in the mid-span, and the upper flange of the steel beam buckled under compression, while the lower flange was tensioned. The composite slab and steel beam resisted the bending moment together, and a large shear force was generated at the interface of the two. Some shear studs near the mid-span position failed, and the composite slab and steel beam broke apart (Figure 6(c)). Two longitudinal cracks were

running through the composite slab along the beam cross direction at the rib position of the profiled steel plate. According to the analysis, the thickness of concrete at the position of slab ribs is 35 mm, which is only half of that at other positions (75 mm), and the impact occurred in the middle of the two slab ribs of the composite slab. During the impact process, the composite slab on both sides of the slab ribs had larger inertia, and the composite slab generated a larger bending moment perpendicular to the axis of the beam. These two reasons may lead to the emergence of longitudinal cracks through the area. Under the action of the negative bending moment of the connection, several main oblique cracks along the width direction of the composite slab at the joint appeared. Several small cracks perpendicular to the beam span were uniformly distributed on the composite slab, and the gap between cracks was about 15 cm, which was attributed to that the deformation of specimen WUF-B was mainly beam flexural deformation. In addition, the top slab concrete near the impact position in the span of the specimen was crushed under a positive bending moment (Figure 6(b)).

3.2. Discussions on load-resisting mechanisms

Figure 7 shows the equilibrium of the forces under impact load. The specimen resisted the impact force through inertia effect and structural resistance. When the specimen was deformed under the impact force, the shear force and axial force direction of the connection section changed with the angle of the beam end, and the component in the vertical direction was generated. Therefore, both the shear force and axial force contribute to the load resistance of the specimen to the impact force, as shown in Eq. (1) [8].

$$F_I = F_{ine} + V_{B,L}\cos\theta + N_{B,L}\sin\theta + V_{B,R}\cos\theta + N_{B,R}\sin\theta \tag{1}$$

Where F_I represents the impact force, F_{ine} is the contribution of inertia effect, $V_{B,L}$ and $N_{B,L}$ are the shear force and axial force of the left joint of the specimen; $V_{B,R}$ and $N_{B,R}$ are the shear force and axial force of the right joint of the specimen, respectively. θ is the angle of the beam end.

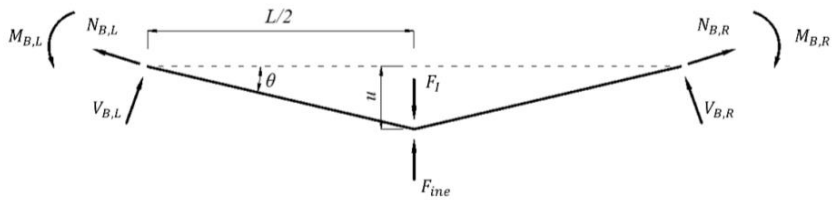

Figure 7. Equilibrium of forces under impact load [8]

The contribution of shear force to impact load resistance was calculated by $V_B\cos\theta$, and the axial force contribution was calculated by $N_B\sin\theta$. Whether the connection of the specimen was rigid, pin, or semi-rigid, the shear force of the specimen was always in the opposite direction of the impact force in the process of resistance to the impact load. In the early stage of the impact process, the axial force was in compression, and in the later stage, it was in tension with the increase of specimen deformation. As the impact force was far away from the

connection section, it can be considered that the shear force of the section represents the contribution of the flexural action (FA). As for axial force, when it was in compression, it was regarded as the contribution of compressive arch action (CAA). When it appears as a tensile force, it was regarded as the contribution of catenary action (CA). The sum of FA, CAA and CA was structural resistance.

$$F_{FA} = V_{B,L}\cos\theta + V_{B,R}\cos\theta \tag{2}$$

$$F_{CAA} = |N_{B,L}|\sin\theta + |N_{B,R}|\sin\theta, \qquad N_{B,L} < 0, N_{B,R} < 0, \tag{3}$$

$$F_{CA} = N_{B,L}\sin\theta + N_{B,R}\sin\theta, \qquad N_{B,L} > 0, N_{B,R} > 0 \tag{4}$$

$$F_L = F_{FA} + F_{CAA} + F_{CA} \tag{5}$$

$$F_{ine} = F_I - F_L \tag{6}$$

Where F_L represents structural resistance, F_{FA} represents the contribution of FA, F_{CAA} represents the contribution of CAA, and F_{CA} represents the contribution of CA. Eqs. (2) to (6) [8] can be used to quantitatively evaluate the contribution of different resistance mechanisms in the process of resistance to impact loads.

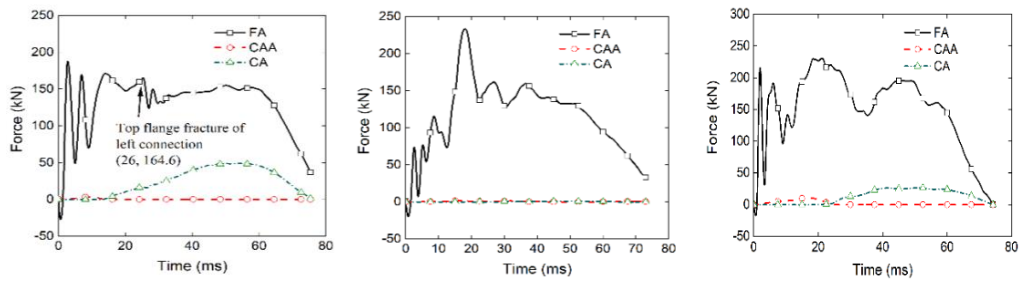

(a) WUF-B (b) FP (c) RCC

Figure 8. Load resistance mechanism

Figure 8 shows the load resistance contributions of the three specimens. Taking the WUF-B specimen in Figure 8 (a) as an example, the contribution of FA in the initial stage accounted for about 98% of the structural resistance, while the contribution of CA was only 2%. This is because the deformation of the specimen as well as the angle of the beam end were small. In the later stage, the contribution of FA gradually stabilized and always provided the most structural resistance. With the continuous deformation of the specimen, the axial force of the section changed from compression to tension, and CA began to develop. At this stage, due to the different deformation degrees of the three specimens, their resistance mechanisms were

also different. For the WUF-B specimen, the fracture of the upper flange of the steel beam occurred at the left joint of the specimen at 26 ms, which resulted in the decrease of the resistance provided by FA and led to the rapid development of CA. Finally, the contribution of FA and CA accounted for 76% and 24%, respectively. Therefore, in the process of resistance to impact load, the contribution of different resistance mechanisms was related to the deformation degrees and failure modes of the specimens.

4. FINITE ELEMENT ANALYSIS

4.1. Modelling details and verifications

As shown in Figure 9, the finite element model was established by ANSYS/LS-DYNA software. The model includes the complete specimen and its column end hinged-supports, beam end hinged-supports, and pin shaft. The constraint conditions of the specimen in the test were simulated by constraining the hinged supports. Most modelling details were similar to those reported previously by Chen et al. [9]. Currently, there is a lack of research investigating the impact behaviour of Composite beam. To address the technology gap, parametric analyses were conducted on composite beams with various connection types (including WUF-B, FP and RCC) under a mid-span impact scenario. Parameters related to impact load and structural design were investigated and presented. Meanwhile, the impact loading system of the drop hammer was simplified reasonably, and only the hammer head was retained. By adjusting the density of the hammer material, the weight of the drop hammer was consistent with the test, and the number of non-essential elements was reduced to improve the calculation efficiency.

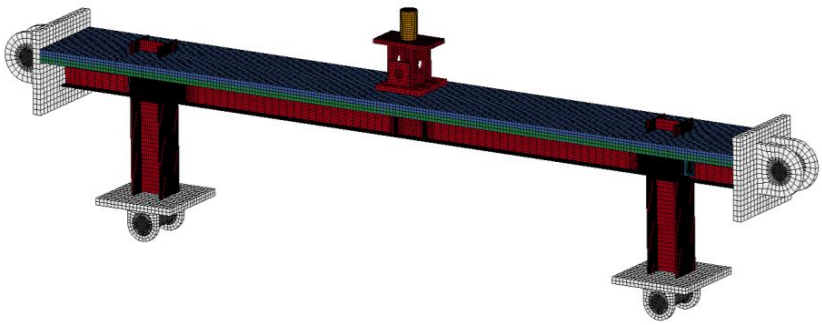

Figure 9. FE models of joint specimens (WUF-B) [9]

The mechanical properties of steel material were obtained before the conduction of tests, and the strain rate effect was taken into account by defining Cowper-Symonds [17] coefficients C and p as 6844 s^{-1} and 3.91 [18], respectively. ANSYS LS/DYNA provides many material models for capturing the dynamic properties of concrete, including the kinematic hardening model (Mat 25), K&C model (Mat 73), JHC model (Mat 111), and CSCM model (Mat 159).

To balance accuracy and computation time, different mesh sizes were used in the analysis. For large deformation zones such as bolts, fin plates, and welding areas, cube elements with a side length of around 2.5 mm were employed. Hexahedron elements with a side length ranging from

25 to 50 mm were used for elastic zones like beams, columns, and supports. The graded mesh was applied between the fine and coarse meshes. For the concrete slab, cube elements with a side length of 10 mm were adopted, and three layers in the thickness direction were modelled.

In the experiments, pinned supports were applied as boundary conditions to restrain the tested specimens, representing the inflection points. In the numerical analysis, these pinned supports, consisting of pins and brackets, were also modelled. Overall, these modelling and meshing techniques were employed to accurately simulate and analyse the behaviour of the materials and structural components involved in the study.

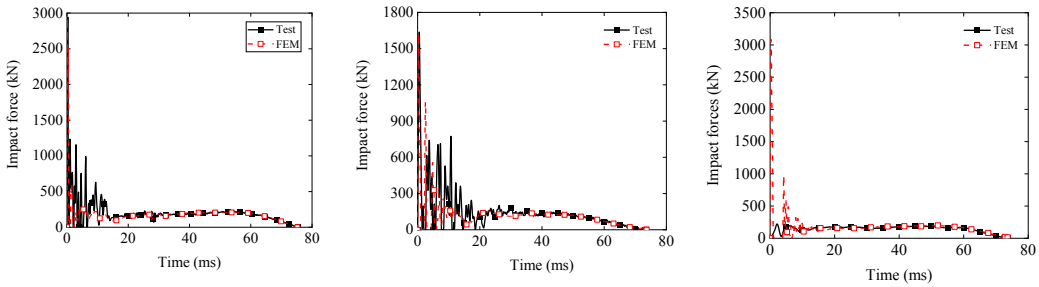

(a) WUF-B (b) FP (c) RCC

Figure 10. Comparison of single impact tests and FEM

Figure 10 shows the comparison between the impact force time history curves obtained by finite element simulation and the test results. It can be seen that the time history curves obtained by finite element simulation were in good agreement with the impact test results. Figure 11 compares the deformation and failure modes of specimens in the FEM with the impact test. The FEM can better capture the deformation and failure modes of composite structures with different beam-column connections under impact loads, including the failure modes of connections and composite slabs. In conclusion, the finite element model established in this paper can well simulate the dynamic response process of plane composite frame substructure under impact loads.

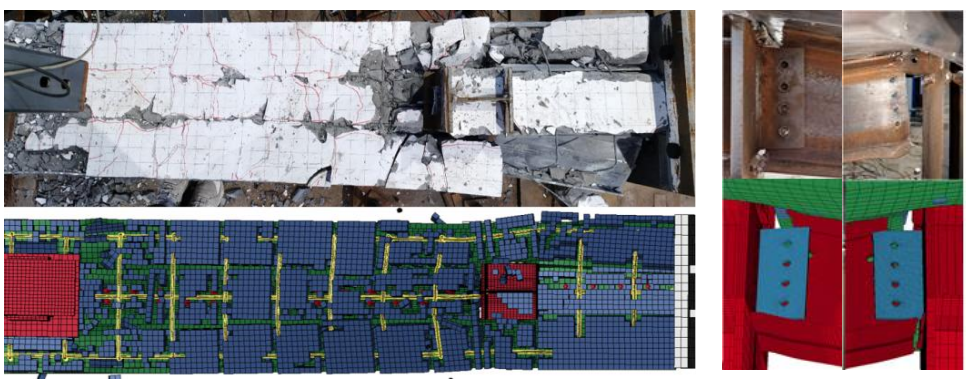

(a) WUF-B slab (b) WUF-B connection

Figure 11. Comparison of failure modes between test and FEM of WUF-B [9]

4.2. Parametric analysis

The finite element model was established and verified, and a series of parametric analysis were carried out based on the benchmark model. The contribution of composite slabs to the impact resistance of composite structures with different connections was compared, and the influence of concrete strength, slab thickness, profiled steel plate thickness, reinforcement ratio, shear stud distance, and span-to-depth ratio on the impact resistance of composite slabs was discussed. Due to a large number of calculation examples, the calculation examples were named in the way of 'connection type-parameter-specific value'. For example, WUF-B-CS-C30 represents the calculation example whose connection type is welded unreinforced flange-bolted web and concrete grade is C30.

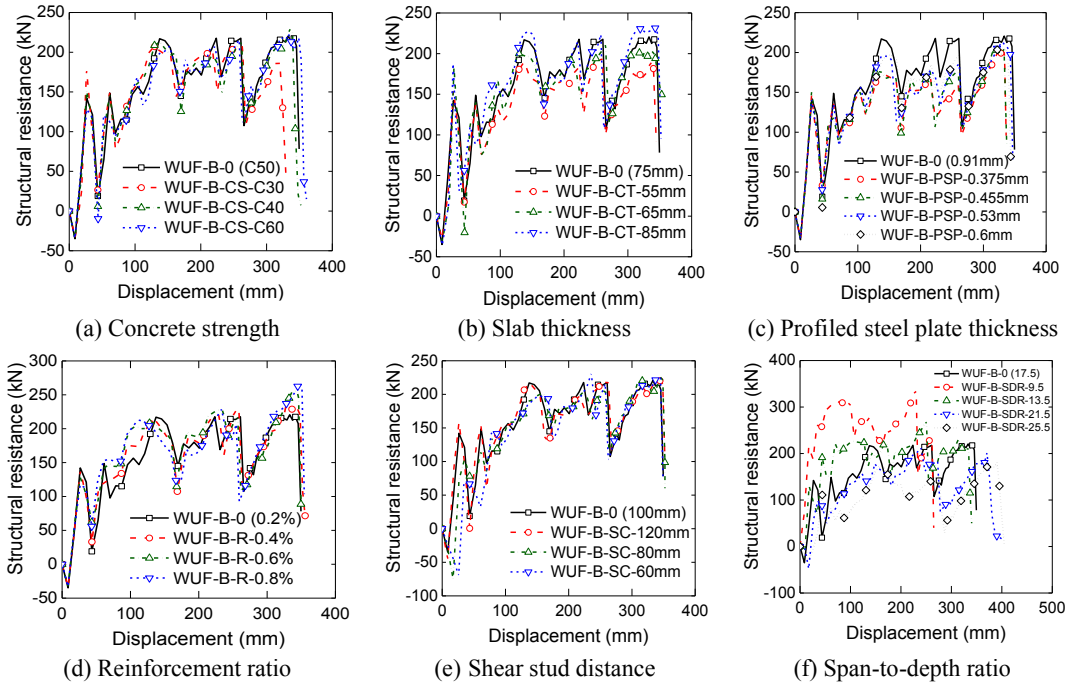

(a) Concrete strength (b) Slab thickness (c) Profiled steel plate thickness

(d) Reinforcement ratio (e) Shear stud distance (f) Span-to-depth ratio

Figure 12. Effect of parameters on the impact resistance of composite structures

Figure 12 shows the influence of various parameters on the load resistance-displacement curves of specimen WUF-B. It was found that the composite slab significantly improves the impact resistance of the specimen. Composite slabs can play a tensile role after the upper flange of steel beam fractures. The higher the concrete strength was, the higher the structural resistance will be developed after the upper flange of steel beams was broken. The larger the failure displacement of the specimen, the more energy it can absorb. However, when the concrete strength grade was above C40, the difference in impact resistance was small. For example, the energy absorption capacity of WUF-B-CS-C60 was 9.3% higher than that of WUF-B-CS-C30, but only 3.9% higher than that of WUF-B-CS-C40. Figure 12(b) shows the influence of

concrete slab thickness on the impact resistance of specimens with different connection forms. It was found that the impact resistance of specimens WUF-B was greatly affected by the thickness of concrete slabs, and the structural resistance of specimens increased with the increase of slab thickness, while the failure displacement was the same. As shown in Figure 12(c), the increase in the profiled steel plate thickness can significantly improve the structural resistance and slightly increase the failure displacement. The energy absorption capacity of WUF-B-PSP-0.6 mm (corresponding to 1.2 mm in the prototype specimen) was 6.6% higher than that of WUF-B-PSP-0.375 mm, and that of WUF-B-0 (0.91 mm thickness) was 13.5% higher than that of WUF-B-PSP-0.375 mm.

As shown in Figure 12(d), for specimen WUF-B, the increase in reinforcement ratio can improve the structural resistance of the specimen, especially at the first peak value and before the final specimen failure. The increase of structural resistance at the first peak value was mainly due to the reinforcement tension at the connection. Meanwhile, the compression of the lower flange of the steel beam contributed to the specimen resisting the negative bending moment and improved FA in the specimen. However, the improvement of structural resistance before the final connection failure was due to the enhancement of CA. With the increase in reinforcement ratio, the failure displacement of the specimen also increased slightly. Higher structural resistance and larger displacement allowed the structure to absorb more energy. The energy absorption capacity of WUF-B-R-0.8% was 8.6% higher than that of WUF-B-0 (0.2%). It should be noted that when the reinforcement ratio exceeded 0.6%, the continuous increase of the reinforcement ratio had a weakened effect on the impact resistance of specimens. As shown in Figure 12(e), when the shear stud distance was more than 100 mm, the structural resistance and displacement curves of the two specimens coincided. When the distance of the studs was decreased to 80 mm, the structural resistance of the specimen in the early stage was slowed down, while the structural resistance was significantly increased in the middle and late stages, and the failure displacement had little effect. For the improvement of structural resistance in the early stage, the main reason is that FA was enhanced with the increase of shear connection strength, while CA had little change. As can be seen from Figure 12(f), with the increase of span-to-depth ratio (SDR), the structural resistance of specimen WUF-B increased, the failure displacement decreased, and the energy absorption capacity of specimens decreased. When the SDR increased from 9.5 to 25.5, the energy absorption capacity of the specimens decreased by 39.8%.

5. CONCLUSIONS

In this paper, impact tests of three planar composite frame substructures with different connection forms were completed, FE models of impact tests were established using ANSYS/LS-DYNA software, and a series of numerical analysis were carried out. The following main conclusions can be drawn:

- In the initial stage of the impact process, the specimen resists the impact load through inertia force, while in the later stage, it mainly resists the impact load through structural resistance. Structural resistance is mainly provided by FA and CA, while the contribution of CAA is very limited and can be ignored.

- The energy absorption capacity of the specimen is an important index to evaluate its impact resistance. When the structure has good flexural resistance, the specimen can absorb more energy under the same displacement. When the deformation ability of the specimen is good, the structural resistance provided by FA can be kept from decreasing while the structural resistance provided by CA can be continuously improved. The RCC specimen showed the best impact resistance in the test because of the good flexural and deformation ability.
- The finite element model established in this paper can accurately simulate the dynamic response of the composite structure under impact load. The impact force and displacement time history curves, and the failure modes obtained through FEM are in good agreement with the test results.
- The failure mode of specimen WUF-B was the complete fracture of the upper and lower flange of the steel beam. The failure mode of specimen FP was that the bolt at the joint was sheared out. The failure mode of the RCC specimen was that the end plate was torn and the bolt was pulled out of the end plate bolt hole.
- The parameter analysis shows that the composite slab can improve the impact resistance of the composite structure. Among them, specimen WUF-B had the most obvious improvement, and specimen RCC was the weakest. The profiled steel plates can improve the development of CA in the structure. The strength and thickness of concrete, the thickness of profiled steel plates, the reinforcement ratio of the composite slab, and the shear stud distance all affect the impact resistance of composite structures, but the effect is different for different connection forms. In summary, the influence of the longitudinal reinforcement ratio of the composite slab is the most obvious.

ACKNOWLEDGMENTS

The authors gratefully acknowledge the financial support provided by National Natural Science Foundation of China (No. 51778086 and No. 52078079), the Research Development Fund of XJTLU (Grant No. RDF-22-02-093).

REFERENCES

[1] Kaewkulchai, G., Williamson, E. (2006). Modeling the impact of failed members for progressive collapse analysis of frame structures. *Journal of Performance Constructed Facilities*, 20(4), 375-83.

[2] Stoddart, E., Byfield, M., Davison, J., and Tyas, A. (2013). Strain rate dependent component based connection modelling for use in non-linear dynamic progressive collapse analysis. *Engineering Structures*, 55, 35-43.

[3] Fujikake, K., Li, B., and Soeun, S. (2009). Impact response of reinforced concrete beam and its analytical evaluation. *Journal of Structural Engineering*, 135 (8), 938-950.

[4] Grimsmo, E., Clausen, A., Aalberg, A., and Langseth, M. (2016). A numerical study of beam-to column joints subjected to impact. *Engineering Structures*, 120, 103-15.

[5] Kadhim, M., Wu, Z., and Cunningham, L. (2019). Experimental and numerical investigation of CFRP-strengthened steel beams under impact load. *Journal of Structural Engineering*, 145, 04019004.

[6] Wang, H., Tan. K., and Yang, B. (2020). Experimental tests of steel frames with different beam-column connections under falling debris impact. *Journal of Structural Engineering*, 146, 04019183.

[7] Wang, H., Yang, B., Chen, K., Elchalakani, M. (2020). Parametric analysis and simplified approach for steel-framed subassemblies with reverse channel connection under falling-debris impact. *Engineering Structures*, 225, 111263.

[8] Yang, B., Chen, K., Wang, D., Elchalakani, M. (2022). Experimental study on composite beam with various connections under midspan impact scenarios. *Journal of Structural Engineering*, 148(10), 04022158.

[9] Chen, K., Wang, D., Yang, B., Lin, X., Elchalakani, M. (2022). Parametric study on composite beam with various connections under mid-span impact scenarios. *Engineering Structures*, 268, 114776.

[10] Lin, S., Wang, J., Qiao, H., Chen, H., and Zhou, Y. (2021). Performance of steel frames with different web bolt number and arrangements in a column-loss scenario. J*ournal of Structural Engineering*, 147 (10), 04021150.

[11] Wang, H., Huo, J., Elchalakani, M., Liu, Y., and Zhang, S. (2021). Dynamic performance of retrofitted steel beam-column connections subjected to impact loadings. *Journal of Constructional Steel Research*, 183, 106732.

[12] Wang, H., Huo, J., Liu, Y., Elchalakani, M., and Zhu, Z. (2021). Dynamic performance of composite beam-column connections subjected to impact loadings. *Journal of Constructional Steel Research*, 178, 106498.

[13] Vlassis, A., Izzuddin, B., Elghazouli, A., and Nethercot, D. (2009). Progressive collapse of multi-storey buildings due to failed floor impact. *Engineering Structures*, 31(7), 1522-1534.

[14] Huo, J., Zhang, J., Liu, Y., and Fu, F. (2017). Dynamic behaviour and catenary action of axially-restrained steel beam under impact loading. *Structures*, 11(8), 84-96.

[15] Yang, B., and Tan, K. (2013). Experimental tests of different types of bolted steel beam-column joints under a central-column-removal scenario. *Engineering Structures*, 54(9), 112-130.

[16] Yang, B., Tan, K., Xiong, G., and Nie, S. (2016). Experimental study about composite frames under an internal column-removal scenario. *Journal of Constructional Steel Research*, 121(6), 341-351.

[17] Cowper, G., Symonds, P. (1957). Strain-hardening and strain-rate effects in the impact loading of cantilever beams. *Technical Rep No 28 Prepared for Office of Naval Research*, Providence, R.I., USA: Brown University.

[18] Jones, N. (1997). Structural Impact: Cambridge University Press.

MITIGATING DAMAGE OF STRUCTURES UNDER BLAST LOADS USING LINEAR PROTECTIVE LAYERS

Eyal Eytam[1], Hezi Y. Grisaro[2]

[1] MSc Student, Faculty of Civil and Environmental Engineering, Technion – Israel Institute of Technology, Technion City, Haifa 32000, Israel. eyal.eytam@campus.technion.ac.il

[2] Assistant Professor, Faculty of Civil and Environmental Engineering, Technion – Israel Institute of Technology, Technion City, Haifa 32000, Israel. hezi@technion.ac.il

Corresponding Author: Hezi Y. Grisaro, PhD.

Faculty of Civil and Environmental Engineering, Technion – Israel Institute of Technology, Technion City, Haifa 32000, Israel

Email: hezi@technion.ac.il

ABSTRACT

The response of structures to blast loads commonly includes damage that cannot be avoided. The trivial method to enhance the structural resistance under blast loads is by stiffening its cross-section, which may lead to an uneconomical design regarding material weight and cost. An alternative method is to use sacrificial layers placed on the surface exposed to the blast loads and designed so that the damage will be redirected and concentrated on them, not on the main structure. After loading, the main structure experiences minimal damage, and the sacrificial layer can be replaced easily. Sacrificial layers commonly include voids, and during the dynamic response, the voids are closed, the damage is developed in the layers, energy is absorbed, and effective lower pressure is transmitted to the structure. With inspiration of sacrificial layers, this study suggests using linear protective layers (LPLs) instead of sacrificial layers, i.e., layers that will not experience any damage and are characterized by linear stiffness. This can be, for example, a plate connected by linear springs to the structure. Because they are linear, the load that is transmitted to the structure is not limited as in the sacrificial layer case. A two-degrees-of-freedom system is developed to study the effectiveness of the linear layer in reducing the damage. Several factors that affect the problem are discussed through a case study.

Keywords: *Blast Loads, Protective Layers, Structural Damage, Structural Dynamics.*

INTRODUCTION

Structures are commonly exposed to more standard loads such as dead loads, live loads, wind loads, etc. However, they can still be exposed to extreme loads such as blast loads or earthquakes. Blast loads are characterized by peak overpressure and short duration; therefore, their dynamic effect may be significant. They can be generated as a result of terrorist attacks, accidental explosions, etc. Structures of high importance, such as military structures, hospitals, power plants, etc., are commonly designed to withstand blast loads under predetermined scenarios [1–4]. Structures that are not explicitly designed to resist these loads could still be loaded, and therefore, sometimes, it is of interest to evaluate their level of damage and performance. When their level of damage is too high, it is necessary to mitigate structural damage.

The trivial method for reducing structural damage is by increasing its stiffness and capacity. There are several major disadvantages of implementing this design approach. First, the structural sections derived to withstand minimal damage are sometimes unrealistic. Next, the sections are over-reinforced; therefore, they are characterized by small potential ductility at failure, and the plastic design of these sections is not optimal. Finally, since these enhanced sections are very stiff, they transfer large reaction forces to the rest of the structural elements that support them. All these reasons make this method less economical.

An alternative approach to protect structures subjected to blast loads and mitigate damage to the main structure is by adding sacrificial protection layers, which absorb most of the damage, often by energy-absorbing layers [5–8]. Because it is challenging to eliminate the damage, the idea is to reduce damage to the main structure by redirecting the damage toward these layers. The sacrificial layers can be made of various materials. Commonly, porous materials that include voids are used, such as tubes, aluminum and metallic foams, honeycomb structures, etc. During compaction, the voids are closed, and during their crushing process, the actual transmitted pressure to the main structure is limited and small compared with the highly intense blast loads. In practice, one of the main effects of sacrificial layers is to limit the peak pressure transmitted to the structure, even when the transmitted impulse is similar.

After the blast event, the protection layer remains damaged, and replacement of those layers is needed to maintain the protection again. A motivation is raised in the current study to use a Linear Protection Layer (LPL), i.e. a protection layer that does not experience damage. The main idea is not to absorb energy, as opposed to sacrificial layers. Instead, the idea is to transmit the load to the structure in a different shape and duration than the original blast load, and ideally, this will reduce the structural damage. In other words, the structural response would be different due to delays in the transmission of the load and the different actual shapes of the transmitted load. Linear protection can theoretically offer a protection mechanism that eliminates the need for replacement. Another benefit LPL can suggest is protection from several and repeated blasts. However, the effect of interval duration between blasts should be considered since it may, in some cases, even increase damage to the main structure, depending on the state of the system during the additional impact (and this will not be discussed in this paper). The effect of the LPL on structural mitigation is not trivial. An illustration of LPL is

shown in Figure 1. In reality, the LPL can be a relatively stiff plate. That is connected to the main structure by linear springs that do not experience plasticity.

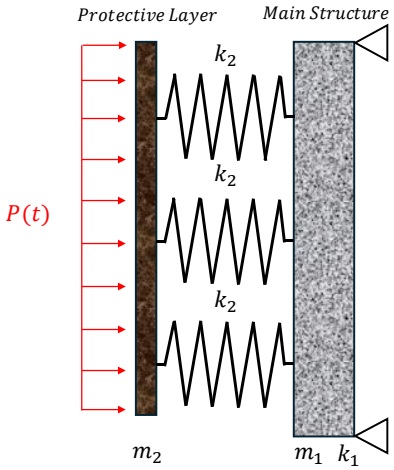

Figure 1. Illustration of LPL

The concept of the LPL is discussed in the current study. This study presents a preliminary analysis stage to investigate a basic and fundamental problem of using LPL through a simple model. It includes a representation of the equations of motion of the basic problem, and its solution through case studies. A discussion of the effectiveness of LPL is discussed, and motivation for future research is presented.

THE MODEL

The current study aims to investigate the basic dynamic problem to understand the fundamental principles of using LPLs. A simple Two Degrees Of Freedom (TDOF) model is used in the current study, as shown in Figure 2. The protective layer and the main structure (i.e. the structure being protected) are represented as a mass-spring system, including two masses and two springs, where m_1 and k_1 represent the mass and stiffness of the main structure, respectively, whereas m_2 and k_2 represent the mass and stiffness of the protective layer, respectively. Thus, the main structure is modeled by an equivalent Single Degree Of Freedom (SDOF) approach. This approach is very common as an approximation for designing structures under blast loads [1,2,9,10]. The blast load is represented by $P(t)$ and acts on the protection layer, where t is the time coordinate. The current study considered a simple triangular-shaped blast load with peak force P_0 and duration t_0 (therefore, the impulse is $I_0 = 0.5P_0t_0$). In cases where no protection layer is considered, the blast load acts directly on the structure. The displacements of the structure and the protection layer are $x_1(t)$ and $x_2(t)$, respectively.

In the current basic study, the structural element is characterized by a linear resistance function (i.e. the spring that represents the structure is linear). However, any plasticity can be easily implemented in the proposed framework because the solution scheme is explicit, as explained in the following text. An additional assumption considers that the LPL is in its elastic regime, i.e. there is neither limit on the compression nor on the tension level of the LPL spring. In reality, there is a certain level of limitation to this compression and tension, and if this limiting

value is reached, the LPL experiences damage and, therefore, is not useful for the goals raised in the current study. However, this remains a limitation at this stage, and first, the basic coupled problem is discussed.

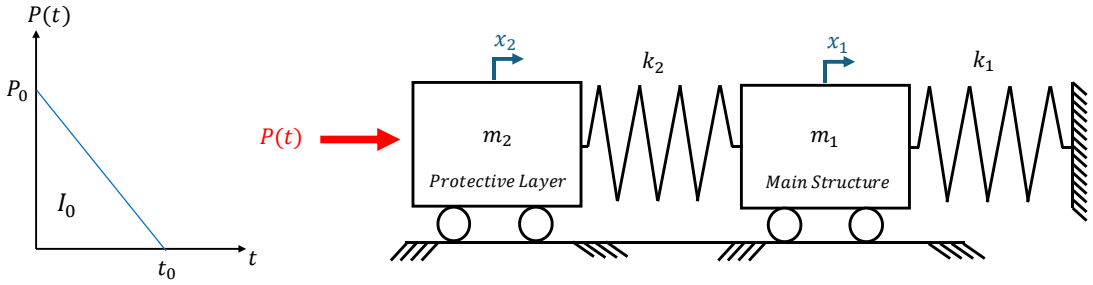

Figure 2. TDOF model.

The equations of motion for the coupled system are shown in Eq. (1), and the equation of motion of the unprotected structure is shown in Eq. (2).

$$\begin{bmatrix} m_1 & 0 \\ 0 & m_2 \end{bmatrix} \begin{bmatrix} \ddot{x}_1(t) \\ \ddot{x}_2(t) \end{bmatrix} + \begin{bmatrix} k_1 + k_2 & -k_2 \\ -k_2 & k_2 \end{bmatrix} \begin{bmatrix} x_1(t) \\ x_2(t) \end{bmatrix} = \begin{bmatrix} 0 \\ P(t) \end{bmatrix} \tag{1}$$

$$m_1 \ddot{x}_1(t) + k_1 x_1(t) = P(t) \tag{2}$$

Since a linear spring is used, the equations are linear in terms of the resistance function, and therefore, analytical solutions exist (if a particular solution of the differential equations exists based on the chosen pressure pulse shape). We intend to extend the basic study into more complex systems, which involve several factors of nonlinearity, and we expect to develop a system that does not have closed-form solutions. Therefore, a numerical procedure was also developed, and the equations were solved using the explicit version of Newmark's beta method, which is equivalent to an explicit finite difference method [11]. In the numerical method, the timestep was chosen to be small enough to achieve both stability of the solution and convergence of the results. In the current study, the analytical and numerical solutions were identical to the numerical predictions, as expected.

EXAMPLES

This section presents three case studies. The examples were chosen to demonstrate initial insights regarding the effect of the LPL on the protection of a structure. The main goal of the examples is to compare the response of the unprotected structure with the protected structure (to evaluate the effect of reducing the structural damage) and also to evaluate indirectly the effect of the chosen protection layer stiffness on the results. As will be shown in the case studies, the specific examples show interesting results regarding the performance of the coupled system.

Case study 1

The first case study includes a structure with a mass of m_1 = 100 kg and stiffness k_1 = 10 kN/m. Note that the actual values do not necessarily represent a realistic case, and they are given to study the fundamental concept. The blast load is characterized by a peak force of P_0 = 50 kN and duration t_0 = 20 msec, which corresponds to an impulse of I_0 = 500 kN-msec. Firstly, the response of the structure is calculated for the given blast load, i.e. the blast load acted directly on the structure without any protection. This scenario is referred as the response or the "unprotected" structure. The obtained displacement-time history of the unprotected structure and the applied blast load are shown in Figure 3a and Figure 3b, respectively.

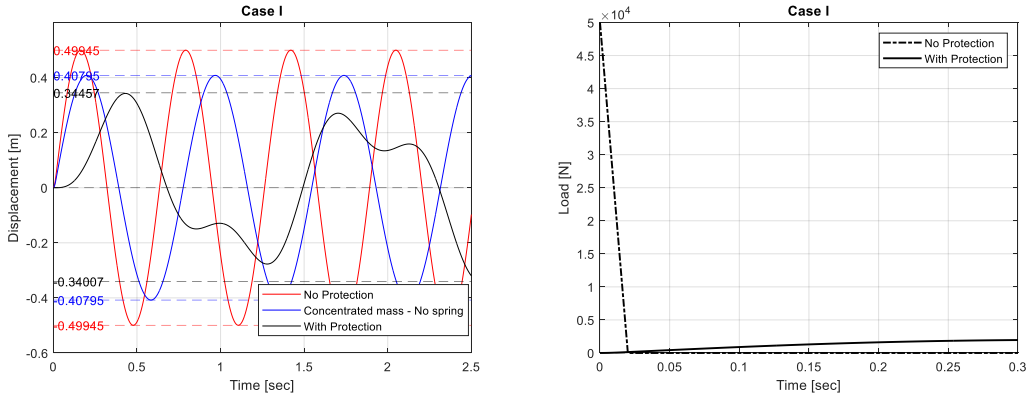

(a) (b)

Figure 3. Results of case study 1: (a) displacement-time history. (b) effective load acting on the main structure

The protection layer, in this case, has a mass of m_2 = 50 kg and stiffness of k_2 = 1 kN/m. In that case, and as mentioned before, the blast load acts on the protection layer, and not directly on the structure. In fact, the load transmitted to the structure is the force in the spring that characterizes the protection layer. The coupled system is solved, and the obtained displacement-time history is shown in Figure 3a and Figure 3b, respectively. It can be seen that by applying the LPL, the maximum displacement of the structure was smaller than that of the unprotected case. This corresponds to the actual load that is transmitted through the spring to the main structure, which is characterized by significantly lower pressures than the original blast load. Note that the blast load is in the impulsive regime because its duration is relatively short compared with the response of the structure.

An interesting discussion can be made on the effect of the LPL on the structural response. The reduction in the maximum displacement of the main structure is traditionally associated with the energy absorption in sacrificial layers. In the current case, as an equivalent method, it may be associated with the effect of the LPL spring and its stiffness. However, it should be noted that the LPL also provides mass to the system. This means that even when the LPL spring is completely rigid (and the protection is effectively attached to the structure), and the blast load acts directly on the structure, it still provides an additional mass to the main structure. Therefore, in the theoretical case of $k_2 \rightarrow \infty$, the equation of motion reads:

$$(m_1 + m_2)\ddot{x}_1(t) + k_1 x_1(t) = P(t) \quad (3)$$

Therefore, a modified dynamic response can be obtained just by modifying the mass component in the system. This system was solved, and the results are shown in Figure 3. Figure 3 shows that the maximum displacement obtained using the additional (or concentrated) mass approach is smaller than the unprotected case, but larger than the fully coupled system. This means that we could indirectly separate the effects of the additional mass component and the effect of the spring on the results, and we could evaluate their contribution quantitively.

Case study 2

Case study 2 includes the same parameters as the previous one, but with a different blast load. In this case, the peak force was P_0 = 15 kN and duration t_0 = 750 msec, which corresponds to an impulse of I_0 = 5,625 kN-msec. The displacement-time histories for the three cases (unprotected structure, the coupled LPL and structure system, and a structure with a mass m_1+m_2) are shown in Figure 4a and Figure 4b, respectively.

In this case, it is shown that by applying the LPL on the structure, the maximum displacement was smaller than in the unprotected case, but the reduction was insignificant. There was a shift in the time of maximum displacement. Note that in this case, the blast load is in the dynamic regime since its duration is comparable with the response time up to the maximum displacement. When a structure with additional mass was considered, the displacement was smaller compared with the unprotected case, but also smaller than the coupeld system. The conclusion is that the effect of the spring was negative in terms of protection.

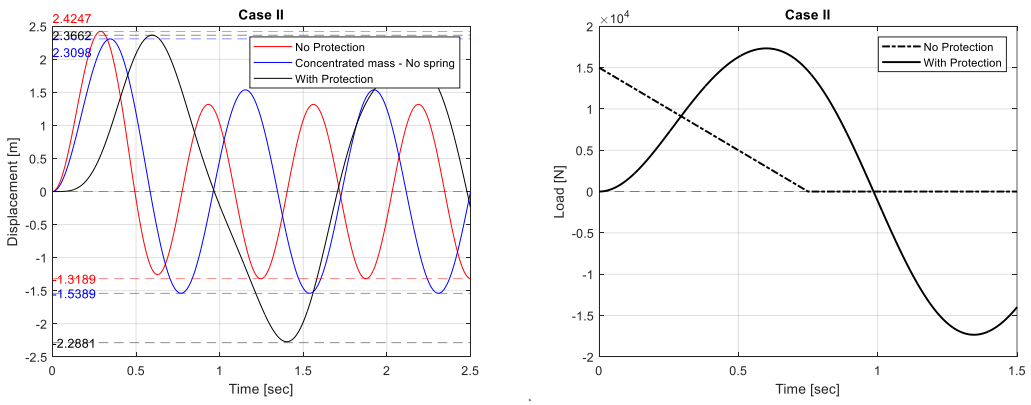

Figure 4. Results of case study 2: (a) displacement-time history. (b) effective load acting on the main structure

Case study 3

Similarly to case study 2, the blast load was modified also in this example. The blast load had a peak force of P_0 = 5 kN and duration t_0 = 1,100 msec, which corresponds to an impulse of I_0 = 2,750 kN-msec. The results are presented in Figure 5. Here, using the LPL in the coupled system increased the maximum displacement of the system, and thus, its effect was negative in terms of protection. When the response of the structure was calculated using the increased mass, the maximum displacement was smaller than that of the unprotected case. Therefore, it

can be concluded that in this case, the additional mass contributed to a reduction of damage in the structure, but the effect of the spring was negative, even with the reference unprotected case. The blast load applied in this case is in the quasi-static regime, and its duration is relatively long.

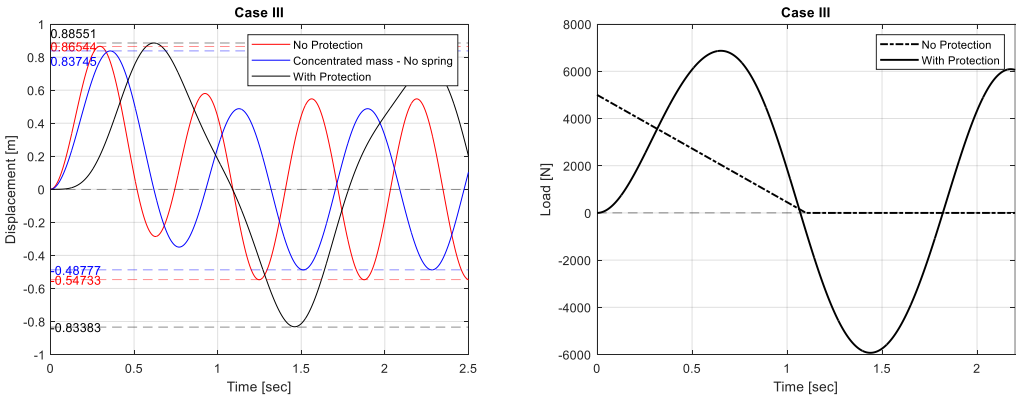

Figure 5. Results of case study 3: (a) displacement-time history. (b) effective load acting on the main structure

Discussion

The presented case studies show that the effect of the LPL, and particularly the effects of the addition of mass to the system and of the LPL spring stiffness, are not trivial. The three cases showed different trends. Therefore, a full understanding of the LPL behavior is needed in order to design it properly and optimally, and avoid negative effects. In addition, the protection filtered the transmitted load into a different load-time history. Therefore, the response of the structure may be different in terms of quasi-static, dynamic and impulsive regimes.

This study put a preliminary foundation for a deeper investigation. Firstly, the response over the full load spectrum is of interest since, just by changing the external load, we derived different trends in the results. Next, the relation between the values of the LPL spring stiffness and the stiffness of the main structure should be investigated to achieve optimal reduction. The same applies to the ratio of the LPL mass and the main structure mass. Finally, a full understanding of the coupled system for a given set of structural parameters may provide a method for achieving the optimal design.

The current study provides insights derived from a simple TDOF model. A more realistic scenario, in which the response of a continuous structure may be modeled to investigate a more realistic problem, which will implement the basic understanding raised from the current study. One of the limitations of the current study is associated with the failure of the LPL spring. The LPL spring cannot experience failure. A more realistic scenario will include both the failure of the LPL (and, therefore, a constraint on the maximum allowed compression or tension of the LPL spring). In addition, plasticity in the main structure should be considered to simulate possible structural damage, at least in the unprotected case. All these aspects will be considered in future studies.

CONCLUDING REMARKS

This study suggests investigating the effectiveness of a protection layer (LPL) represented by linear resistance function, i.e. without yielding. The application of the LPL provides provisions for the structural mass and modification of the equation of motion of the coupled system. The effect of the LPL was studied by simulating the coupled system and a structure with additional mass. Therefore, the two effects of the LPL (the contribution of its spring and the contribution of its mass) were studied indirectly separately.

The results showed that the effect of the LPL is not trivial and depends on the parameters of the structural system and the applied blast load. A more detailed investigation is needed to fully understand the coupled dynamics and the effect of the parameters on the results.

REFERENCES

[1] USACE. Protective Design Center. Methodology Manual for the Single-Degree-of Freedom Blast Effects Design Spreadsheets (SBEDS). PDC TR-06-01 Rev 1 2008.

[2] USACE. Unified Facilities Criteria (UFC) - Structures to resist the effects of accidental explosions. UFC 3-340-02, U.S Army Corps of Engineers: 2008.

[3] CSA. Design and assessment of buildings subjected to blast loads, CSA S850-12, Canadian Standards Association. Toronto, ON: 2012.

[4] ASCE. Blast protection of buildings, ASCE/SEI 59-11, American Society of Civil Engineers. Reston, VA: 2011.

[5] Hanssen AG, Enstock L, Langseth M. Close-range blast loading of aluminium foam panels. International Journal of Impact Engineering 2002;27:593–618. https://doi.org/10.1016/S0734-743X(01)00155-5.

[6] Ma GW, Ye ZQ. Energy absorption of double-layer foam cladding for blast alleviation. International Journal of Impact Engineering 2007;34:329–47. https://doi.org/10.1016/j.ijimpeng.2005.07.012.

[7] Wu C, Huang L, Oehlers DJ. Blast Testing of Aluminum Foam–Protected Reinforced Concrete Slabs. Journal of Performance of Constructed Facilities 2011;25:464–74. https://doi.org/10.1061/(asce)cf.1943-5509.0000163.

[8] Shim C, Yun N, Yu R, Byun D. Mitigation of Blast Effects on Protective Structures by Aluminum Foam Panels. Metals 2012;2:170–7. https://doi.org/10.3390/met2020170.

[9] Grisaro HY. Pressure-Impulse diagrams for assessment of structural response due to a fully confined explosion. Engineering Failure Analysis 2023;146:107103. https://doi.org/10.1016/J.ENGFAILANAL.2023.107103.

[10] Rigby SE, Tyas A, Bennett T. Single-Degree-of-Freedom response of finite targets subjected to blast loading – The influence of clearing. Engineering Structures 2012;45:396–404. https://doi.org/10.1016/J.ENGSTRUCT.2012.06.034.

[11] Chopra AK. Dynamics of structures. Pearson; 2017.

THE EFFECT OF STATIC PRELOADS ON RC BEAMS AND SLABS SUBJECTED TO BLAST LOADS

Scott McFadden[1], Wesam Njeem[2], Ashok Malhotra[3], and Laura Ciornei[4], P.Eng.

[1] Senior Engineer, WSP Canada, Scott.McFadden@wsp.com.

[2] Structural Designer, WSP Canada, Wessam.Njeem@wsp.com.

[3] Senior Principal, WSP Canada, Ashok.Malhotra@wsp.com.

[4] Structural Designer, WSP Canada, Laura.Ciornei@wsp.com.

Corresponding Author: Scott McFadden, P.Eng.

150 Slater 7th floor, Ottawa, Ontario, Canada, K1A 1K3

Email: Scott.McFadden@wsp.com

ABSTRACT

Design standards for blast resistant design, such as Canadian standard CSA S850-23, contain load combination provisions for static loads, such as dead, live and snow, used concurrently with dynamic blast loads. These static loads preload the structure with an initial state of internal stress and displacement before and during blast loading. The structural response using this load combination can be predicted using non-linear time history dynamic analysis, which is commonly simplified with a Single Degree of Freedom (SDOF) model, by including the static loading and initial state conditions. The components of structure where static loads are applied concurrently with blast loads are beams and slabs spanning horizontally, and the blast loading direction is considered the same as the gravity.

This paper introduces a method using a closed form equation to predict the peak structural response that includes preloading due to the static load as required by the CSA S850-23 load combinations. This equation uses the principle of energy conservation which is applicable for structures responding in the impulsive dynamic range. In addition, the closed form equation results are compared to the results of SDOF analysis over a range of load durations and natural periods of the member, including both impulsive and dynamic structural responses.

Keywords: *Blast Resistant Design, Preload, Reinforced Concrete Beams, SDOF Dynamic Analysis, Blast Load Combinations.*

INTRODUCTION

Many structures respond in the impulsive dynamic range given that the duration of blast loading is much shorter than the natural period of the structure. For these structures, the peak response to blast loading can be predicted using the conservation of energy method of analysis. Use of this method results in closed form equations to predict the peak structural response to blast loading. This closed form equation is a function of the resistance, natural period of vibration, and imparted blast load. This approach can simplify the required computational effort compared to more rigorous non-linear time history analysis. It also can be used in preliminary design and as a validation tool for more rigorous methods [1].

Structures that resist gravity loads concurrently with blast loading have an initial load state, or preload, which should be considered when predicting the peak structural response. The inclusion of preload on the structure is required as recommended in the design standards such as CSA S850-23 using load combinations [2]. Preload is considered significant in structures members such as beams and slabs spanning horizontally. In addition, based on the literature review, the closed form equation is derived without considering the preload on the structure, and it only considers the impulse imparted to the structure from the blast load [1].
The closed form equation can be used to predict the peak displacement using a 'remaining strength' method. According to the 'remaining strength' method, the resistance of the structure is reduced based on the preload force and the peak displacement is determined relative to the initial preload displacement [3].

The peak response can also be predicted by using dynamic time history analysis which is commonly used with software for blast design such as SBEDS [7], and the use of a Single Degree of Freedom (SDOF) non-linear time history analysis. This paper compares the results of the closed form equations with the SDOF analysis over a range of preload to resistance ratios. Additionally, a comparison between non-preloaded and preloaded structures will be presented.

PREDICTING BLAST EFFECTS WITH PRELOAD

According to the literature review, two methods were considered to predict the response of structures with static preloads subjected to blast loading. The first method uses non-linear time history analysis, typically as a Single Degree of Freedom (SDOF), with preload as an initial state of stress and displacement corresponding to the static loading [3][4]. Software programs such as SBEDS use this method. The second method applies a reduction on the resistance of the structures during the non-linear time history analysis by the amount of the static preload, this is referred to as the 'remaining strength' method. Both methods predict the same peak response, however for the 'remaining strength' method, the static deflection of the preloads must be added to the peak dynamic response to blast loads.

For the cases when the structure has a natural period of vibration larger than the duration of the blast loading, by a factor of 10 or greater, the response is referred to as impulsive. This is considered as a common occurrence in the design or evaluation of beams and slabs subjected to blast loading given the short duration of blast loading [1].

The peak response for such a structure responding in the impulsive dynamic range to blast loading, can be accomplished with a closed form equation derived using the conservation of energy method. Additionally, preload can be included by deducting the energy associated with the static preloads that remain constant through the dynamic motion of the structure. The following section shows the derivation for one of the closed form equations including preload.

Energy Method Equations

The strain energy at maximum structural response of the structural member was considered based on the ductility ratio concept. This method also incorporates the resistance and preload of the structural member. The structural resistance curve is idealized as shown in Figure 1 and Figure 2. In addition, equating strain energy with the kinetic energy resulting from an imparted blast load impulse, the peak response in terms of ductility can be determined. The derivation of the closed form energy method equations has been provided in [1] for predicting the effects of blast loading without preload. These equations have been used as the basis for the derived closed form energy method equations including preload.

Variable descriptions:

D = ductility ratio defined as:

$$D = \frac{y}{yu} \tag{1}$$

y = Displacement
yu = Displacement at elastic limit
yi = Displacement at initial state (preload)
R = Resistance
Ru = Resistance at elastic limit
Ri = Resistance at initial state (preload)
I = Impulse
Tn = Natural Time Period of equivalent SDOF system
R_{u_RS} = Remaining resistance defined as equation (4)

Without Preload:

Closed form equations to predict maximum response in terms of ductility without preload adopted from reference [1]:

$$D = \left(\left(\frac{2I\pi}{R_u}\right)^2 + 1\right)0.5 \quad \text{for } D > 1 \tag{2}$$

For D ≤ 1, R will correspond to the elastic response of the system:

$$D = \frac{I\,2\pi}{T_n Ru} \tag{3}$$

With Preload Included:

Based on the previous equations, the new equation including preload is derived for the case when the ductility ratio less is than 1 (elastic range), as presented in the Figure 1 and the following equations.

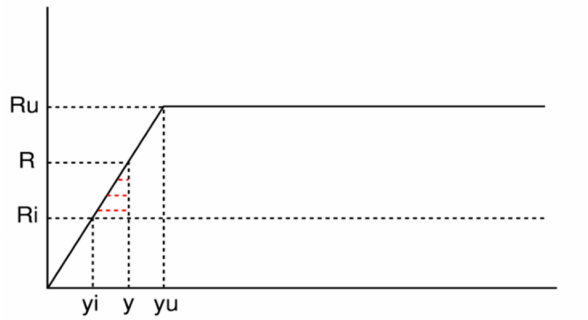

Figure 1. Resistance Curve - Elastic Response

The derivation of the mentioned closed form energy equation is as follows:

Using the 'remaining strength' method, for ductility ratio less than 1, the remaining resistance becomes:

$$R_{u\_RS} = R - R_i \tag{4}$$

Solving for maximum resistance :

$$R = R_{u\_RS} + R_i \tag{5}$$

Letting R_{u_RS} equal the elastic resistance per equation (3) and using the ductility at the elastic response (7):

$$R = \frac{I*2*\pi}{T_n} + R_i \tag{6}$$

Ductility factor at elastic response:

$$D = \frac{R}{R_u} \tag{7}$$

Substituting equation (6) into (7), we obtain the ductility equation for elastic response:

$$D = \left(\frac{I*2*\pi}{T_n*R_u}\right) + \left(\frac{R_i}{R_u}\right) \tag{8}$$

In addition, for ductility ratio above 1 at the elastic-plastic range is also presented in equation (9):

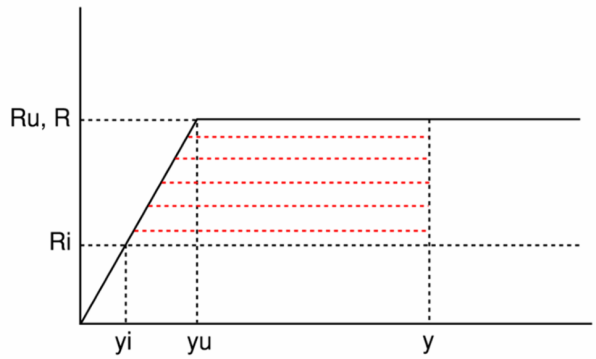

Figure 2. Resistance Curve - Elastic-Plastic Response

$$D = 0.5 * \left(\left(\frac{I*2*\pi}{T_n*(R_u - R_i)}\right)^2 + 1\right) * \left(\frac{R_u - R_i}{R_u}\right) + \left(\frac{R_i}{R_u}\right) \tag{9}$$

SDOF Model

An equivalent Single of Degree of Freedom analysis model is used to predict the peak response in terms of displacement of the actual beam structure. The real distributed mass and stiffness of the beam in the SDOF system is simplified as a lumped mass and spring using transformation factors that account for the support condition, loading and mass distribution of the real structural system. This method is appropriate for many structures where the response is primarily controlled by a single mode of vibration [4].

Furthermore, the structural response is modeled based on an elastic – plastic resistance curve shown in Figure 5 necessitating a non-linear time history analysis to predict the peak response of the equivalent SDOF system. The blast loading is idealized as a triangular pressure – time history curve as shown in Figure 6.

The real system is designed or investigated as shown in Figure 3 and Figure 4 shows the transformed equivalent SDOF model.

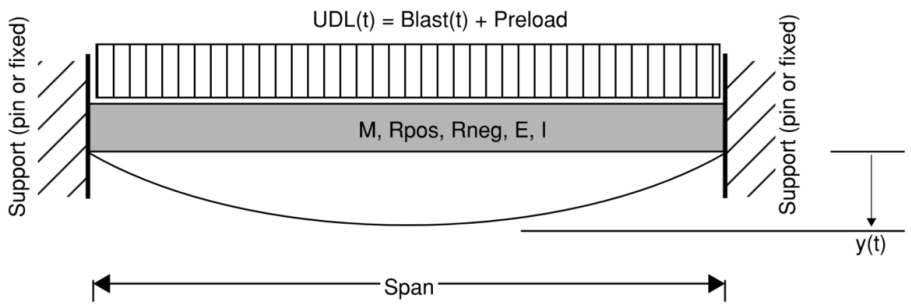

Figure 3. Structural System Subjected to Blast and Static Preloads

UDL =Uniformly Distributed Load including both transient blast loading and static preloading.

Blast(t) = Transient blast load applied in the direction of gravity loads (preload)

Preload = Static loads according to design standard load combinations (self-weight, superimposed dead, live load, snow)

M = Ultimate bending capacity of beam

R_{pos} = Positive resistance of beam for displacement in positive y direction

R_{neg} = Negative resistance of beam for displacement in negative y direction (rebound)

Y(t) =Maximum deflection of the beam at the corresponding location along the length of the beam

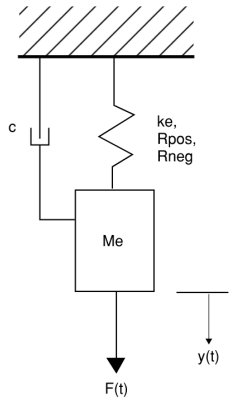

Figure 4. Equivalent SDOF Model

c = damping
k_e = effective stiffness taken into consideration the real beam support conditions, E and I.
M_e = effective mass taken into consideration the distributed mass of the real system
F(t) = Time history force applied to lump mass SDOF (Blast plus static Preload)

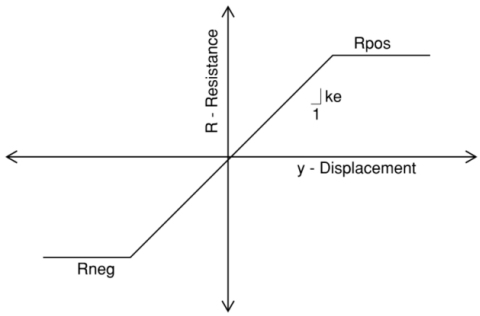

Figure 5. Idealized Elastic - Plastic Resistance Curve

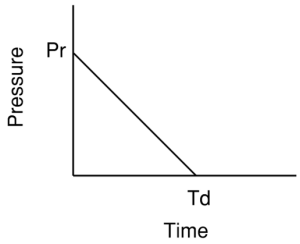

Figure 6. Idealized Blast Loading Time History

P_r – Peak pressure

T_d – Duration of the positive phase of blast loading

COMPARISON BETWEEN PREDICTIVE METHODS

The following sections compare the prediction of blast response of structures using the new derived closed form equations and rigorous SDOF analysis using an initial state of displacement and stress corresponding to the static preloads [5].

Comparing Energy Method to SDOF

The energy method equations have been derived based on the imparted impulse to the structure. For cases where the natural period of vibration is at least 10 times greater than the duration of blast loading, the peak response is determined based on the imparted blast load impulse alone. The following two scenarios have been investigated to compare the prediction of peak response between the new energy equations and rigorous SDOF analysis. A blast load duration to natural period ratio, Td/Tn, from 0.01 to 0.1 was used during the analysis.

1. Preload to Resistance ratio of 0.3, and a Resistance to Peak force ratio of 0.6. (Figure 7 and Table 1)
2. Preload to Resistance ratio of 0.3, and a resistance to Peak force ratio of 0.1. (Figure 8 and Table 2)

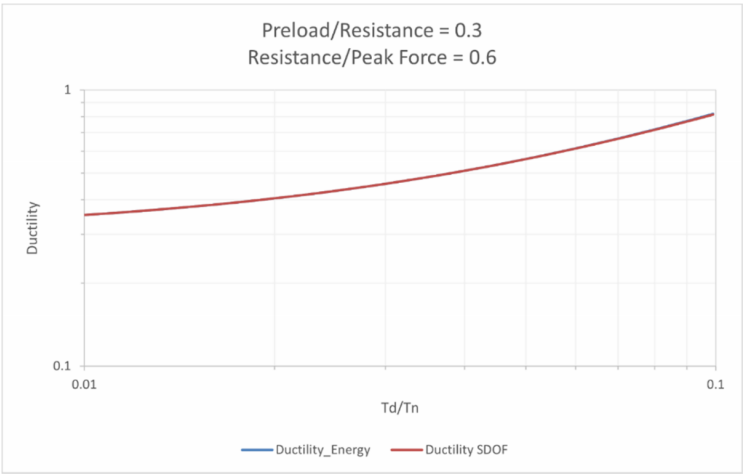

Figure 7. Energy Method to SDOF Comparison with Preload Ratio 0.3 and Resistance Ratio 0.6, Impulsive Range

Table 1. Energy Method to SDOF Comparison with Preload Ratio 0.3 and Resistance Ratio 0.6, Impulsive Range

Td/Tn	Ductility (Energy Equations)	Ductility (SDOF)	% Difference
0.01	0.352	0.352	0.02%
0.02	0.404	0.404	0.04%
0.04	0.508	0.508	0.01%
0.06	0.616	0.615	0.11%
0.10	0.818	0.813	0.57%

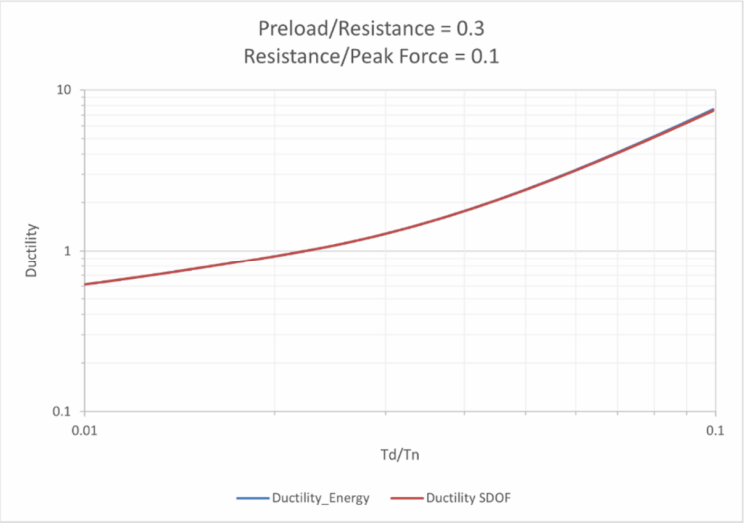

Figure 8. Energy Method to SDOF Comparison with Preload Ratio 0.3 and Resistance Ratio 0.1, Impulsive Range

Table 2. Energy Method to SDOF Comparison with Preload Ratio 0.3 and Resistance Ratio 0.1, Impulsive Range.

Td/Tn	Ductility (Energy Equations)	Ductility (SDOF)	% Difference
0.01	0.614	0.614	0.00%
0.02	0.924	0.924	0.01%
0.04	1.760	1.756	0.19%
0.06	3.219	3.200	0.60%
0.10	7.566	7.426	1.87%

It can be seen in the figures and tables that the new energy equations show perfect agreement with rigorous SDOF analysis over the provided range of load duration to natural period of vibrations. The results are within 2% difference.

The following figures and tables (Figure 9 and Figure 10, Table 3 and Table 4) compare the energy method equations to SDOF analysis over a wider range of load duration to natural period of vibration ratios, Td/Tn from 0.01 to 10.

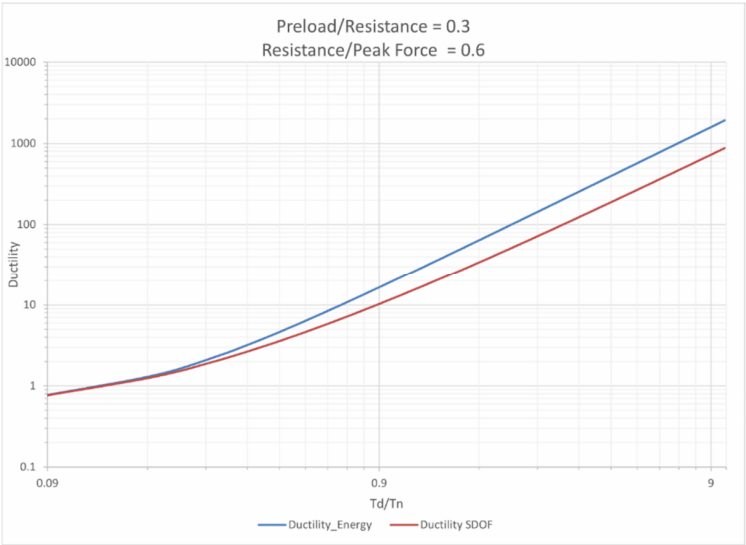

Figure 9. Energy Method to SDOF Comparison with Preload Ratio 0.3 and Resistance Ratio 0.6, Dynamic Range

Table 3. Energy Method to SDOF Comparison with Preload Ratio 0.3 and Resistance Ratio 0.6, Dynamic Range

Td/Tn	Ductility (Energy Equations)	Ductility (SDOF)	% Difference
0.1	0.771	0.767	0.43%
0.5	5.27	3.99	27.7%
1.0	23.5	14.0	50.8%
2.0	84.7	44.2	62.8%
10.0	1918	876	74.5%

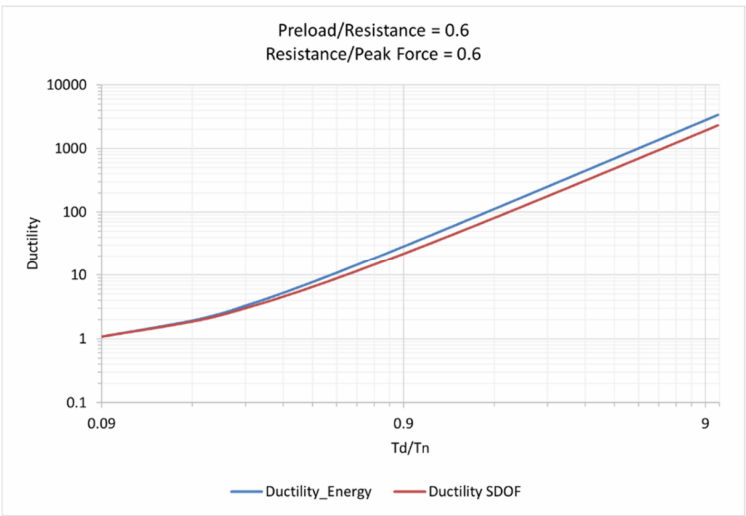

Figure 10. Energy Method to SDOF Comparison with Preload Ratio 0.6 and Resistance Ratio 0.6, Dynamic Range

Table 4. Energy Method to SDOF Comparison with Preload Ratio 0.6 and Resistance Ratio 0.6, Dynamic Range

Td/Tn	Ductility (Energy Equations)	Ductility (SDOF)	% Difference
0.1	1.08	1.07	0.28%
0.5	8.89	7.38	18.7%
1.0	40.8	30.7	28.3%
2.0	147	106	32.9%
10.0	3357	2308	37.0%

During a wider dynamic range of Td/Tn ratios, the energy method diverges from the SDOF method and the percentage of difference is increased up to 75%. The energy method equations are therefore not accurate when applied outside the impulsive response range of the structure, when the Td/Tn ratio exceeds 0.1.

Comparing Preload and Non-Preload Structures

The effect of preload is compared to non-preloaded structures in the following **Figure *11*** and

Table 5. For this comparison, the preload to resistance ratio was taken as 0.3 and the resistance to peak blast force ratio was 0.1. A preload ratio of 0.3 represents a typical beam designed for factored gravity loads. Only the impulsive response range of Td/Tn ratio from 0.01 to 0.1 is considered.

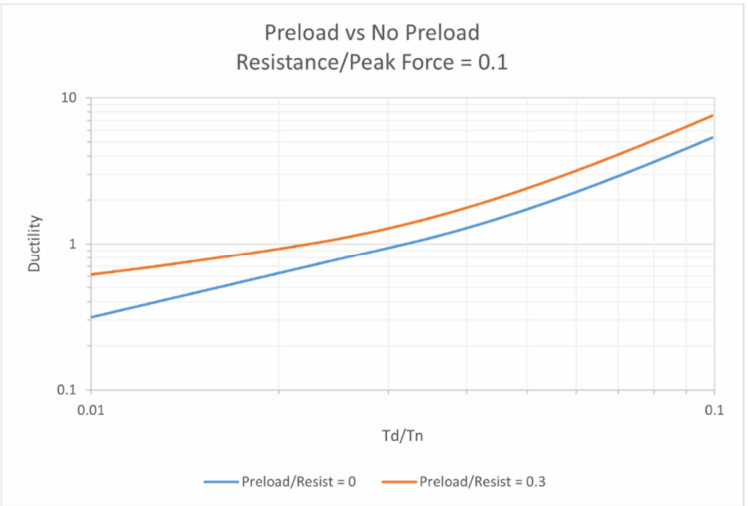

Figure 11. Preload versus No Preload

Table 5. Preload versus No Preload

Td/Tn	Ductility (Preload/Resistance = 0.0)	Ductility (Preload/Resistance = 0.3)	% Difference
0.01	0.314	0.614	64.7%
0.02	0.625	0.924	38.7%
0.04	1.277	1.756	31.8%
0.06	2.245	3.143	33.3%
0.10	5.34	7.566	34.5%

The results show that the effect of preload increases the structural response between 32% to 65% within the impulsive response range, for this given preload and resistance to force ratio.

WORKED EXAMPLES

The application of the closed formed energy method equations for concrete beam design will be presented in the following examples. Additionally, the results will be compared with the software program WSP-BLAST-BM that utilizes the non-linear time history SDOF method to predict response of reinforced concrete beams in accordance with the Canadian CSA S850-23 design standard [6].

Reinforced Concrete Beam with Low Level of Protection (plastic response D>1)

Predict the peak response in terms of ductility for a reinforced concrete beam with cross section of 3000 mm x 1200 mm and length of 10 m subjected to a blast load that was generated by a spherical burst resulting from the detonation of 50 kg (TNT) at a stand-off distance of 5 m. In addition, the effect of gravity loads (SDL, LL and self-weight) is to be considered. The beam is reinforced with top steel of (9800 mm^2) and bottom steel of (14000 mm^2). Calculate the ductility ratio of this beam.

First, Closed form equation using energy method:

From blast software: Impulse = 1394 kPa.msec, Equivalent duration (td) = 1.39 msec

Effective moment of inertia = 0.253 m^4, E_c = 30234.52 MPa,

$k_e = \frac{160\ EI_e}{L^3}$ = 1.23 x 10^9 N/m, m = 372867.9 kg, K_{LM} = 0.78

$T_n = 2*\pi*\sqrt{\frac{m*K_{LM}}{k}}$ = 96.67 msec

IMP = Impulse*trib area = 111520 N.sec

Preload (R_i) = 4777.834 kN, R_u = 8112.251 kN

$$D = 0.5 * \left(\left(\frac{IMP * 2 * \pi}{T_n * (R_u - R_i)} \right)^2 + 1 \right) * \left(\frac{R_u - R_i}{R_u} \right) + \left(\frac{R_i}{R_u} \right) = 1.76$$

Secondly as shown in Figure 12, Blast loading software (WSP-BLAST-BM):

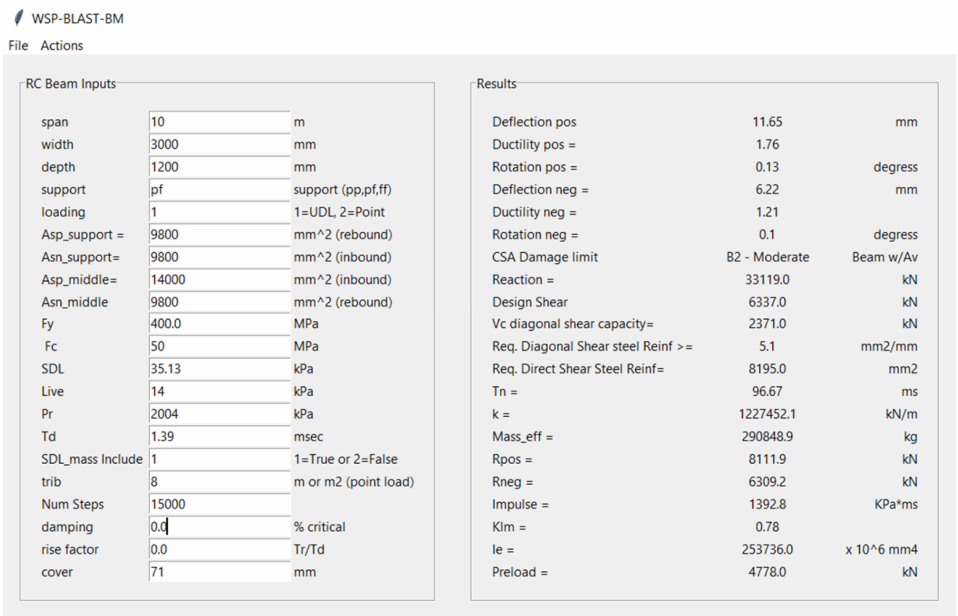

Figure 12. WSP-BLAST-BM example 1

Reinforced Concrete Beam with High Level of Protection (elastic response D<1)

Reinforced concrete beam with cross section of 3000 x 1200 mm and length of 10 m was subjected to blast loads that was generated by a charge weight of 50 kg (TNT) at a stand-off distance of 20 m. In addition, the effect of gravity loads (SDL, LL and self-weight) was considered in this example. This beam was reinforced with top steel of (9800 mm^2) and bottom steel of (14000 mm^2). Calculate the ductility ratio of this beam.

First, Closed form equation using energy method:

From blast software: Impulse = 281 kPa.msec, Equivalent duration (td) = 9 msec

Effective moment of inertia = 0.253 m^4, E_c = 30234.52 MPa,

$k_e = \frac{160\ EI_e}{L^3}$ = 1.23 x 10^9 N/m, m = 372867.9 kg, K_{LM} = 0.78

$T_n = 2*\pi*\sqrt{\frac{m*K_{LM}}{k}}$ = 96.67 msec

IMP = Impulse*trib area = 22480 N.sec

Preload (R_i) = 4777.834 kN, R_u = 8112.251 kN

$$D = \left(\frac{IMP*2*\pi}{T_n*R_u}\right) + \left(\frac{R_i}{R_u}\right) = 0.76$$

Secondly as shown in Figure 13, Blast loading software (WSP-BLAST-BM):

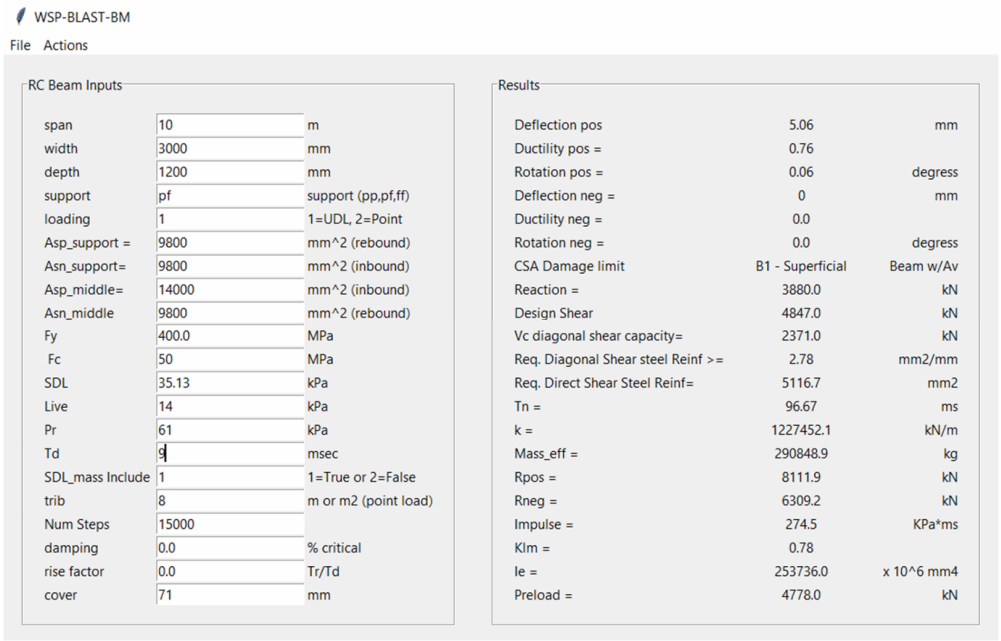

Figure 13. WSP-BLAST-BM example 2

CONCLUSION

The results of new energy equations that include the preload had perfect agreement with the results that obtained from the SDOF analysis at the short range from 0.01 to 0.1 of Td/Tn. However, at the larger range of Td/Tn ratio between 0.01 and 10, the results of energy method diverged up to 75% from the SDOF method results when Td/Tn ratio exceeds the impulsive range of 0.1, which is expected. In addition, it was clear that the effect of preload on the structures increases the structure response at the impulsive range up 65% when compared to un-preloaded structures. Finally, the results of two examples showed that the new energy equations (closed form equations) had good or perfect agreement with the WSP-BLAST-BM software means that these equations are reliable in the design stage.

REFERENCES

[1] Malhotra, A., Carson, D., and Stevens, T., (2007). Demystifying Blast Effects on Buildings. Journal of Structures, 36(2), 115-127.

[2] CSA Group (2023), CSA S850-23 Design and Assessment of Buildings Subjected to Blast Loads. CSA National Standard of Canada

[3] ASCE Petrochemical Energy Committee, (1997). Design of Blast Resistant Buildings in Petrochemical Facilities. ASCE.

[4] Biggs, J., (1964) Introduction to Structural Dynamics. McGraw-Hill, Inc.

[5] WSP Canada (2024).WSP-BLAST-SDOF. Batch processing of SDOF with Preloading. Ottawa, ON, Canada.

[6] WSP Canada (2024).WSP-BLAST-BM Reinforced concrete beam blast design program. Ottawa, ON, Canada.

[7] U.S. Army Corps of Engineers; PDC TR-06-02 Rev1; September 2008; Single-Degree-of-Freedom Blast Effects Design Spreadsheet (SBEDS); Department of Defense, Washington, DC.

PROTECT2024